UNIVERSITÀ DEGLI STUDI DI GENOVA

School of Mathematical, Physical and Natural Sciences

Doctorate in Science and Technologies of Chemistry and Materials

Curriculum: Chemical Sciences and Technologies

Doctor of Philosophy Thesis

XXXVIII Cycle

Assessment of the Repurposing Potential of Natural Gas API 5L X52 Steel Pipelines for Hydrogen Transport

Supervisors

Prof. Roberto Spotorno

Dr. Michelangelo Mortello

Technical Supervisors

Dr. Marco Palombo

Marco De Marco

PhD Candidate

Flavio Catalano

Academic Year 2024-2025

Table of Contents

Table of abbreviations

The present manuscript includes several abbreviations and acronyms, each of which is defined at its first occurrence in the text. For the reader's convenience, a comprehensive table listing all abbreviations and acronyms in alphabetical order is provided below.

Abbreviation	Definition	Unit of measurement
AIDE	Adsorption-Induced Dislocation Emission	
API	American Petroleum Institute	
A_{pl}	Area under the load–displacement curve	
B	Thickness	mm
BCC	Body-centered cubic	
BM	Base material	
C_0	Hydrogen subsuperficial concentration	ppm
CE	Carbon equivalent	
CMOD	Crack mouth opening displacement	mm
CT	Compact tension specimen	
D_{eff}	Effective diffusion coefficient	$m^2 \cdot s^{-1}$
DS	Devanathan-Stachursky	
EBSD	Electron backscattered diffraction specimen	
EI	Embrittlement index	
F	Faraday constant	96500 C
FCC	Face-centered cubic	
FCGR	Fatigue crack growth testing	
FZ	Fusion zone	
H	Hydrogen	
H	Lenght	mm
HAZ	Heat affected zone	
HE	Hydrogen embrittlement	
HEDE	Hydrogen Enhanced Decohesion	
HELP	Hydrogen Enhanced Local Plasticity	
HER	Hydrogen evolution reaction	
HESIV	Hydrogen-Enhanced Strain-Induced Vacancies	
I	Current	mA
J	Current density	mA/cm^2
J(t)	Flow	$mol \cdot m^2 \cdot s^{-1}$
J	J-Integral	kJ/m^2
J_{IC}	J-Integral critical value	kJ/m^2
J_{IH}	J-Integral critical value in H	kJ/m^2
K	Stress intensity factor	MPa√m
K_{IC}	K critical value	MPa√m

K_{IH}	K critical valure in H	MPa√m
LOM	Light optical microscopy	
NG	Natural gas	
N_T	Hydrogen traps concentration	$N° \cdot cm^{-3}$
SAW	Submerged arc welding	
SEM	Scanning electron microscopy	
SENB	Single edge notch bend specimen	
SENT	Single edge notch tension specimen	
σ	Stress	MPa
SMAW	Shielded metal arc welding	
SSRT	Slow strain rate test	
t	Time	s
T	Temperature	°C
TDA	Thermal desorption analyzer	
TEM	Trasmission electron microscopy	
TMCP	Thermo mechanically controlled process	
TU	Thiourea	
W	Widht	mm
WM	Weld metal	
YS	Yield Strenght	MPa
Z	Reduction Area	

Acknowledgments

I would like to thank everyone who made this doctoral research project possible. In particular:

- Università di Genova: Roberto Spotorno, Paolo Piccardo, Ivan Milano and all the members of the inorganic chemistry and metallurgy group, specially all the PhD and master students.
- Istituto Italiano della Saldatura-Ente Morale: Michelangelo Mortello, Marco Palombo, Marco De Marco, Michele Lanza, Filippo Alberto Recanzone, Lorenzo Carrattieri, Arash Kosari and all laboratory staff.
- Cranfield University: Francesco Fanicchia, Vikesh Kumar, Sravan Kumar Sambaraj, Husban Naiyer, Abdurrahmaan Akhtar, Tim Pryor and all Centre for Materials staff.

Finally, I thank my family without whom I would have never had this opportunity.

ABSTRACT

The energy transition aimed at achieving net-zero carbon emissions requires the integration of hydrogen into the global energy mix as a vector for the storage and transport of renewable energy. In this context, the repurposing of existing natural gas transportation infrastructure represents a strategic solution to accelerate its large-scale implementation. However, the phenomenon of hydrogen embrittlement poses critical issues that may compromise the structural integrity of pipelines.

This doctoral research project aims to investigate the effects of cathodic hydrogen on an API 5L X52 steel extracted from an Italian pipeline that has been in service since the 1970s with a view to assessing its suitability for future use in hydrogen applications. The experimental activity involved the base material and the girth weld in order to analyze the effect of microstructure on susceptibility to embrittlement. Hydrogen was introduced by electrochemical charging by optimizing parameters such as current density (J = -10 mA/cm^2) and electrolyte composition (0.01 mol/L H_2SO_4 and 2.00 g/L CH_4N_2S) at the laboratories of the Istituto Italiano della Saldatura-Ente Morale. The fusion zone accumulated a greater amount of hydrogen compared to both the base material and the heat affected zone. Despite the base material exhibiting larger grains than the heat affected zone, it absorbed a greater quantity of hydrogen due to its peculiar microstructure, characterized by alternating ferrite and pearlite bands and by the widespread presence of elongated manganese sulfides, which acted as trapping sites. The effect of hydrogen on mechanical properties was evaluated with fracture mechanics tests using notched tensile and bending specimens (SENT and SENB). The base material showed the greatest reduction in fracture toughness; however, the three materials exhibited similar behavior in hydrogen environment. Fractographic analysis performed by electron backscattered diffraction provided further insight into the embrittlement mechanisms. At Cranfield University, hydrogen permeation was investigated on base material, weld metal, and stressed base material specimens using a Devanathan–Stachurski cell. The base material exhibited the highest hydrogen diffusion coefficient but also promoted local hydrogen accumulation phenomena leading to surface blistering. In contrast, the weld metal was able to trap more hydrogen, showing slower diffusion and the absence of blistering. In the stressed metal, it was observed that the amount of absorbable hydrogen increased as strain intensity increased. Finally, an innovative experimental setup for the direct measurement of hydrogen permeation was designed and developed, based on the use of a mass spectrometer as a detector for hydrogen flow.

ABSTRACT (italian version)

La transizione energetica finalizzata all'azzeramento delle emissioni di carbonio richiede l'integrazione dell'idrogeno nel mix energetico globale quale vettore per l'accumulo e il trasporto di energia rinnovabile. In questo contesto, il riutilizzo delle infrastrutture esistenti per il trasporto di gas naturale rappresenta una soluzione strategica per accelerarne l'implementazione su larga scala. Tuttavia, il fenomeno dell'infragilimento da idrogeno pone delle criticità che possono compromettere l'integrità strutturale delle condotte.

Questo progetto di ricerca di dottorato mira a investigare gli effetti dell'idrogeno catodico su un acciaio API 5L X52 prelevato da un gasdotto italiano in servizio dagli anni '70, con l'obiettivo di valutarne l'idoneità per un futuro utilizzo in applicazioni legate all'idrogeno. L'attività sperimentale ha riguardato sia il materiale base che la saldatura circonferenziale al fine di analizzare l'effetto della microstruttura sulla suscettibilità all'infragilimento. L'idrogeno è stato introdotto mediante carica elettrochimica ottimizzando parametri quali densità di corrente (J = -10 mA/cm^2) e composizione dell'elettrolita (H_2SO_4 0,01 mol/L e CH_4N_2S 2,00 g/L) presso i laboratori dell'Istituto Italiano della Saldatura-Ente Morale. La zona fusa accumula una quantità di idrogeno superiore rispetto al materiale base e alla zona termicamente alterata. Nonostante il materiale base presenti grani più grandi rispetto alla zona termicamente alterata, assorbe una quantità superiore di idrogeno grazie alla peculiare microstruttura costituita da bande alternate di ferrite e perlite e alla presenza diffusa di solfuri di manganese allungati, che agiscono come siti di intrappolamento. L'effetto dell'idrogeno sulle proprietà meccaniche è stato valutato tramite prove di meccanica della frattura con provini intagliati di trazione e piega (SENT e SENB). Il materiale base evidenzia la maggiore riduzione di tenacità a frattura; tuttavia, in ambiente idrogenato i tre materiali mostrano un comportamento simile. L'analisi frattografica tramite diffrazione da elettroni retrodiffusi ha permesso di comprendere meglio i meccanismi di infragilimento. Presso la Cranfield University (UK) è stata studiata la permeazione di idrogeno in provini di materiale base, saldatura e materiale base deformato mediante cella di Devanathan–Stachurski. Il materiale base presenta il più alto coefficiente di diffusione dell'idrogeno ma favorisce fenomeni di accumulo locale che provocano blistering superficiale. La saldatura, invece, può intrappolare più idrogeno mostrando una diffusione più lenta e assenza di blistering. Nel metallo deformato è stato osservato che all'aumentare dell'intensità della deformazione, aumenta la quantità di idrogeno assorbibile. Infine, è stato progettato e realizzato un apparato sperimentale innovativo per la misura diretta della permeazione basato sull'impiego di uno spettrometro di massa come rivelatore del flusso di idrogeno.

INTRODUCTION, AIM AND STRUCTURE OF THE THESIS

Over the last century, the world's population and demand for energy have grown at a rate unprecedented in human history. This rapid development has had significant side effects, in particular an increase in the concentration of greenhouse gases in the atmosphere due to human activities, with harmful consequences for life on Earth. Climate change is now one of the greatest global challenges [1]. Global warming is having increasingly visible and dramatic impacts: desertification, rising sea levels, melting glaciers and frequent extreme heat waves [2]. These phenomena threaten not only biodiversity, but also the economic and social stability of the most vulnerable populations. The greenhouse effect is a natural mechanism that has been known to the scientific community since 1896, when Swedish scientist Svante Arrhenius first hypothesised that the increase in CO_2 due to growing industrialisation could modify the planet's thermal balance [3]. Since then, numerous studies have confirmed and expanded on this theory [4] [5] [6]. However, it was not until 1979, with the First World Climate Conference held in Geneva, that the international community began to seriously consider the need to curb emissions [7]. A concrete step forward came in 1997 with the Kyoto Protocol, which set a target of reducing greenhouse gas emissions by at least 8.65% compared to 1990 levels [8]. However, the most ambitious agreement is the Paris Agreement, signed in 2015 during COP21 [9]. It establishes a commitment to keep the global average temperature rise well below 2 °C, with the aim of limiting it to 1.5 °C. It also provides for a 55% reduction in emissions by 2030 and the goal of climate neutrality (net zero emissions) by 2050. To achieve these goals in the context of ecological transition, it is essential to gradually abandon fossil fuels as the primary source of energy [10]. International agreements are pushing for the electrification of the most energy-intensive sectors, such as heavy industry, transport and domestic heating, with the exclusive use of renewable sources: solar, wind, geothermal and hydroelectric. However, although these sources are clean and unlimited, they are intermittent: the sun doesn’t always shine, the wind doesn’t always blow, and rivers don’t always flow at a constant rate [11]. To manage this discontinuity, storage systems such as batteries are used to store electrical energy for use when needed. However, batteries still have significant limitations: the use of rare and expensive metals such as lithium and cobalt, polluting production and disposal processes, heavy weight that limits their use in mobility, still reduced autonomy and long recharging times [12] [13]. In this context, hydrogen (H) is playing an increasingly important role as a flexible, low-emission energy carrier [14]. Green H, produced by electrolysis powered by renewable sources, allows surplus energy to be converted into a fuel that can be used as needed according to the Power-to-Gas (P2G [15]) principle. It can thus be transported and used to power industrial sectors that are difficult to electrify, contributing substantially to decarbonisation. For distances greater than 500 km, the most efficient and environmentally friendly solution is gas pipelines [16]. Europe already

has a network of approximately 200,000 km of gas pipelines for transport, in addition to 2 million km for local distribution and over 20,000 natural gas regulation stations [17]. Repurposing this infrastructure for H transport is the fastest and most cost-effective way to accelerate its large-scale adoption [18]. The potential path of H, from production to end use, is shown in Figure 1.

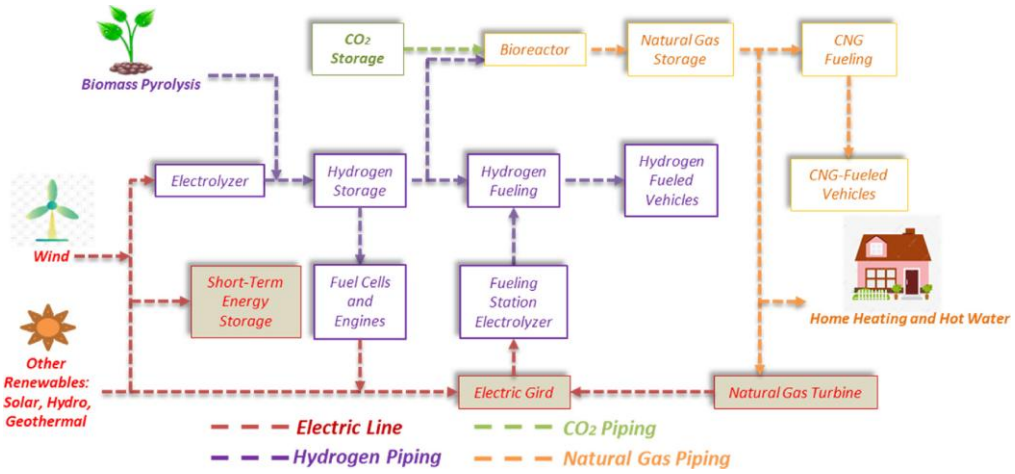

Figure 1-*Possible H pathways [19].*

Many global projects are currently underway to implement H in the energy mix. The main ones are summarised in Table 1 [20]. However, there are challenges: for the same amount of energy released, H requires higher pressure than natural gas due to its lower atomic weight, and its wider flammability limits make it dangerous in the event of leaks [21]. The production of green H is currently very expensive (6 to 16 times more than that from hydrocarbons, grey H [22]). Finally, as it is the element with the smallest atomic radius (0.53 Å), it can penetrate and dissolve into the matrix of many metals. This process progressively degrades the mechanical properties of the material, increasing the risk of structural failure. Already in the last decades of the 19th century, several unexpected structural failures of metal structures were linked to the presence of H in the material [23]. In 1875, Johnson published the first scientific article observing the decrease in the mechanical properties of steels in hydrogenated environment [24]. Since then, countless studies have been conducted on the subject, from the characteristics [25] and modelling of the mechanism [26] [27] to the effect on various commercial alloys [28] [29].

Table 1-*Most important H implementation projects around the world.*

Project	Nation	Aims
HyDeploy	UK	20% H in natural gas
Hy4Heat	UK	100% H as fuel for residential and commercial buildings
HyP SA	Australia	5% green H in natural gas
Hyblend	USA	Technical assessment for adding H to natural gas
Snam	Italy	10% H in natural gas
GRHYD	France	20% H in natural gas
EN-H_2	Portugal	Achieving Net Zero by implementing H in the energy mix

H damage comes in various types and forms:

- Blistering
- Hydrides formation
- Hydrogen attack
- Hydrogen embrittlement (HE)

Blistering occurs when H atoms accumulated in microstructural defects in the matrix recombine to form molecular H. At the matrix/inclusion interface, the pressure can be so high that it plastically deforms the material, forming blisters that can be preferential initiation sites for microcracks. Under high temperature and high pressure conditions, H attack can occur. In low-alloy steels, H can react with carbon to form hydrocarbons. This not only decarburises the material but also leads to the formation of cracks. If alloys such as titanium, zirconium and tantalum are present in a steel, there is a possibility that they will be sequestered by H and precipitate as hydrides. This reaction lowers the strength of the material because hydrides are typically low in density and very brittle [30]. In all of the phenomena described above, the causes of mechanical failure are directly attributable to the action of H, which always undergoes a phase transformation. Furthermore, for these phenomena to occur, extreme temperature and pressure conditions are required, where a large amount of H is introduced into the material (Figure 2).

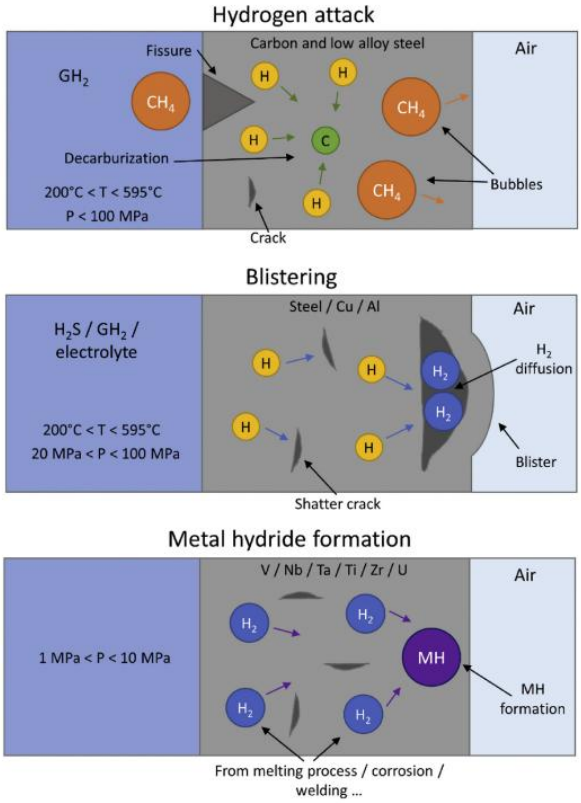

Figure 2-*Sketches of H attack, blistering and hydride formation [31].*

HE [32], on the other hand, is a more subtle effect, indirectly caused by H atoms diffused in the crystal lattice, which can occur at room temperature, even with low levels of hydrogenation in the presence of mechanical stress, whether static or cyclic, or even internal residual stress (Figure 3). The result is the formation of cracks with a brittle morphology, which propagate under the combined action of stress and the environment, and which can lead to the unexpected failure of the loaded component, due to stresses lower than the maximum strength of the metal in air. The propagation of cracks is usually perpendicular to the tensile stress, and it is not uncommon to observe crack branching. In particular, the mechanism occurs in two stages: crack initiation and propagation. Usually, the initiation phase is preceded by an incubation period, during which micrometric or even nanometric "crack embryos" form, i.e. very small defects or imperfections at emerging inclusions, grain boundaries and interfaces between different phases. The crack propagation phase can be stable or unstable. In the case of stable propagation, the crack advances due to the combined effect of the environment and the applied stress, stopping if one of the two factors is removed and resuming propagation if the conditions favourable to its advancement are restored. When the crack reaches a critical size, its growth becomes unstable, leading to material failure [33].

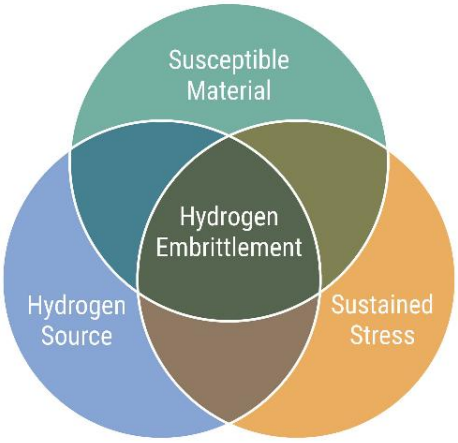

Figure 3-*Main factors contributing to HE [34]*

Current gas pipelines are made from steel produced over a very long period of time, from the 1960s to the present day. In addition, the pipes are joined by kilometres and kilometres of welds that present critical issues such as HAZs and residual stresses generated during the process. For this reason, it is essential to thoroughly understand the properties of these materials in H environment. Only then is it possible to accurately assess the suitability of existing pipes to operate safely with H. This thesis is part of a large-scale project, begun in 2022 at the Istituto italiano della Saldatura-Ente Morale in collaboration with Università degli Studi di Genova, to study the effect of H on the mechanical properties of vintage API 5L X52 steel extracted from an Italian gas pipeline. The activities began with the acquisition of materials and data obtained from previous work. In particular, various electrochemical parameters were tested to obtain the optimal charging conditions for introducing H into the steel. Subsequently, the BM and weld were tested using slow strain rate testing (SSRT) with in situ H charging. At this point, the electrochemical parameters were further refined and the effect of charging time on the base material (BM), heat affected zone (HAZ) and fusion zone (FZ) was studied. The effect of H was investigated using fracture mechanics tests on both tension and bending specimens. During the seven-month research period at Cranfield University (UK), the effect of microstructure and mechanical stress on H permeation was studied using the Devanathan-Stachursky cell. In addition, an innovative experimental apparatus was constructed to directly determine H permeation. This thesis has been divided into four chapters as follows:

- Chapter 1. The first chapter provides a comprehensive overview of the scientific and technological context relevant to this study. It opens with an introduction to the steels used in gas transport pipelines, with a particular focus on API grades and their microstructural characteristics. The phenomenon of HE is then discussed from multiple perspectives, including H diffusion mechanisms, trapping theory, and the main embrittlement models

proposed in the literature. The theoretical aspects of fracture mechanics are presented, followed by an overview of the current regulatory framework and mechanical testing in H environment. It concludes with a review of previous experimental activities conducted prior to the start of this doctoral research.

- Chapter 2. The second chapter describes the API 5L X52 vintage pipeline steel and its girth weld, including chemical composition and microstructural characterization. The experimental procedures adopted through the research are detailed, including applicable reference standards, specimen geometries (SENT and SENB), electrochemical H charging conditions, fracture mechanics testing protocols, EBSD analysis, and h permeation measurements using the Devanathan–Stachurski cell. The design and development of an innovative experimental apparatus for direct H permeation measurement based on a mass spectrometer are also presented.
- Chapter 3. The third chapter presents and critically discusses the experimental results. The H uptake capacity of the BM, HAZ, and FZ is analyzed in relation to their microstructural features and trapping characteristics. The influence of H on fracture toughness and crack propagation behavior is evaluated. Permeation results are interpreted in terms of diffusion coefficients, trapping effects, and blistering susceptibility. The role of plastic deformation on H absorption is also examined. The findings are discussed in light of existing theoretical models and literature data.
- Chapter 4. The final chapter summarizes the main outcomes of the research, highlighting the scientific contributions of the work to the understanding of H–steel interaction in pipelines. The implications for the safe repurposing of existing natural gas infrastructures for H transport are outlined. Finally, future research perspectives are proposed, including further experimental developments and the broader role of materials research within the ongoing energy transition.

1. Hydrogen interaction with steels

1.1 Pipeline steels

The materials that best meet the suitability criteria for gas pipelines are high-strength low-alloy (HSLA) steels. The American Petroleum Institute (API) regulates the technical specifications for these steels by the API 5L standard (European equivalent EN 10208), which are recognised and accepted worldwide [35]. They are currently produced according to two levels of specifications: PSL1 and PSL2 (in addition to mechanical properties, PSL2 has limitations on carbon equivalent and pipe end shape [36]). The main grades with their characteristic mechanical properties are summarised in Table 2 (in API nomenclature, the number after the X indicates the minimum yield strength in psi). The production of pipeline steels began in the mid-20th century to meet the growing demand for high-pressure oil and gas. The first grades, such as API X42, X46 and X52 introduced in the 1940s and 1950s, were characterised by moderate strength and limited toughness, but with the increase in energy demand and the need for larger pipes, grades such as X65, X70 and X80 were developed, leading to the current X100 and X120 [37]. Originally, after casting into ingots, the steel was heated and rolled to obtain the final products. The key to achieving an optimal microstructure was achieved with thermo mechanically controlled processing (TMCP [38]). This process involves a sequence of rolling operations performed at controlled temperatures to progressively reduce the size of the austenitic grains and induce the formation of fine ferritic grains during the cooling phase. In the most advanced grades, simple rolling control is combined with accelerated cooling, which allows transformation into acicular ferrite and bainite. The result is a material characterised by high strength, good toughness and superior weldability compared to traditional alloy steels [39]. The microstructure of API 5L steels can include different phases: various morphologies of ferrite (polygonal, quasi-polygonal, acicular), bainite, pearlite, non-metallic precipitates and islands of martensite/austenite. Optimisation of the rolling and cooling process allows the relative fractions of these phases to be adjusted and an optimal balance between strength and ductility to be achieved [40] [41].

Table 2-*Difference between PSL1 and PSL2 based on mechanical properties.*

Grade	Yield strength minimum [Mpa]	Yield strength maximum [MPa] for PSL2	Ultimate tensile strength minimum [MPa]	Ultimate tensile strength maximum [MPa] for PSL2
X42	290	496	414	758
X46	317	524	434	758
X52	359	531	455	758
X56	386	544	490	758
X60	414	565	517	758
X65	448	600	531	758
X70	483	621	565	758
X80	552	690	621	827
X90	625	775	695	915
X100	690	840	760	990
X120	830	1050	915	1145

Careful balancing of alloying elements allows HSLA to achieve superior mechanical properties compared to common carbon steels [42]. They generally contain carbon (C) up to 0.1 wt%, manganese (Mn) up to 2.0% and small amounts of other elements such as niobium (Nb), vanadium (V), titanium (Ti), molybdenum (Mo), chromium (Cr), boron (B) and silicon (Si). The effect of alloying elements is shown in Table 3. Furthermore, the tubes are joined by welding, and therefore particular attention must be paid to avoid process defects that could compromise the reliability of the component.

Carbon equivalent (CE) formulas are used to predict the susceptibility of carbon steels to HE based on their chemical composition. Although there are various expressions for CE, it is commonly calculated according to Eq. 1 (numbers are expressed as a percentage by weight):

$$CE = C + \frac{Mn}{6} + \frac{Cr+Mo+V}{5} + \frac{Ni+Cu}{15} \quad \text{Eq. 1}$$

In general, the higher the CE value, the greater the susceptibility of steel to HE. Composition limits to contain HE include S <0.01 wt%, P <0.015 wt% and CE < 0.35 [43]. The CE specification was designed to avoid the formation of untempered martensite, which is the microstructure most susceptible to HE during welding [44]. Over time, natural gas transport infrastructure has undergone numerous changes in chemical and engineering requirements, with the aim of ensuring ever-higher mechanical performance. For this reason, the pipeline network in operation today is composed of a wide variety of materials: over the years, different grades of steel have been introduced, developed through different production processes [45]. This has resulted in significant variations in chemical composition, microstructure and mechanical properties, not only between different grades, but also

within the same grade depending on the time of manufacture. This makes it difficult to compare the results of mechanical tests performed on samples of different steels, as a correct interpretation also requires consideration of microstructural and compositional peculiarities [36]. Consequently, it is particularly difficult to formulate a general and unambiguous assessment of the HE resistance of the current pipeline network.

Table 3-*Effect of alloying elements in pipeline steels [36].*

Element	Effect
C	Increases hardness and strength but reduces ductility and weldability
Mn	Strengthens the alloy in solution but can segregate, promoting HE
Nb	Refines grain and strengthens by precipitation
V	Strengthens ferrite grains
Ti	Refines grain
Mo	Strengthens ferrite and promotes bainite formation
Cr	Increases hardenability by delaying ferrite-pearlite transformation
B	Increases hardness
Si	Deoxidiser

1.2 H-Fe Interaction

H can come into contact with steel in two forms: electrolytic and gaseous. There are several circumstances in which this occurs: pickling, contact with liquids or gases containing H, electrodeposition, phosphating, welding and heat treatments. It is also possible for H to penetrate the metal during service conditions, for example in the presence of cathodic overprotection or in any form of corrosion involving the evolution of H as a cathodic process, such as galvanic corrosion or simple contact with high-pressure H [41]. Once absorbed by the steel, it diffuses into the crystal lattice in atomic form. Consequently, the induced effects are similar regardless of the entry mechanism [46] [47] [48] (Figure 4).

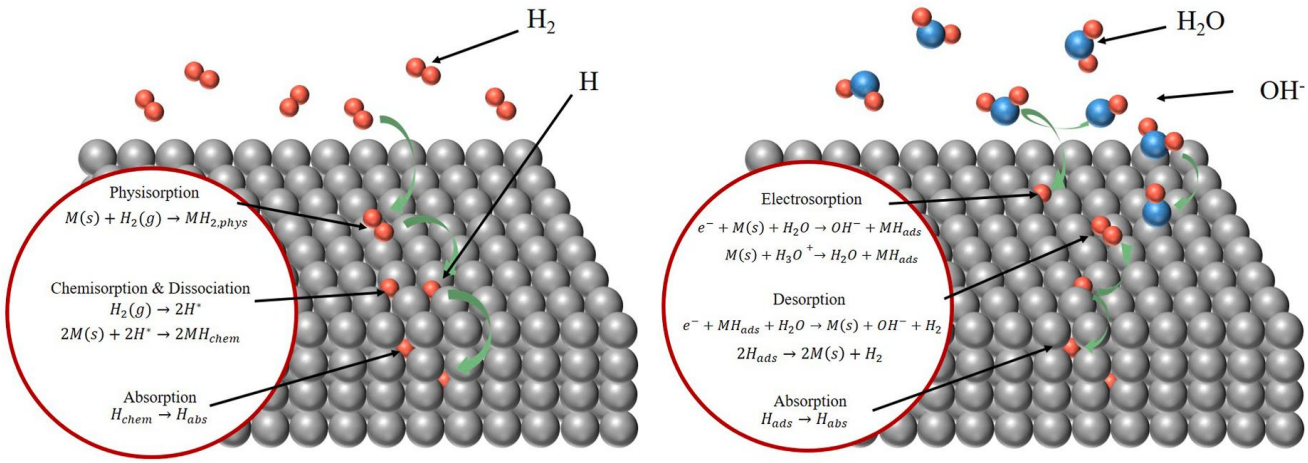

Figure 4-*Comparison between H gas and electrolyte permeation [49]***.**

1.2.1 Gaseous Interaction

The diatomic molecules of H gas cannot penetrate directly into the metal matrix. It is therefore necessary for these molecules to be dissociated into H atoms. The spontaneous dissociation of H_2, promoted solely by molecular collisions, is not thermodynamically sustainable under typical pipeline operating conditions. Instead, the energetically favoured mechanism is catalytic dissociation on the steel surface: H molecules interact with the surface sites of the metal, where they undergo H–H bond breaking and release atoms capable of diffusing. This process, known as dissociative adsorption, is gradually favoured by higher partial H pressure and temperature conditions, which lower its Gibbs free energy [50]. Initially, the molecules interact with the steel surface through physisorption, i.e. weak van der Waals interactions. This phenomenon is reversible and does not yet produce mobile atomic H. The adsorption capacity depends on the crystallographic structure of the surface: low crystal index planes, such as Fe (100) or Fe (110), offer more favourable sites, while defects such as grain boundaries, dislocations or inclusions act as additional sites that increase the amount of H adsorbed. This is followed by the chemisorption process, in which the molecules dissociate and the

atoms are strongly bound to the surface sites of the iron. It is at this stage that H becomes effectively available for subsequent permeation [51]. The physisorption process and the two phases of chemisorption are presented in Eqs. 2, 3 and 4 respectively (H^* is high-energy atomic H).

$$M(s) + H_2(g) \leftrightarrows MH_{2\,phys} \quad \text{Eq. 2}$$

$$H_2(g) \rightarrow 2H^* \quad \text{Eq. 3}$$

$$2M(s) + 2H^* \rightarrow 2MH_{chem} \quad \text{Eq. 4}$$

1.2.2 Electrolytic Interaction

In an aqueous environment, H can develop on the surface of a cathodically polarised metal. Since dissolved H is necessarily dissociated into a proton and a conduction electron, the cathodic charge becomes a direct transfer of protons, with the result that the proton (H^+) is transferred from the aqueous solution (H^+_{aq}) to the metal (H^+_M), adsorbed on the surface and then absorbed into the crystal lattice [51]. The hydrogen evolution reaction (HER) can occur in both acidic and basic environments [52]. In the former case, the overall reaction is described by equation 5.

$$2H^+_{aq} + 2e^- \leftrightarrows H_{2(g)} \quad \text{Eq. 5}$$

The mechanism first involves the electrochemical adsorption of H, the Volmer reaction (Eq. 6), followed by the electrochemical (Heyrovsky reaction, Eq. 7) and/or chemical (Tafel reaction, Eq. 8) desorption of H.

$$H^+ + M + e^- \leftrightarrows MH_{ads} \quad \text{Eq. 6}$$

$$MH + H^+ + e^- \leftrightarrows M + H_2 \quad \text{Eq. 7}$$

$$2MH \leftrightarrows 2M + H_2 \quad \text{Eq. 8}$$

The global HER in alkaline solution is described by equation 9.

$$2H_2O + 2e^- \leftrightarrows H_2 + 2OH^- \quad \text{Eq. 9}$$

The Volmer-Heyrovsky-Tafel mechanism in alkaline solution is given by equations 10, 11 and 12 respectively.

$$H_2O + M + e^- \leftrightarrows MH_{ads} + OH^- \quad \text{Eq. 10}$$

$$MH + H_2O + e^- \leftrightarrows M + OH^- + H_2 \quad \text{Eq. 11}$$

$$2MH \leftrightarrows 2M + H_2 \quad \text{Eq. 12}$$

In both cases, part of the adsorbed H on the metal surface diffuses through the lattice (Eq. 13):

$$H_{ads} \rightarrow H_{abs} \quad \text{Eq. 13}$$

1.3 Hydrogen diffusion theory

The diffusion of H in the steel lattice is a parameter of fundamental importance in studying the interaction between the microstructure of the material and the H atom, in evaluating trapping sites and in developing strategies to improve HE resistance. The main mechanisms of H diffusion in a metallic material are [53]:

- Interstitial diffusion: H migrates from one interstitial site to the adjacent one.
- Vacancy or substitution diffusion: H atoms move to occupy the positions left vacant by the matrix atoms. The speed of the process depends both on the difference in size between the H atoms and those of the matrix, and on the differences in binding energies.
- Transport via mobile dislocations: under conditions of local plastic deformation, for example at the tip of a crack, H can bind to a mobile dislocation and move with it. In BCC structures, this mechanism can generate transport speeds up to an order of magnitude higher than interstitial diffusion alone.
- Transport along grain boundaries: under certain conditions, grain boundaries can act not only as H traps but also as diffusion channels. In boundaries characterised by a high density of dislocations and vacancies, trapping phenomena prevail, while in high-angle boundaries, diffusion is favoured and accelerated [46].
- Quantum tunnelling: a mechanism that only becomes significant at low temperatures, when H can cross energy barriers due to the quantum effect [54].

The diffusion of a species is governed by Fick's two laws. Fick's first law (Eq. 14) states that the flow of a diffusive species, such as H, is related to the concentration of that species. Specifically, H flows from regions of higher concentration to regions of lower concentration, with an intensity directly proportional to the concentration gradient.

$$J = -D\frac{\partial C}{\partial x} \qquad \text{Eq. 14}$$

Where J [mol·m²·s⁻¹] is the flow of H atoms passing through a known surface area per unit time, D [m²·s⁻¹] is the diffusion coefficient, C [mol·m⁻³] is the concentration of the diffusing species, and x [m] is the distance travelled by the diffusing species. However, Eq. 14 is only applicable under steady-state conditions. Since it is not possible to determine steady-state conditions, it is necessary to use Fick's second law instead, according to the following equation (Eq. 15):

$$\frac{\partial C}{\partial t} = D\frac{\partial^2 c}{\partial^2 x} \qquad \text{Eq. 15}$$

Therefore, a transient diffusion mechanism involves a change in H concentration at any location, as a function of time and according to Fick's second law.

1.3.1 Diffusion into interstitial sites

Iron has three stable allotropic forms at different temperature ranges:

- α iron up to 912 °C
- γ iron between 912 °C and 1394 °C
- δ iron between 1394 °C and melting point at 1538 °C

Iron α and δ have a body-centred cubic (BCC) lattice, while γ has a face-centred cubic (FCC) lattice. The solid solution of carbon in iron is classified according to its allotropic form: δ ferrite for carbon in δ iron, austenite for carbon in γ iron and α ferrite for carbon in α iron [55]. Once absorbed, H atoms diffuse into the host lattice and arrange themselves in the interstitial sites of the metal and in trap sites (Figure 5).

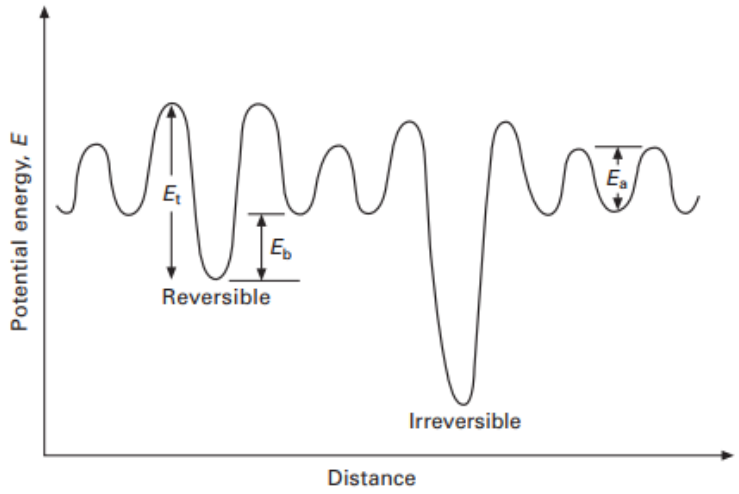

Figure 5-*Diagram of the potential energy associated with interstitial diffusion sites (with activation energy E_a) and trapping sites (characterised by binding energy E_b and activation energy E_t). The energy required to release H from trapping sites varies depending on the nature of the site itself [56].*

H in the interstices creates a local distortion that increases the total energy of the system through a contribution of elastic deformation. The size and geometry of the interstitial sites are therefore a fundamental parameter for determining how much H can actually be hosted within the metal matrix [57]. In cubic lattices, it is possible to distinguish between two types of interstitial sites, octahedral (O) and tetrahedral (T) (Figure 6). Calculations based on the ratio between the interstitial site radius and the atomic radius of the host lattice have shown that O sites are predominantly occupied in FCC lattice structures, while T sites are preferred in BCC lattices at room temperature [57]. At temperatures

above 100 °C, however, entropic factors cause an increase in the fraction of occupied O sites [57]. The sizes and numbers of interstitial sites are presented in Table 4.

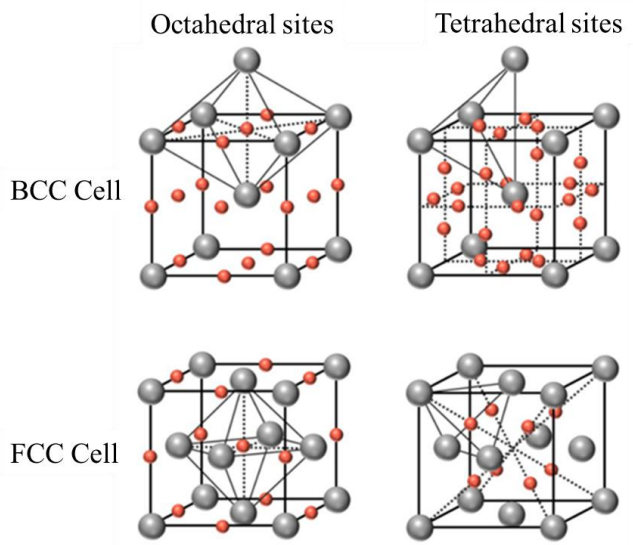

Figure 6-*Potential sites for H atom accommodation in bcc and fcc lattices (grey—Fe atoms, red—interstitial sites) [55].*

Table 4-*Quantity and size of interstitial sites in BCC and FCC lattices.*

Crystal lattice	**T site**		**O site**	
	N° per Fe atoms	Radius [Å]	N° per fe atoms	Radius [Å]
BCC	6	0,35	3	0,19 Å
FCC	1	0,28	2	0,52

Reticular diffusion through interstitial sites is the main mechanism of H transport in steel. H is more soluble in the FCC structure due to the larger size of the octahedral site compared to the tetrahedral site in BCC (Table 4). The two structures also have different atomic packing factors: 0.68 for BCC and 0.74 for FCC, which is therefore more compact. BCC, being less dense and characterised by a greater number of interstitial sites per unit cell, has a lower activation energy for H jumping between interstitial sites. This translates into a higher diffusion rate in the BCC lattice than in the FCC. Martensite, on the other hand, has a body-centred tetragonal (BCT) structure, but as the carbon content increases, the tendency to form compact hexagonal martensite (HCP) increases. These crystal configurations, which are more densely packed than BCC, reduce H mobility. Therefore, H diffusion in martensite is lower than in ferrite [58]. In the FCC lattice, diffusion does not occur via a direct jump from one octahedral site to another, but rather in two successive stages. In fact, to make a direct jump between two octahedral sites, H would have to overcome a high energy barrier (1.24 eV). The actual process, however, initially involves migration from an O site to a T site (0.73 eV), followed by the transition from the tetrahedral site to another octahedral site (0.21 eV). Therefore, in the FCC

lattice, diffusion follows an O-T-O path. The diffusion coefficient is determined by the slow stage, i.e. the migration from the O site to the T site (Figure 7a). In a perfect FCC lattice of Fe atoms, the following applies to H (Eq. 16):

$$D(T) = 3.22 \cdot 10^{-4} \cdot e^{-\frac{8425}{T}} \, [cm^2/s] \qquad \text{Eq. 16}$$

In the BCC cell, when a H atom occupies an O site, it spontaneously migrates to a T site, thus reaching the global minimum of total energy. In this crystal structure, H therefore diffuses along a purely T–T–T path. The diffusion barrier for a H atom to jump from one T site to the nearest T site is 0.096 eV, which explains the high mobility of H in BCC iron (Figure 7b). The diffusion coefficient of H in a perfect BCC iron lattice can be estimated using the following relationship (Eq. 17):

$$D(T) = 1.379 \cdot 10^{-4} \cdot e^{-\frac{1120}{T}} \, [cm^2/s] \qquad \text{Eq. 17}$$

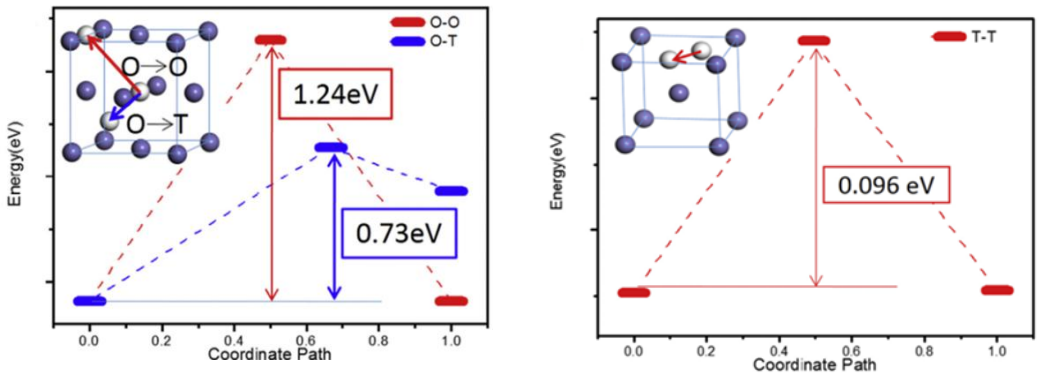

(a) (b)

Figure 7-*Energy barriers for H atom diffusion relative to* (a) *Fe-fcc,* (b) *Fe-bcc.*

Firstly, the concentration of H within steel (C_H) can be calculated using Sieverts' equation [59] (Eq. 18)

$$C_H = S \cdot \sqrt{f_H} \qquad \text{Eq. 18}$$

where S is the Sieverts constant, which depends on temperature and steel type, while f_H is the fugacity of H (pressure exerted by a gas with ideal behaviour). The fugacity value increases for pressures above 200 bar [60]. The concentrations calculated using Sievert's law are lower than those obtained experimentally because H atoms in the interstitial sites of the lattice are only a fraction of those present in the lattice at equilibrium. Microstructural defects constitute other H storage sites called trap sites. Furthermore, Sievert's law assumes that the metal surface is completely available to interact

with H. In real conditions, however, the presence of surface oxides or gaseous impurities can cause the results to diverge from ideal conditions [61].

1.3.2 Diffusion into trap sites

All metallic materials have inevitable imperfections in their crystal lattice, which can trap H atoms inside them [58]. The presence of traps, both inside the metal and on its surface, causes several effects [33]:

- increase in the overall solubility of H and its local concentration;
- reduction in the apparent diffusivity of H;
- influence of the path of H penetration into the material on the diffusion phenomenon, making it unpredictable based on Fick's equation alone.

If the available thermal energy is sufficient to allow the H atom to escape from a trap, the latter is defined as reversible. It is important to note that there is no clear boundary in terms of binding energy between reversible and irreversible traps: the probability that a H atom will escape from a trap gradually decreases as the binding energy increases, until it becomes negligible for the strongest bonds. As the temperature increases, this probability increases significantly, the residence time of H in the trap decreases, and consequently the effective diffusivity of H in the material increases [58]. Figure 8 shows typical H traps and the classification of reversible and irreversible traps based on binding energy, where E_R and E_{IR} are the reversible and irreversible binding energies of H, respectively, E_S is the energy barrier, and E_d is the desorption energy. In general, at ambient T, a trap with a binding energy greater than 50 kJ/mol can be considered irreversible [48]. Table 5 lists the most common H traps with their binding energies. Typical reversible traps are edge and screw dislocations, low-angle grain boundaries, cementite/ferrite boundaries, and austenite/ferrite interfaces. Irreversible H traps are mixed dislocations, non-metallic inclusions, secondary phases, precipitates, and vacancies. Wide-angle grain boundaries can be either reversible or irreversible traps [62].

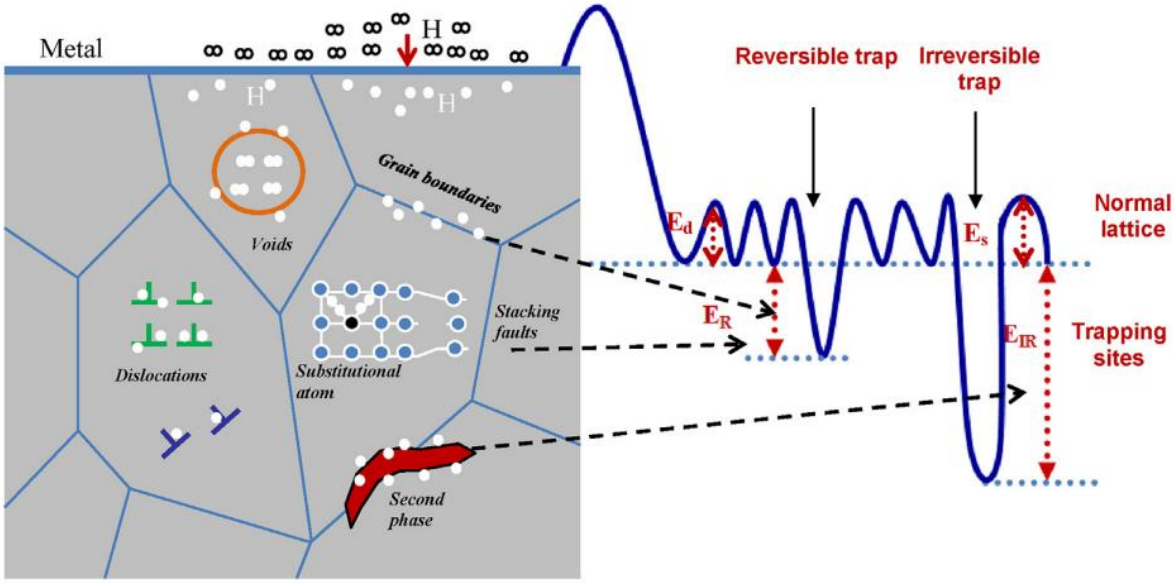

Figure 8-*Typical H traps and corresponding energy diagram [63].*

Since H atom finds a more energetically stable configuration within a trap than in an interstitial site of the lattice, the probability of it moving towards a trap is greater than that of jumping to an interstitial site. In the crystal lattice, there are two main reasons why the probability of H jumping can be modified [64]:

- Presence of a directional force. An attractive force of unknown origin directs the movement of H in a preferred direction. This behaviour can be explained by the nature of H as a shielded proton or, more simply, by its small atomic size and consequent high mobility. In this condition, the physical space of the lattice is not altered, but it is more likely that H will jump in the direction of the applied force, being attracted towards its origin.
- Distortion of the lattice. Distortion modifies the average height of the H atom jump. This effect makes the process of release from the trap more complex.

Table 5-*Typical H traps and their binding energy in Fe BCC [46].*

Trap	**Binding Energy [kJ/mol]**
Vacancy	24-78
Micro vacancy	40
Dislocation	60
Screw dislocation	26
Grain boundary	9-49
TiC incoherent	60-129
V_4C_3 incoherent	40
Cementite/ferrite interface	11-18
Dispersed oxides	45
MnS	64
Ferrite/austenite interface	44
Al_2O_3	43-62
Fe_2O_3	43-62

Based on these considerations, traps can be divided into attractive and physical traps, although in most real cases a mixture of the two behaviours is observed. In attractive traps, the H atom is subjected to forces of different kinds that bind it to the site. When H dissolves into the crystal lattice, it transfers its electron to the metal's electron cloud. As a result, H tends to be attracted to imperfections or defects that have electron vacancies in order to achieve a more energetically stable condition. If the material is subjected to traction, H will tend to migrate to those areas of the crystal lattice that have expanded due to the stress. Finally, an increase in temperature causes an increase in the solubility of H; therefore, H atoms are attracted to areas with higher temperatures, such as the inner regions of a solidifying ingot. In a physical trap, the H atom is not attracted by a specific force; however, once trapped, its release is energetically more difficult. This type of trap owes its existence to modifications of the ideal crystal lattice, in which it is energetically more favourable for H to remain. Since a distortion of the crystal lattice is generally accompanied by electronic disorder, most real traps exhibit mixed behaviour, combining both attractive and physical characteristics. A prime example is edge dislocations, which act as mixed traps: the tensile stress field produces an attractive effect, while the dislocation core constitutes a physical trapping site. In pipeline steels, the main trapping sites are [65]:

- the grain boundaries of pre-eutectoid ferrite;
- the interfaces between ferrite and pearlite;
- the interfaces between the matrix and precipitates.

Among the most influential inclusions in the phenomenon of H diffusion are FeS and MnS, whose presence in modern steels is, however, significantly reduced. In fact, the sulphides formed during the hardening processes promote the formation of microvoids at the inclusion-matrix interface, due to the difference in the thermal expansion coefficients of the two materials. Large quantities of H atoms can accumulate in these microcracks, where they become permanently trapped [66] [67]. At this point, it is possible to modify Eq. 18 with the contribution of trapped H in Eq.19:

$$C_H = C_T + S \cdot \sqrt{f_H} \qquad \text{Eq. 19}$$

where C_T is the concentration of trapped H [68]. Figure 9 shows the equilibrium concentration of H with respect to the charging pressure for pure iron and three different steels.

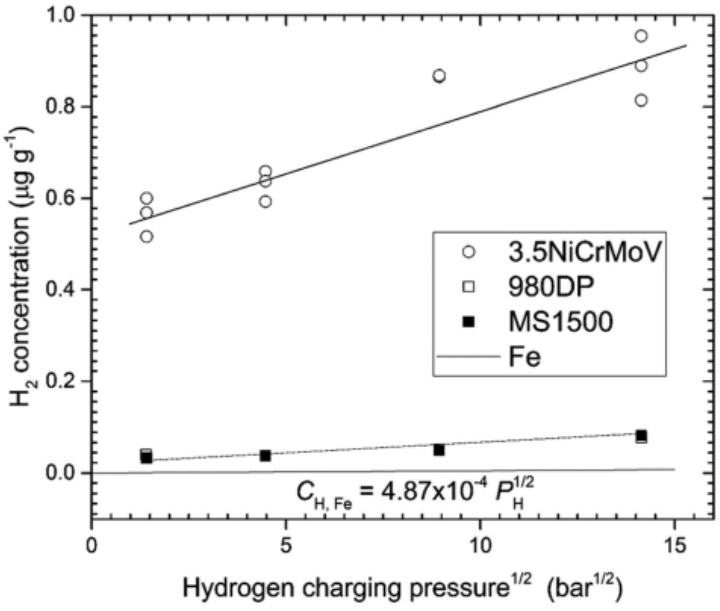

Figure 9-*Equilibrium H concentration for medium-strength steel (3.5NiCrMoV), high-strength steel (980DP and MS1500) and pure iron subjected to gas loading. The solubility of H in steel is greater than in Fe due to the large number of traps present [69].*

Traps have a significant influence on the H diffusion coefficient; for this reason, it is possible to introduce a new diffusion coefficient that takes this phenomenon into account, called the apparent diffusion coefficient, D_{app}. There are therefore two different diffusion coefficients:

- The apparent diffusion coefficient (D_{app}), which describes the behaviour of the system in the initial stages of the diffusion process, when the trapping sites are still free and gradually begin to saturate. A collection of the D_{app} values available in the literature for the main API 5L steels is provided in Table 6.
- The lattice diffusion coefficient (D_H), which represents the diffusion of H between the interstitial sites of the crystal structure, as described by equations 14 and 15. In this case, the system is considered to be at steady state, since the trapping sites are completely saturated.

Table 6-*Apparent diffusivity of H in different steels for pipelines.*

Steel	D_{app} at RT [m^2/s]
X52 [70]	$2.554 \cdot 10^{-10}$
X60 [71]	$2{,}25 \cdot 10^{-10}$
X65 [72]	$0.195 \cdot 10^{-10}$
X70 [73]	$0.263 \cdot 10^{-10}$
X80 [74]	$4.7 \cdot 10^{-11}$
X100 [75]	$1.04 \cdot 10^{-12}$
X120 [76]	$2.5 \cdot 10^{-11}$

1.3.3 Parameters affecting diffusion

Microstructure plays a fundamental role in H diffusion in pipeline steels [59]. Pearlitic microstructure is more susceptible to cracking than ferrite because it is harder and more brittle. H atoms tend to accumulate between pearlite lamellae, at ferritic grain boundaries and in the separation zones between inclusions and the metal matrix. When these atoms combine to form H_2 molecules, localised internal pressure is generated, which can trigger the formation of microcracks [77] (Figure 10). Martensite, on the other hand, offers maximum resistance to diffusion; however, this decreases following tempering due to the annihilation of defects [78]. The thin interlamellar cementite of bainite acts as a diffusion barrier [79] [80]. In martensitic steels, residual austenite does not have a strong trapping power, but the interfaces between austenite and martensite can represent areas of preferential accumulation [81]. The diffusion coefficient increases progressively from hardened to normalised and finally annealed steels, in relation to the reduction of defects and the increase in the ferritic fraction [82]. Welding processes modify the microstructures of pipeline joints, and this directly affects H permeation. FZ generally exhibits the highest permeation rate and the highest sub-surface concentration of H, due to the presence of fine acicular ferrite [83]. However, excessively high welding temperatures can cause grain growth and the formation of carbides and dislocations, reducing H permeability [84]. In the BM, phase interfaces facilitate H diffusion but also act as effective traps, leading to higher overall diffusivity but lower subsurface concentration [78]. In the HAZ, the presence of cementite precipitates, coarse grains and high microstructural heterogeneity limits diffusion, increasing trap density and reducing diffusivity [77]. Table 7 shows the H flow, diffusivity, H subsurface concentration and trap density obtained for the BM, FZ and HAZ of NG pipeline steel.

Table 7-*H permeation parameters in the welding of X80 pipeline steel [85].*

	Flow [$mol_H/m \cdot s$]	Diffusivity [m^2/s]	H sub-superficial concentration [mol_H/m^3]	Trap density [n°/m^3]
BM	$4.06 \cdot 10^{-10}$	$3.35 \cdot 10^{-11}$	12.12	$0.93 \cdot 10^{-27}$
FZ	$4.74 \cdot 10^{-10}$	$2.72 \cdot 10^{-11}$	17.43	$1.64 \cdot 10^{-27}$
HAZ	$2.49 \cdot 10^{-10}$	$1.49 \cdot 10^{-11}$	16.71	$2.88 \cdot 10^{-27}$

Grain size has a dual influence: finer grains increase the surface area of grain boundaries, which results in both preferential diffusion paths and reversible traps. It has been observed that there is an optimal grain size at which diffusion reaches its maximum value, balancing the accelerating effect of the edges and the braking effect of the triple joints. Numerical simulations on pipeline steels have confirmed that maximum diffusion occurs for an average grain diameter of around 40–50 μm [86]. The crystallographic texture also influences diffusion. Although knowledge in the field of pipeline steels is still limited, studies conducted on austenitic steels have shown that H atoms diffuse more rapidly in grains with <001>//ND and <101>//ND orientation than in those with <111>//ND orientation, due to the different atomic packing factor [87]. It is hypothesized that similar behavior may also occur in BCC steels used for pipelines, where <001>//ND oriented grains, which are less atomically dense, are more vulnerable to H cracking [88] [89].

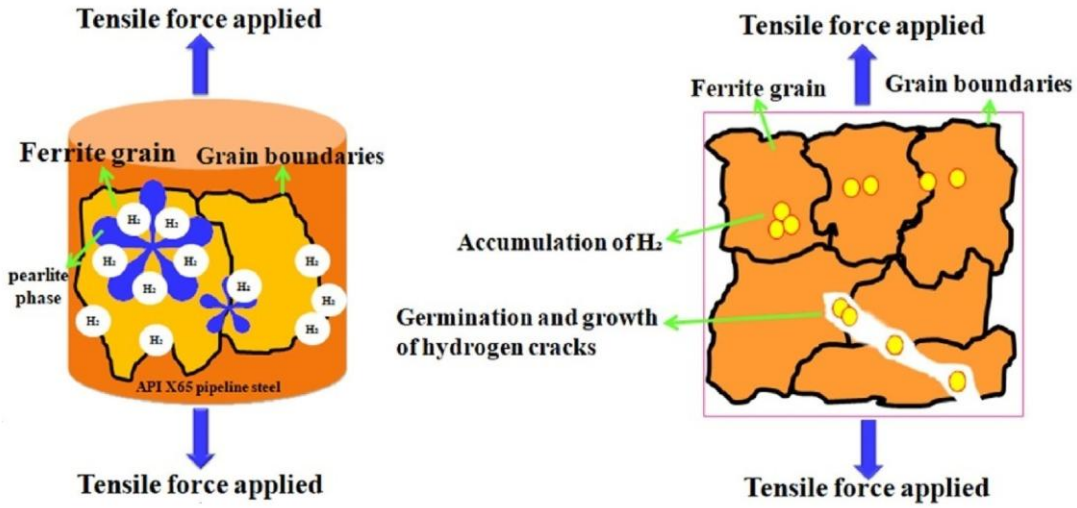

Figure 10-*H diffusion in the microstructure of pipeline steel [77].*

Dislocations act as weak traps, as H tends to agglomerate around them, forming a Cottrell atmosphere that reduces its mobility and causes localized hardening [90]. A high density of dislocations reduces the diffusivity of H and increases its concentration in areas subject to plastic deformation [91]. Cyclic deformation generates a dense network of fixed dislocations that limit the diffusion path of H, while reducing susceptibility to cracking [92]. In pipeline steels with different manganese contents, it has

been observed that the reduction of Mn and the consequent formation of finer carbides lead to lower diffusivity due to the increase in the concentration of trap sites [78]. Vanadium and niobium also produce small precipitates (V_4C_3, VC, NbC) that act as irreversible traps with high binding energy [93] [94]. The nature and coherence of the precipitates with the metal matrix are decisive: incoherent inclusions or those surrounded by cavities can trap greater amounts of H than coherent ones [95] [96]. Furthermore, the type of inclusion significantly modifies the diffusion behavior: the trapping efficiency increases according to the sequence TiN < $MgAl_2O_4$ < Al_2O_3 < MnS [97]. The latter type, particularly when elongated along the rolling direction, is known to trigger H cracks, especially when combined with mixed Mn/Al inclusions in ratio greater than 1[98]. The presence of mechanical stress, both elastic and plastic, has a significant effect on diffusion. In elastic conditions, the application of tensile stress causes the lattice to expand and reduces the energy barrier for H atom migration, thus increasing permeation [99]. During plastic deformation, on the other hand, the multiplication of dislocations generates new trapping sites which, while increasing the local concentration of H, reduce the overall diffusivity and permeability. Under compression conditions, on the contrary, the solubility and diffusivity of H decrease [100]. A uniform elastic deformation field increases the solubility of H according to Eq. 20 [33]:

$$C_H = C_0 \cdot e^{\frac{\sigma_0 \cdot V_H}{RT}} \qquad \text{Eq. 20}$$

Where C_H is the local H concentration at the point under triaxial stress, C_0 is the H concentration in areas not under stress, σ_0 is the hydrostatic component of the stress state, and V_H is the partial molar volume of H in the steel. Finally, the temperature at which permeation occurs plays a key role, as an increase in temperature causes an increase in the diffusion coefficient [101] [102]. In fact, it increases according to an Arrhenius law, as shown in Eq. 21 [103]:

$$D = D_0 \cdot e^{\frac{-E}{RT}} \qquad \text{Eq. 21}$$

Where D_0 [m^2/s] is the diffusion coefficient in the normal state, E is the activation energy required for H to jump from one lattice site to another, R [J/mol·K] is the gas constant, and T [K] is the absolute temperature.

1.3.4 Diffusion experiment with Devanathan-Stachurski cell

In 1962, Devanathan and Stachurski (DS) published an article describing the experimental apparatus they had designed to measure the instantaneous rate of electrolytic H permeation through a palladium sheet [104]. The principle of the method is that, under potentiostatic conditions, the concentration of H on the cathodic side of the sheet (H inlet) is kept constant while on the anodic side (H outlet) it is zero. The metal sample of interest is placed between two separate electrochemical cells, one for charging and one for discharging. In the first cell, the H^+ ions in the solution are reduced on the surface of the sample. At this point, the H atoms can recombine into molecules or pass through the metal membrane to be oxidized in the discharge compartment. The anodic background current is a direct measure of the instantaneous permeation rate according to Faraday's law (Eq. 22). This allows the H permeation rate to be recorded continuously with high sensitivity:

$$W = \frac{MM_H \cdot I \cdot t}{z \cdot F} \qquad \text{Eq. 22}$$

Where:

W = mass of H produced during the electrochemical reaction
MM_H = H atomic weight
Z = number of electrons exchanged in the electrochemical reaction
F = Faraday constant (96500 C)
I = anodic current required to oxidize the H atoms in the anodic compartment
t = time

In a typical DS cell experiment, on the cathode side, H is constantly generated at a controlled current to maintain stable conditions at the membrane inlet. On the anode side, however, complete oxidation of H is achieved by maintaining a constant potential such that the only possible reaction is the oxidation of H. The background current, established before the start of H transport, remains stable and much lower than the current due to the oxidation of H atoms. Subsequently, an increase in current is observed, which finally reaches a steady state value depending on the diffusion characteristics of H in the membrane (Figure 11).

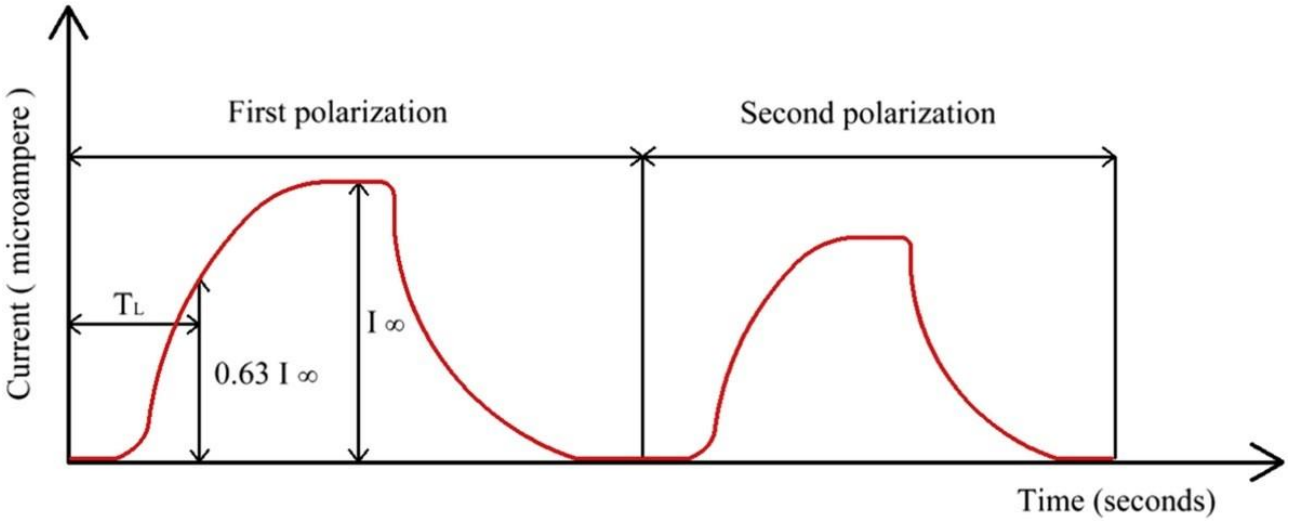

Figure 11-*Typical H permeation curve [105].*

However, the results obtained with this technique are influenced by two main factors: surface concentration of H and the analytical procedure used to obtain the diffusion parameters. With regard to the first aspect, the technique assumes that the surface activity of H remains constant throughout the entire duration of the test, although, except in cases where a thin layer of palladium is present, this condition is only achieved after a long period of stabilization [106] [107]. With regard to the second factor, it is necessary to consider the trapping effect, as it produces variations in apparent diffusivity [108]. The choice of specimen thickness is another critical parameter: the thickness must be sufficient for H diffusion to be controlled by transport in the metal bulk and not by surface processes, but not excessive to the point of making it difficult to maintain constant conditions during the test. Furthermore, an appropriate ratio between the radius of the exposed area and the thickness of the sample is necessary to ensure one-dimensional diffusion. The charging compartment can use H gas or an aqueous solution, chosen according to the operating conditions to be simulated or to facilitate permeation. The charging electrolyte, kept in static or recirculating conditions, may be the same as the anodic electrolyte [109] or may differ from it [110] [111] [112]. During the experiment, the discharge side of the sample tends to become passivated as it is subjected to an anodic current. This process compromises the results because the oxide is a H permeation barrier [113]. For this reason, it is recommended to cover the anodic side with a layer of palladium. It has two functions: to protect the sample from oxidation and to prevent H atoms from recombining into molecules [114]. The permeation test with a DS cell, standardized as ASTM G148 [115] and ISO 17081 [108], allows the diffusion coefficient, flow, H subsurface concentration, and concentration of reversible and irreversible traps to be obtained (see chapter 2.2.4).

1.4 Cathodic Hydrogen Charging

H can be introduced into steel by gas phase charging or electrochemical charging. Although gas phase charging more realistically replicates actual operating conditions, electrochemical charging offers several significant advantages:

- Greater H absorption efficiency, allowing for faster evaluation of materials. This method is an effective screening tool: if a material resists electrochemical charging, it is very likely to perform well with gaseous H as well [116];
- Lower costs and experimental complexity, with reduced safety risks compared to high-pressure gas testing [117];
- Ability to simulate real operating conditions, such as those of a pipeline in contact with the ground in the presence of coating defects and cathodic protection [118].

Although the generation of H atoms and their absorption on the steel surface differ significantly between the two mechanisms, the absorption of atomic H, its diffusion through the crystal lattice, and its interaction with trap sites remain largely similar, or even identical, for both charging methods [49] [50]. However, differences in the activation of diffusible H traps have been observed between electrochemical and gas-phase charging, mainly due to different H fugacity conditions [119]. The two main operating configurations for electrolytic charging are galvanostatic mode, in which a constant current is set, and potentiostatic mode, in which a constant potential is set. The former method allows high absorption rates to be achieved in relatively short time, making it particularly useful for material screening tests. However, the potential can reach very low (cathodic) values in an attempt to sustain the imposed current. This leads to intense H evolution, which can alter the morphological conditions of the sample surface, reducing the effective efficiency of H entry into the lattice and promoting undesirable phenomena such as bubble formation or the removal of protective surface films [120] [121]. In potentiostatic mode, the current adapts to the kinetics of the surface and the state of H saturation in the material, making it particularly suitable for studying the equilibrium between absorbed and dissolved H. However, compared to galvanostatic charging, the total amount of H introduced may be lower for the same amount of time, thus requiring longer times to reach the saturation level of the metal [122]. Further complicating the interpretation of the results obtained by electrolytic charging is the fact that there is no universally recognised experimental protocol for performing the tests.

The definition of the procedure therefore requires careful evaluation of various operating parameters, including:

- the pH of the charging solution;
- the addition of a H recombination inhibitor;
- the current density or potential applied during charging;
- the duration of exposure to the electrolytic environment.

Experimental results show that acidic solutions are more efficient than others in charging H [123]. This is attributed to different H generation mechanisms in different environments, which lead to different H concentrations at the metal/electrolyte interface, and to the presence of an oxide layer on the surface [124], which can hinder H absorption and therefore its diffusion into the metal, particularly in alkaline environments with a pH higher than 10 [125]. Generally, an increase in charging time results in greater H absorption into the material [126] [127]. However, for prolonged charging periods, there may be a decrease in the rate of H entry due to the formation of oxide on the sample [128]. Similarly, if the charging density increases (more current is sent to the cathode for HER), the amount of H produced and therefore absorbed also increases [77] [129]. During electrochemical charging, it is essential to use a recombination poison, i.e. a substance that prevents H atoms from recombining into H_2, thus increasing the efficiency of the charge. The most commonly used poisons are sulphur-based [130] [131] [132] and arsenic-based compounds [133] [134] [77]. Hydrogen sulphide, present as a contaminant in natural gas and petroleum, promotes the absorption of H in steels in accordance with Eq. 23 [135]:

$$H^+_{(aq)} + HS^-_{ads} \rightarrow (HSH) \overset{e^-}{\rightarrow} HS^-_{ads} + H_{ads} \qquad \text{Eq. 23}$$

Nowadays, thiourea (TU, CH_4N_2S) and ammonium thiocyanate (NH_4SCN) are widely used due to their excellent efficiency, low cost and toxicity [136] [137] [138]. TU inhibits the formation of H_2 by specific adsorption on the surface of the sample, limiting the surface area available for H adsorption [139].

1.5 HE Mechanism

Over the years, various mechanisms have been proposed to explain the advancement of a hydrogen-assisted crack. Among the best known are Hydrogen Enhanced Decohesion (HEDE), Hydrogen Enhanced Local Plasticity (HELP), Adsorption-Induced Dislocation Emission (AIDE), and Hydrogen-Enhanced Strain-Induced Vacancies (HESIV). In many cases, the embrittlement of the material is not attributable to a single phenomenon, but rather to a combination of several mechanisms acting simultaneously. Despite the considerable progress made in recent decades, the dominant mechanism responsible for embrittlement remains a subject of debate, and research continues with the aim of clarifying it definitively [140]. The HEDE theory was formulated in 1926, when it was first hypothesised that the presence of H could reduce the energy of intermolecular bonds in metallic structures [141]. The concept was subsequently refined, leading to the theory that H atoms in the metal lattice decrease the local cohesion between metal atoms, promoting the nucleation and propagation of microcracks even under low stress levels [142] (Figure 12a). The weakening of interatomic bonds is attributed to the tendency of the 1s electron of H to migrate towards the 3d orbitals of iron atoms. Electron transfer increases interatomic repulsion and, as a result, reduces the cohesive strength of lattice planes or grain boundaries [143]. When cohesion is sufficiently reduced, fracture can occur by cleavage once the critical crack opening is reached [144]. The determining factor in the HEDE model is the localised accumulation of H at the crack tip. The determining factor in the HEDE model concerns the localised accumulation of H. High concentrations of H must accumulate in the area of maximum hydrostatic stress, i.e. near the tip of the crack [145]. Simulations and experimental measurements have confirmed this possibility: for example, in pure iron, the elastic stress can reach values of up to 20,000 MPa a few tens of nanometres from the tip of the crack, which is sufficient to attract H and promote the phenomenon [146]. The sites most frequently associated with this mechanism are grain boundaries and phase interfaces, which is why intergranular fractures are commonly related to the phenomenon [147]. The HELP mechanism was first proposed in 1972 [148]. It is based on the hypothesis that H accumulated near the tip of the crack reduces the resistance to dislocation movement, increasing their mobility and facilitating local plastic deformation [149] [150] (Figure 12b). H causes a decrease in local yield strength, allowing dislocations to move even under low stress levels. This leads to the formation of slip bands and localised plastic deformation near the tip of the crack, phenomena frequently observed on the fracture planes of embrittled materials [151]. It was noted that as the stress decreased, the fracture evolved from ductile behaviour to quasi-brittle and finally intergranular fracture, confirming the role of increased local plasticity [152]. The mechanism was subsequently consolidated on the basis of elasticity theory and transmission electron

microscopy (TEM). It was demonstrated that H produces a shielding effect on dislocations (e.g. dislocations with the same sign as the Burgers vector, precipitates, interfaces), allowing them to flow more easily [153]. Several macroscopic evidences are consistent with the HELP model. For example:

- the reduction in flow stresses in the presence of H compared to H-free samples [154];
- the presence of more superficial dimples in the fractures of H charged materials [149];
- the high density of dislocations beneath the fracture surfaces of cleavage or H-induced intergranular fractures [155].

However, the model also has some critical issues related to the diffusion time of hydrogen: the model would require H to reach the tip of the crack before its propagation, but in many cases the crack advances faster than H [156]. For this reason, it is generally believed that HELP acts in combination with other embrittlement mechanisms, contributing significantly to the loss of ductility but not being the sole cause of fracture [157]. The AIDE mechanism describes a embrittlement process in which H adsorbed on surfaces subject to high stress concentration promotes the nucleation of dislocations and, consequently, crack propagation. It is often interpreted as a combination of the HEDE and HELP mechanisms, as it involves both the weakening of interatomic cohesion and the movement of dislocations [152] [158]. The first experimental evidence attributable to AIDE dates back to 1972, when numerous pits were observed by TEM on the fracture surfaces of steels subjected to high stress intensities, interpreting them as the result of micro-pore aggregation and as a possible crack propagation mechanism (Figure 12c). Based on these observations, the model was proposed in 1979, arguing that dislocation nucleation occurs through the breaking and subsequent reformation of atomic bonds in the material, a process significantly facilitated by hydrogen adsorbed at the tip of the crack [159]. In the model, H modifies the surface energy, promoting or in some cases inhibiting the nucleation of dislocations [160]. H therefore plays a key role: it facilitates the nucleation of dislocations, weakens interatomic bonds, allowing dislocations to reach the surface of the crack. Their activity and the formation of micropores determine the progression of the fracture. This behaviour differs from that predicted by the HELP mechanism, in which it is the greater mobility of dislocations in the plastic zone that promotes crack growth [19]. However, although much indirect evidence supports the model, there is still a lack of direct and definitive experimental evidence for the entire process of AIDE, which is why the precise role of AIDE is still a matter of debate in the scientific community [19]. The HESIV mechanism interprets embrittlement as the result of the increase and stabilisation of vacancies generated in regions with high deformation concentration (Figure 12d). Thermal desorption tests showed that below 200 °C, the temperature at which the dislocation density did not appear to change, there was a decrease in the H desorption rate. This reduction was therefore

interpreted as the result of vacancy annihilation [161]. From the thermal data, it was deduced that the density of deformation-induced vacancies increased significantly in the presence of H, leading to the formulation of the HESIV model [162]. The validity of the mechanism was further supported by positron annihilation spectroscopy (PAS) analyses, which showed an increase in the average lifetime of positrons in iron samples subjected to traction, an increase that was further accentuated when the samples had been previously charged with H [163]. Once stabilised, these vacancies tend to aggregate to form clusters and subsequently small nanometric voids, which can drastically reduce local fracture resistance in areas of high stress concentration, such as crack tips. Significant evidence of this phenomenon comes from high-resolution scanning electron microscope analyses, which identified fracture surfaces characterised by a mottled contrast on a nanometric scale, interpretable as the presence of nanodimples attributable to the nucleation of voids starting from vacancy clusters [164]. Further evidence was obtained by analysing samples subjected to fatigue in H environments, where a high pore density was detected compared to reference samples, indicating a marked synergy between H and vacancies in promoting the nucleation of micropores. Thermal desorption studies and atomistic simulations have shown that the energy of H trapped within a vacancy is reduced, facilitating the formation of micropores and thus the loss of ductility and crack propagation [165]. However, experimentally distinguishing the HESIV mechanism from other embrittlement models is a significant challenge. The deformation microstructures and fracture morphologies produced can, in fact, be similar to those generated by other mechanisms based on dislocation activity, making it difficult to isolate the exclusive contribution of vacancy clusters [166]. Furthermore, since the HESIV model assumes the existence of a local plastic zone at the tip of the crack, it is not self-consistent in describing the entire embrittlement process and it is often necessary to integrate it with other mechanisms in order to fully explain HE [56].

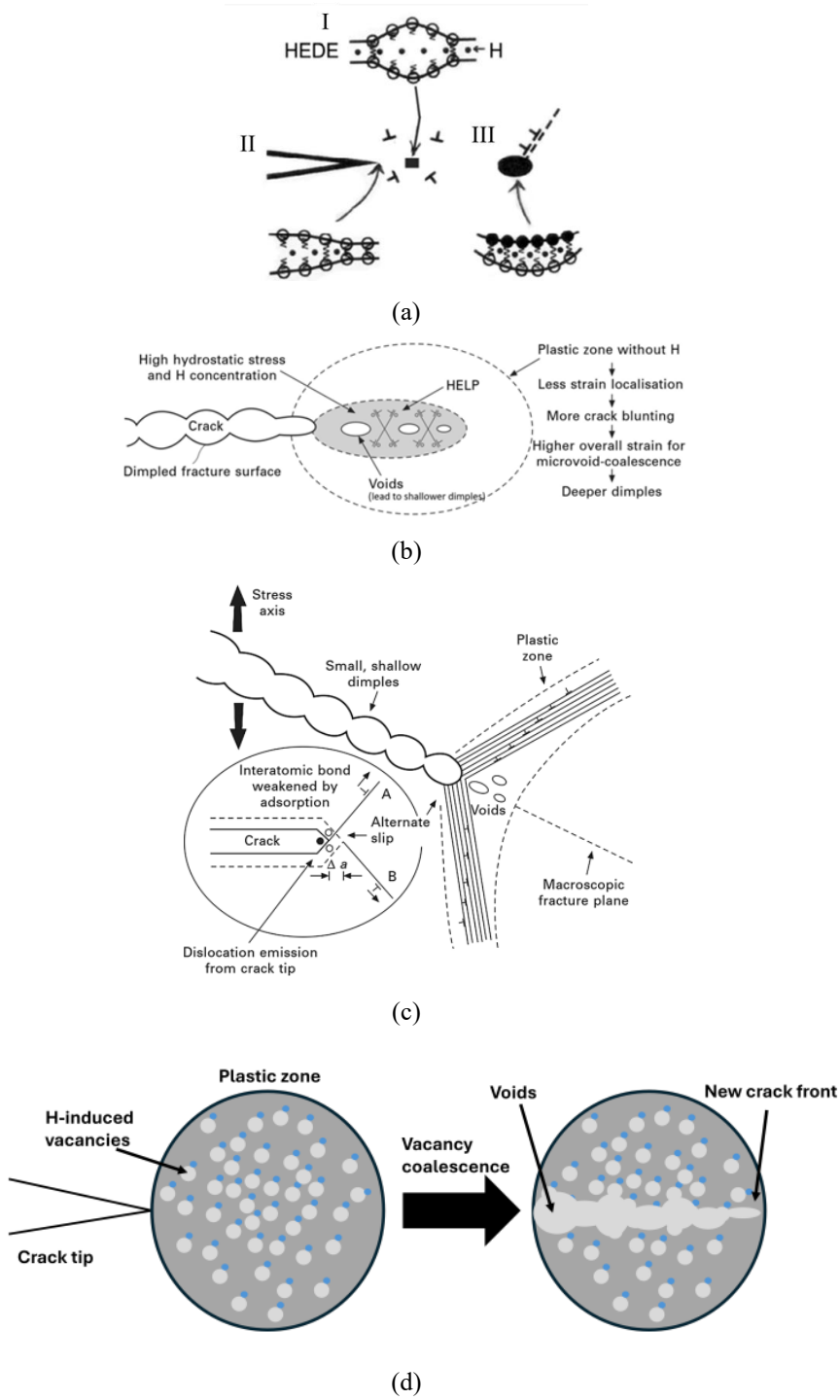

Figure 12-*Sketches of HE mechanisms.* (a) *HEDE. The separation of atoms due to the weakening of interatomic bonds is caused by (I) H in the lattice, (II) adsorbed H, (III) H at particle-matrix interfaces [167].* (b) *HELP. The presence of H promotes dislocation mobility and the localisation of plastic deformation at the crack tip; crack propagation occurs through a process of microcavity coalescence in this area of hydrostatic stress and high H concentration [168].* (c) *AIDE. Embrittlement consists of two phases: local reduction of the cohesive energy of the material, which promotes the nucleation and emission of dislocations from the crack tip; nucleation and growth of microcavities in front of the crack tip. (Δa is the crack growth length).* (d) *HESIV. H promotes the coalescence of vacancies into microvoids that promote crack growth [169].*

1.6 Introduction to Fracture Mechanics

Understanding fracture mechanisms is a central theme in materials engineering, since the failure of a component marks the end of its service life. Analysing the ways in which a material is damaged not only makes it possible to prevent catastrophic failures, but also allows for the design of more efficient, safer and longer-lasting structures. The fracture surface can generally be ductile or brittle. Ductile fracture is the result of the nucleation, growth and coalescence of microscopic voids that begin at inclusions and second-phase particles. Brittle fracture can be of two types, cleavage and intergranular: the former involves separation along specific crystallographic planes and the fracture path is transgranular, while the latter occurs along grain boundaries (Figure 13). In general, metal structures are designed and tested to withstand a portion of the stress value taken as a reference depending on the type of stress acting (static, dynamic, cyclic). However, breakage phenomena may occur that are not adequately addressed by this type of approach. In fact, sudden collapses can also occur at stress values significantly lower than the yield strength, which is generally taken as a reference value for static stress. In such cases, we can speak of engineering brittle fracture, which occurs at extremely high speeds and without plastic deformation. Brittle failures can have disastrous consequences in terms of human safety and costs.

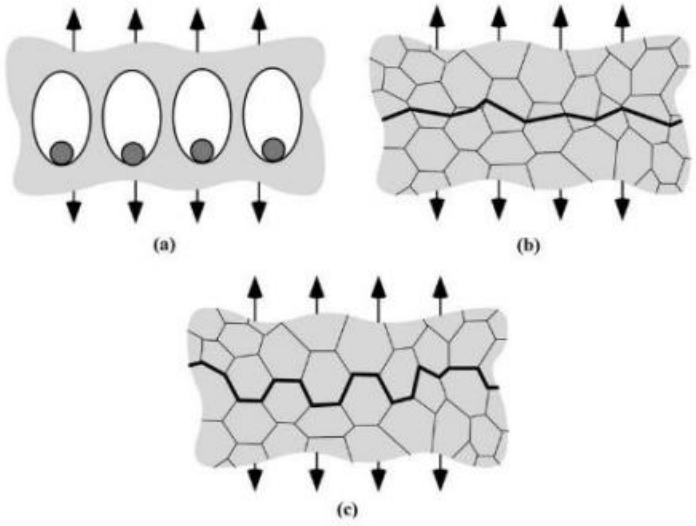

Figure 13-*Sketch of metal fracture mechanisms*. (a) *ductile;* (b) *cleavage;* (c) *intergranular [170].*

Examples are the American Liberty tankers. To meet the high demand for vessels to be used in World War II, it was decided to build ships with an almost entirely welded structure and extensive use of prefabricated metal parts. The welded hull, effectively a continuous sheet of steel, allowed small cracks to spread unimpeded, unlike a hull made of separate plates riveted together. The cracks

originated at the right-angled corners of the hatches and then spread silently to the hull, leading to catastrophic failure [171].

In 1967, the St. Mary's Bridge in West Virginia collapsed due to a crack caused by friction on a bearing and exacerbated by stress corrosion. More recently, in 2010, a natural gas pipeline exploded in San Bruno, California, due to a welding defect that had not been detected when the pipe was manufactured in 1956 [172]. Historically, the first assessments of the behaviour of components containing discontinuities were conducted in 1913 by Inglis [173], who developed an analysis of the stress state induced by the presence of an elliptical hole in a large flat plate subjected to a uniform tensile stress distribution s as shown in Eq. 24.

$$\sigma_{max} = \sigma_{nom}\left(1 + 2\sqrt{\frac{a}{p}}\right) \quad \text{Eq. 24}$$

Where: σ_{max} is the local peak stress at the notch tip; σnom is the nominal stress in the component, i.e. the stress in the component assuming no discontinuities; a is the hole radius, p is the hole curvature radius.

The stress concentration factor at the notch tip is therefore equal to (Eq. 25):

$$\frac{\sigma_{max}}{\sigma_{nom}} = \left(1 + 2\sqrt{\frac{a}{p}}\right) \quad \text{Eq. 25}$$

This ratio tends to infinity for values of r that tend to zero (in the case, for example, of two-dimensional defects with sharp corners). However, Inglis was unable to explain why brittle materials break at stresses much lower than their theoretical strength. In 1921, Griffith resolved this limitation by introducing an energy-based approach: fracture progresses when the elastic energy released exceeds the energy cost required to create new surfaces [174]. The origins of modern fracture mechanics theory can be traced back to the analyses conducted by Irwin, based on the concepts developed by Griffith and a method developed by Westergaard [175] in 1939 for analysing the state of stress and strain at the apex of two-dimensional defects. Irwin demonstrated that the stresses and strains that occur near the tip of a two-dimensional defect can be characterised by a single parameter: the stress intensity factor, K [MPa√m] [176]. A two-dimensional defect can propagate in three different ways: detachment, sliding and tearing. The first is the most significant from an engineering point of view, since the propagation of two-dimensional defects occurs preferentially in direction orthogonal to the maximum principal stress (Figure 14).

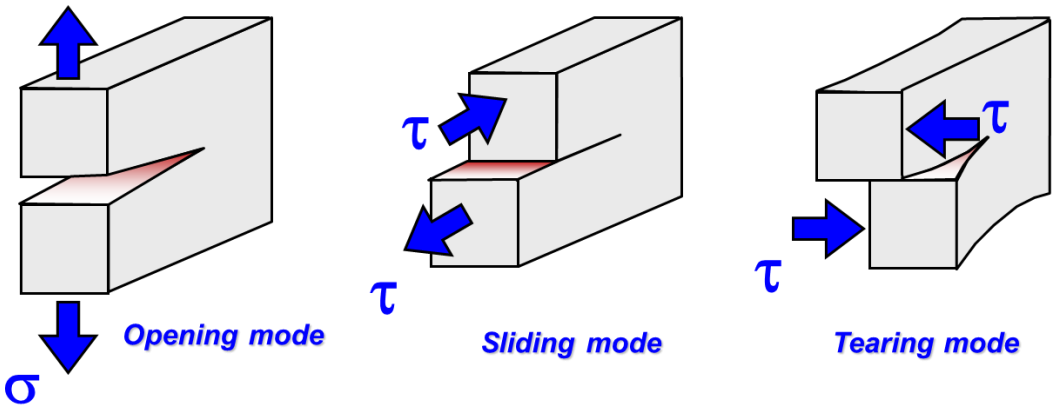

Figure 14-*The three modes of crack surface displacement. σ is the stress normal to the crack plane, τ parallel to the crack plane.*

For the first method (in which K is referred to as K_I), the analytical expressions describing the stress state at the tip of the defect are (Eqs. 26, 27, 28, 29, 30):

$$\sigma_x = \frac{K_I}{\sqrt{2\pi r}}\cos\frac{\theta}{2}\left[1 - \sin\frac{\theta}{2}\sin\frac{3}{2}\theta\right] \quad \text{Eq. 26}$$

$$\sigma_y = \frac{K_I}{\sqrt{2\pi r}}\cos\frac{\theta}{2}\left[1 + \sin\frac{\theta}{2}\sin\frac{3}{2}\theta\right] \quad \text{Eq. 27}$$

$$\tau_{xy} = \frac{K_I}{\sqrt{2\pi r}}\sin\frac{\theta}{2}\cos\frac{\theta}{2}\cos\frac{3}{2}\theta \quad \text{Eq. 28}$$

$$\sigma_z = \nu(\sigma_x + \sigma_y) \quad \text{Eq. 29}$$

$$\tau_{xz} = \tau_{yz} = 0 \quad \text{Eq. 30}$$

Where θ is the direction relative to the tip along which the stress components are evaluated and ν is Poisson's ratio. At this point, K is defined as (Eq. 31):

$$K = Y\sigma\sqrt{\pi a} \quad \text{Eq. 31}$$

Where Y is a shape factor that depends on the geometry of the material, σ [MPa] is the applied stress, and a [m] is the size of the defect. K characterises the stress field near the apex of the defect, defining the width of the singularity zone (the region surrounding the apex of the defect, where stresses are very intense) and the severity of the stress state.

The defect can propagate in two ways:

- unstable (brittle fracture)
- stable (subcritical propagation of the defect, e.g. due to fatigue, stress corrosion or viscous creep at high temperatures).

Unstable propagation occurs when stresses and strains at its apex reach critical values, i.e. when K_I reaches a critical value called K_{IC}. The energy expended for the propagation of the defect per unit area of the defect itself is given by (Eq. 32):

$$G = \frac{dU}{Bda} \quad \text{Eq. 32}$$

Where B is the thickness of the metal plate, d is the increase in the defect and *d*U is the reduction, due to the increase in the length of the defect, of the elastic energy present in the plate. The relationship between K and G is given by the equation (Eq. 33):

$$G = \frac{K^2}{E'} \quad \text{Eq. 33}$$

Where E' is the elastic modulus in a flat state during deformation.

It is very important to remember that K was introduced in the hypothesis of linear elastic behaviour of the material (linear elastic fracture mechanics, LEFM). The conclusions are therefore valid as long as the plastic zone at the tip of the crack remains very small compared to the geometric dimensions. This condition of negligible macroscopic plastic deformation is generally well verified in materials with a high yield strength and in thick pieces, but it is a serious limitation in the case of the most common structural materials. In these cases, the use of LEFM leads to overly cautious solutions and a significant underutilisation of the material; in fact, the real critical condition of unstable fracture propagation in these cases occurs for K_I values well above K_{IC} [177]. Before unstable defect propagation occurs, the plastic zone reaches dimensions that render the Linear Elastic Fracture Mechanics Theory inapplicable. In particular, when the dimensions of the plastic zone at the apex of the defect are of the same order of magnitude as the smallest dimensions characterising the system, it is necessary to resort to an alternative treatment: Elastoplastic Fracture Mechanics (EPFM). In 1968, Rice [178] introduced the concept of the J integral [kJ/m^2], which is defined by the following equation (Eq. 34):

$$J = \int_{\Gamma}^{0} \left[W\, dy - t \left(\frac{du}{\partial x_1} \right) ds \right] \quad \text{Eq. 34}$$

Where $W = \int_0^{\varepsilon} \sigma d\varepsilon$ is the deformation energy density, ε is the infinitesimal deformation tensor, Γ is any closed path around the crack in an anti-clockwise direction, t is the traction vector, u is the displacement vector, and ds is the curve increment. J therefore represents the rate of energy release associated with the advancement of the defect. Under LEFM conditions, the integral J coincides with the energy release rate G. Therefore, in accordance with Eq. 33, it is possible to derive K from J and viceversa. As with K, it is also possible to identify a critical value of J (J_{IC}) for which unstable defect

propagation occurs. If the test is conducted in a hydrogenated environment, K_{IC} and J_{IC} are called K_{IH} and J_{IH}.

1.7 Mechanical testing in hydrogen

The assessment of HE in pipeline steels is an essential step in ensuring their fitness for service with H_2/NG mixtures and pure H_2. Despite the extensive scientific literature on the subject, the lack of a universally recognised test method makes it difficult to compare results obtained with different approaches, parameters and environmental conditions. However, the main international standards converge on a set of mechanical tests considered most effective for characterising these materials: tensile tests (on smooth, notched and hollow specimens), fracture toughness tests (specimens with defects) and fatigue tests for assessing crack propagation velocity. Below, these test methods will be described individually with the relevant regulatory references. The aim is providing a clear and consistent picture of the tools currently available to characterise the performance of gas pipelines in a hydrogenated environment.

1.7.1 Regulatory framework

The international standards currently available propose different testing methodologies, which in some cases can lead to incomparable or even divergent results. The main reference standards that define the criteria for assessing the compatibility of metallic materials with H are ASME B31.12 [179], ASME VIII Div.3 Art. KD-10 [180], ISO 11114-4 [181], CHMC-1 [182] and EPRG [183]. These documents illustrate the test methods considered suitable, how to interpret the results and the relevant operating conditions, with particular attention to high-pressure systems, in which embrittlement phenomena are more critical. The standards focus on steels intended for components such as pipes, tanks, valves and fittings designed for use in H service; when a material passes the set of tests required by a specific standard, it is considered suitable for use according to that technical reference. which define the criteria for assessing the compatibility of metallic materials with H. According to ASME VIII Div. 3 art. KD-10, materials must be characterised by fracture mechanics tests, obtaining in particular the H environment toughness K_{IH} and the fatigue crack propagation curves $da/dN-\Delta K$. Unlike ISO 11114-4, ASME explicitly recognises that pressure vessels are welded structures. Consequently, the required parameters must be determined separately for BM, FZ and HAZ, and for each welding procedure adopted. The K_{IH} measurement must be performed according to ASTM E1681, using constant load or displacement test pieces (the applied load, K_{IAPP}, is suggested by the standard). According with KD-10, the tests must be conducted in an autoclave with high-purity

H (O_2, CO and $CO_2 \leq 1$ ppm; $H_2O \leq 3$ ppm) for 1000 hours. The outcome of the test depends on crack propagation:

- if the propagation is less than 0.25 mm under constant load conditions, $K_{IH} = K_{IAPP}$; under constant displacement conditions, $K_{IH} = 0.5\ K_{IAPP}$.
- if the propagation is greater than 0.25 mm, K_{IH} is calculated as described in ASTM E1681 [184].

KD-10 standard also requires the determination of the fatigue crack growth curve in the same test environment, imposing a maximum frequency of 0.1 Hz to allow H diffusion and thus evaluate more severe embrittlement conditions. For austenitic stainless steels, characterised by very low H diffusion coefficients, even lower frequencies would be necessary to capture the actual behaviour in H. The ASME B31.12 standard, while not providing its own methods, refers entirely to KD-10 and establishes a minimum threshold reference value for K_{IH} of 55 MPa√m.
The CHMC standard, dedicated to assessing the compatibility of metals with compressed H, proposes a comprehensive set of experimental methodologies designed to provide a broader picture of the response of materials in the presence of H. The tests must be performed in high-purity H, with very strict limits on impurities ($O_2 \leq 1$ ppm, $CO_2 + CO \leq 2$ ppm, $H_2O \leq 3.5$ ppm, $N_2 \leq 2$ ppm). The test pressure cannot be lower than the maximum working pressure for the component, while the temperature must coincide with that at which the material exhibits maximum susceptibility to embrittlement, defined according to the guidelines provided by the standard itself. Chapter 5 of the standard describes the applicable test methodologies, which include:

- SSRT tests, conducted on smooth or notched specimens, with strain rates of 10^{-5} s^{-1} for smooth specimens and 10^{-6} s^{-1} for notched specimens, measured over a working length of 25.4 mm;
- determination of the H-assisted fracture threshold with K_{IH} or J_{IH} fracture mechanics testing
- fatigue crack propagation tests, conducted in H at a frequency of 1 Hz and with a load ratio R = 0.1, for the definition of the da/dN–ΔK curve;
- fatigue life tests, with S–N curves obtained under load or deformation control, at 1 Hz for low-cycle fatigue and 20 Hz for high-cycle fatigue.

The material qualification process, described in chapter 6, is structured with the aim of reducing the number of tests required (Figure 15). First, the relative notch tensile strength (RNTS) and the relative

reduction of area (RRA) are defined. The first is the ratio between the breaking load of a specimen cut in H and a reference specimen in inert environment, the second is the ratio between the reduction in area in H and the reduction in area in inert environment (smooth specimens may be used). The tensile strength and reduction in area values must be obtained from the average of the results of three specimens. If the material is an aluminium alloy or austenitic stainless steel and the test yields an RNTS or RRA ≥ 0.90, then the material is H compatible. For all other materials, and for those that do not meet this threshold, the minimum acceptable limit is RNTS ≥ 0.50. If this value is met, the material must then undergo advanced testing (K_{IH}/J_{IH} toughness, FCGR or S–N), depending on the type of application for which it is intended.

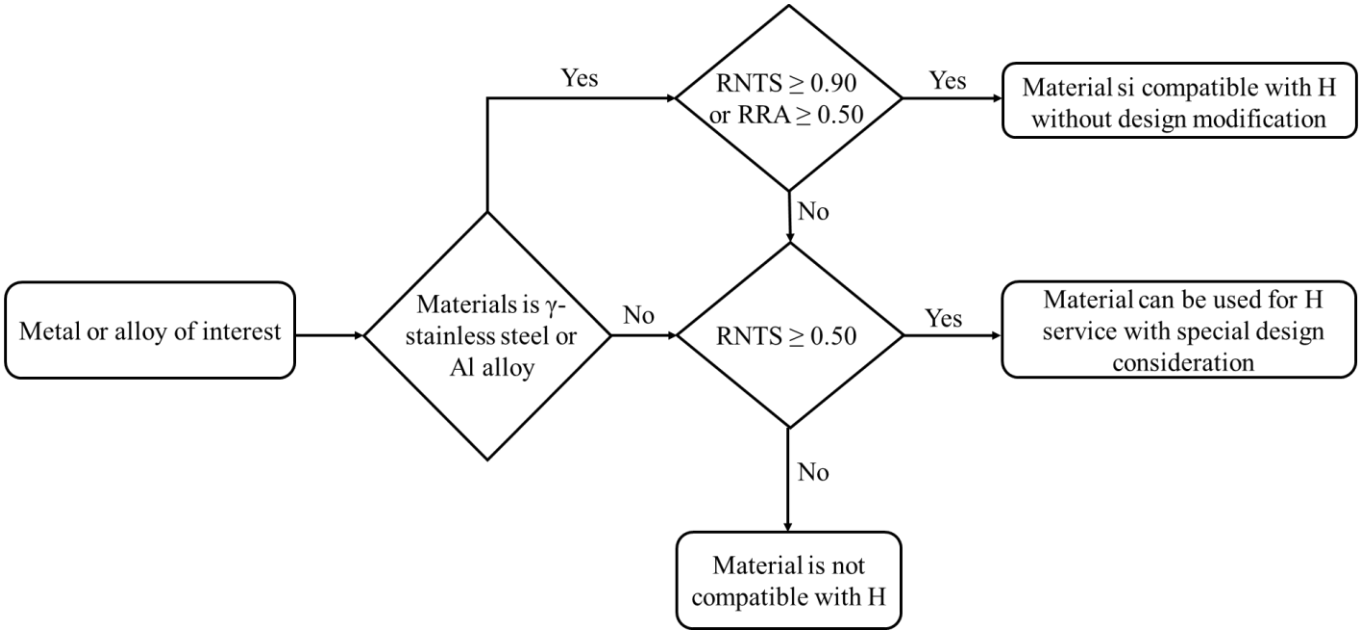

Figure 15-*Qualification scheme for a metallic material according to the CHMC code.*

ISO 11114-4 defines three different test methods for assessing the compatibility of metallic materials with high-pressure H. Method A, known as the disk rupture test and equivalent to ASTM F1459 [185], consists of measuring the rupture pressure of a metal disk in H and He. The material is considered suitable if the ratio between the rupture pressure in He and H is ≤ 2. Although this is a rapid method, it has several limitations: it uses very thin test pieces (0.75 mm), which are not representative of actual components, does not take into account the presence of defects and does not provide engineering parameters useful for design, relying instead on an empirical criterion [186]. Method B involves a constant load fracture mechanics test to determine K_{IH} at the same working pressure as the material. The specimens must have a thickness of at least 85% of that of the actual component. During the test, the load must increase by 1 $MPa \cdot m^{0.5}$. The material is considered suitable for service in H if the value obtained is equal to or greater than the limit imposed by the standard,

calculated as 60/950×R_m, where R_m represents the average breaking load measured on two specimens of the same material. Unlike method A, the K_{IH} parameter obtained in this way has real engineering value, as it allows the result to be used directly in the subsequent stages of pressure vessel design. However, it requires sophisticated experimental equipment and stringent safety standards in order to work with high-pressure H. Method C has a test protocol similar to method B. The characteristics of the test pieces are the same as those required by method B, but before exposure to H, each test piece is preloaded to a predetermined level of deformation using a formula specified in the standard, so that an initial K_{IAPP} value of 1.5×60/950 R_m is applied. The tests must last at least 1000 hours. A material is considered suitable for service in H if, at the end of the test:

- the average crack growth does not exceed 0.25 mm, or
- the crack grows beyond 0.25 mm, but the final K_I value remains not less than the limit of 60/950 R_m.

Despite its relative simplicity of application, this method is generally considered less conservative than method B and, for this reason, its revision has long been the subject of discussion within regulatory bodies [187].

The EPRG (European Pipeline Research Group) standard focuses on fracture mechanics tests for the determination of J_{IH}. Test specimens must be manufactured to full thickness; if smaller specimens are used, they must be extracted as close as possible to the inner wall of the pipe in order to sample the microstructure in contact with H gas, where the expected H concentration will be highest. The longitudinal weld must be extracted according to ASTM E399 [188] with C-L orientation (the crack grows through the thickness), while the girth weld must be extracted with L-C orientation (the crack advances parallel to the rolling direction). The fracture mechanics test can be performed in accordance with ASTM E1820 [189] or ISO 12135 [190] using the unloading compliance or direct current potential drop method. The multi-specimen technique is not included but is recommended for verifying the curve obtained. Since crack growth monitoring in H tests has limited resolution, the standard indicates that it is not possible to accurately identify the start of crack propagation.

For this reason, an engineering definition is suggested: the value of J at crack growth equal to 0.05 mm, indicated as $J_{0.05}$, to be taken as the threshold toughness. At this point, the parameter must instead be used within an engineering integrity assessment to verify that the operating stresses do not exceed the H-assisted fracture threshold.

1.7.2 Overview of Mechanical Testing

Slow Strain Rate Tests (SSRT) are one of the most widely used experimental methods for assessing the susceptibility of metallic materials to HE. The logic behind these tests stems from the fact that HE is a phenomenon controlled by H diffusion and its ability to accumulate in areas of high plastic deformation: the application of a low strain rate therefore allows H to interact more effectively with the material and reveal its actual vulnerability. SSRTs can be performed on three types of specimens: smooth (ASTM G129 [191]), notched (ASTM G142 [192]) and hollow (ISO 7039 [193]) (Figure 16). In a hydrogenated environment, the yield strength (YS) and ultimate tensile strength of smooth specimens remain almost unchanged compared to values in air, while those related to elongation at break and reduction in area (Z) show relevant decreases [194]. The curve in H tends to coincide with that in air up to the maximum load; subsequently, there is a deviation in the necking phase when the triaxial stress state favours the local accumulation of H and the onset of damage. In some studies [29] [195] [196], the loss of mechanical properties is commonly correlated with an embrittlement index (EI), which is often evaluated in relation to Z and expressed as a percentage, according to equation 35:

$$EI = \frac{Z_{Air} - Z_{H_2}}{Z_{Air}} \qquad \text{Eq. 35}$$

where Z_{air} and Z_{H2} are, respectively, the reduction in the area of the test specimen in air and in H environment. The EI parameter could be useful for comparing data obtained using gaseous and electrolytic methods, as it evaluates the brittle behaviour of the test specimen, regardless of the technique used. Pipeline steels begin to show an appreciable reduction in ductility parameters even at very low pressures, in the order of tens of kPa; however, once a threshold typically between 50 and 100 bar is exceeded, a clear plateau is observed: further increases in pressure do not cause mechanical degradation comparable to that recorded in the transition from lower to intermediate pressures. The appearance of the plateau is interpreted as the result of a balance between surface absorption and internal diffusion: once H has significantly occupied the available sites in the plastic zone or in front of the crack front, the process is no longer limited by the flow from the external environment, but by the material's ability to redistribute it internally [188].

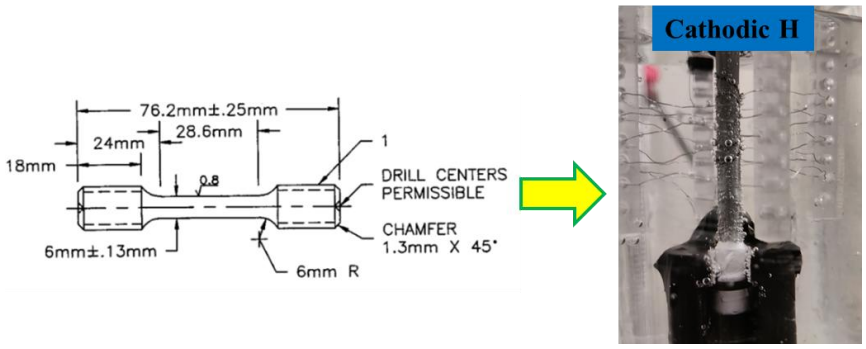

(a)

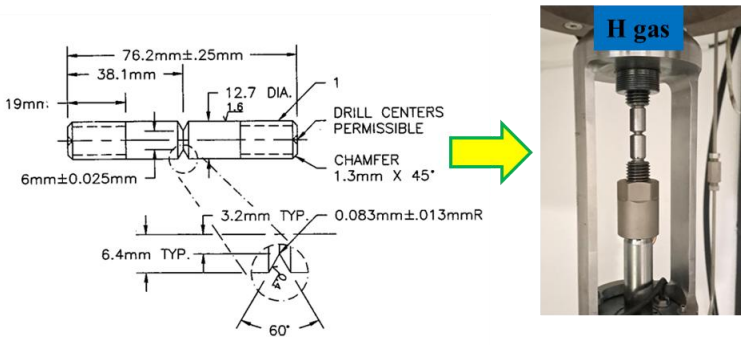

(b)

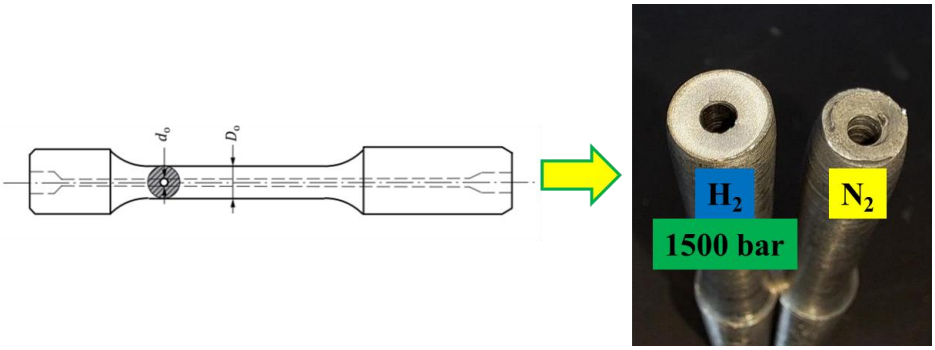

(c)

Figure 16-*Sketches from the standards and pictures of SSRT specimens.* (a) *smooth;* (b) *notched;* (c) *hollow.*

The strain rate applied to the specimen is a fundamental parameter for the successful execution of the test. Since the phenomenon is governed by diffusive processes, the amount of H that can reach the highly stressed regions during the test is closely dependent on the time available. By reducing the strain rate, the material is deformed more slowly, which allows H to be absorbed, diffuse, and accumulate more effectively in the plastic zone ahead of the crack front. The reduction of area becomes much more pronounced as the strain rate drops below approximately 10^{-4} s^{-1}, a value beyond which the material's sensitivity to H increases rapidly. The typical behavior is a strong reduction in ductility as the strain rate decreases, until a very low range is reached, on the order of 10^{-5}–10^{-6} s^{-1}. In this region, the mechanical degradation tends to level off: further reductions in strain rate do not

lead to a significant additional loss of mechanical properties. The origin of this plateau is analogous to that observed in pressure variations: once H has had sufficient time to saturate the reversible trapping sites and the plastically deformed zones, the mechanical response is no longer limited by the rate at which deformation is applied, but by the internal damage mechanisms of the material (Figure 17).

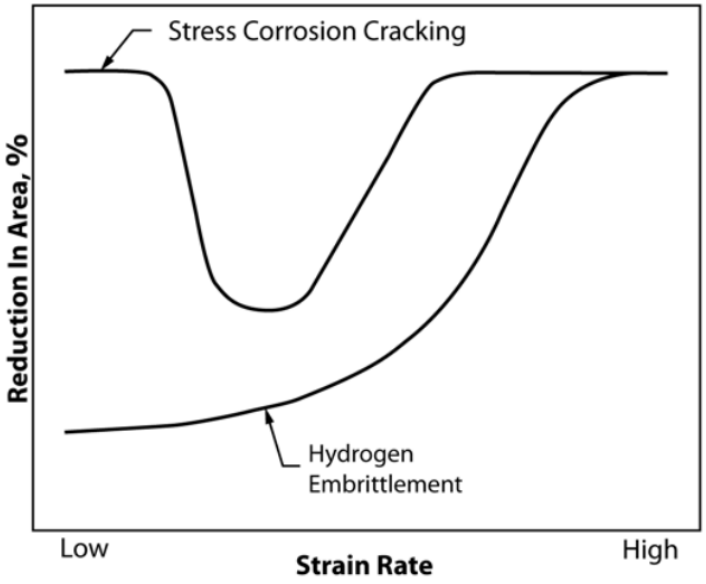

Figure 17-*Effect of test speed in H environment on reduction of area*

Unlike smooth specimens, in which embrittlement manifests itself mainly through changes in elongation and reduction of area, in notched specimens the reference parameter becomes the notched tensile strength (NTS), that is, the maximum load the sample can sustain at the notch. Moreover, the notch makes it possible to isolate the region of interest with respect to the rest of the material; for example, it is particularly useful for testing a weld while excluding the BM.

Hollow specimens have the major advantage of not requiring an autoclave for performing the test, since H flows directly inside them. The setup is therefore much simpler and also allows the specimen to be conditioned externally (for example, to investigate the effect of temperature). However, they also have drawbacks: the geometry itself only allows SSRT tests, excluding fracture-mechanics investigations. The internal machining of the hole is complex (electrical discharge machining is often required, and the achievement of the specified roughness is difficult) and is not compatible with all materials. In this case as well, the results are expressed as variation of the RRA.

Fracture mechanics tests are designed to analyze how an existing crack affects the response of the component and how capable it is of resisting crack propagation. Since defects, notches, and microcracks are unavoidable in real components, these tests represent an essential tool for predicting

the risk of sudden failures. The key output of these tests is fracture toughness, defined as the ability of the material to resist the initiation and unstable propagation of a crack. It provides a quantitative measure of resistance to brittle fracture and makes it possible to establish the maximum level of stress that a component can withstand. The tests typically performed can be divided into static and cyclic. Static tests consist in determining the maximum load associated with failure of the specimen containing a defect or the load required to induce stable defect growth (J_{IH} and K_{IH}). Cyclic tests, instead, are aimed at characterizing fatigue crack growth (FCGR). The objective is to measure the crack growth rate da/dN as a function of the stress-intensity range ΔK, the parameter that controls the level of cyclic loading at the crack tip [197]. The most commonly used specimen types are: compact tension (CT), single edge notch bend (SENB), single edge notch tension (SENT), and bolt-loaded CT (Figure 18). For all specimen types: B is the thickness, H the height, W the width, and a the crack length. The specimens are machined (typically by wire electrical discharge machining, EDM) to obtain a notch where the crack will be initiated and, in the case of J_{IH} tests, any knife edges where the extensometer measuring the crack-mouth opening displacement (CMOD) will be placed during the test. Subsequently, a fatigue pre-crack is grown in the notch so that $0.45 \leq a/W \leq 0.70$. J_{IH} tests allow obtaining Force–CMOD curves (Figure 19a), which are processed according to standards to obtain J–R curves that describe the evolution of J with crack extension Δa. At this point, it is possible to construct the blunting line, which represents the increase in toughness due solely to plastic blunting of the crack tip. It has the following equation (Eq. 36):

$$J = M\sigma_Y \Delta a \qquad \text{Eq. 36}$$

Where M is the slope coefficient specified in the standard, and σ_γ is the flow strength of the material (the average between the yield strength and the ultimate tensile strength). The blunting line therefore provides the theoretical response of the material during the initial stage of crack propagation, before stable crack growth becomes dominant. Subsequently, the experimental J–R curve is fitted using a power law and compared with this line to obtain the characteristic parameters of fracture resistance. By shifting the blunting line by 0.2 mm along the x-axis, the offset line is obtained. The intersection of the latter with the J–R curve indicates the value of J_{IH} (Figure 19b).

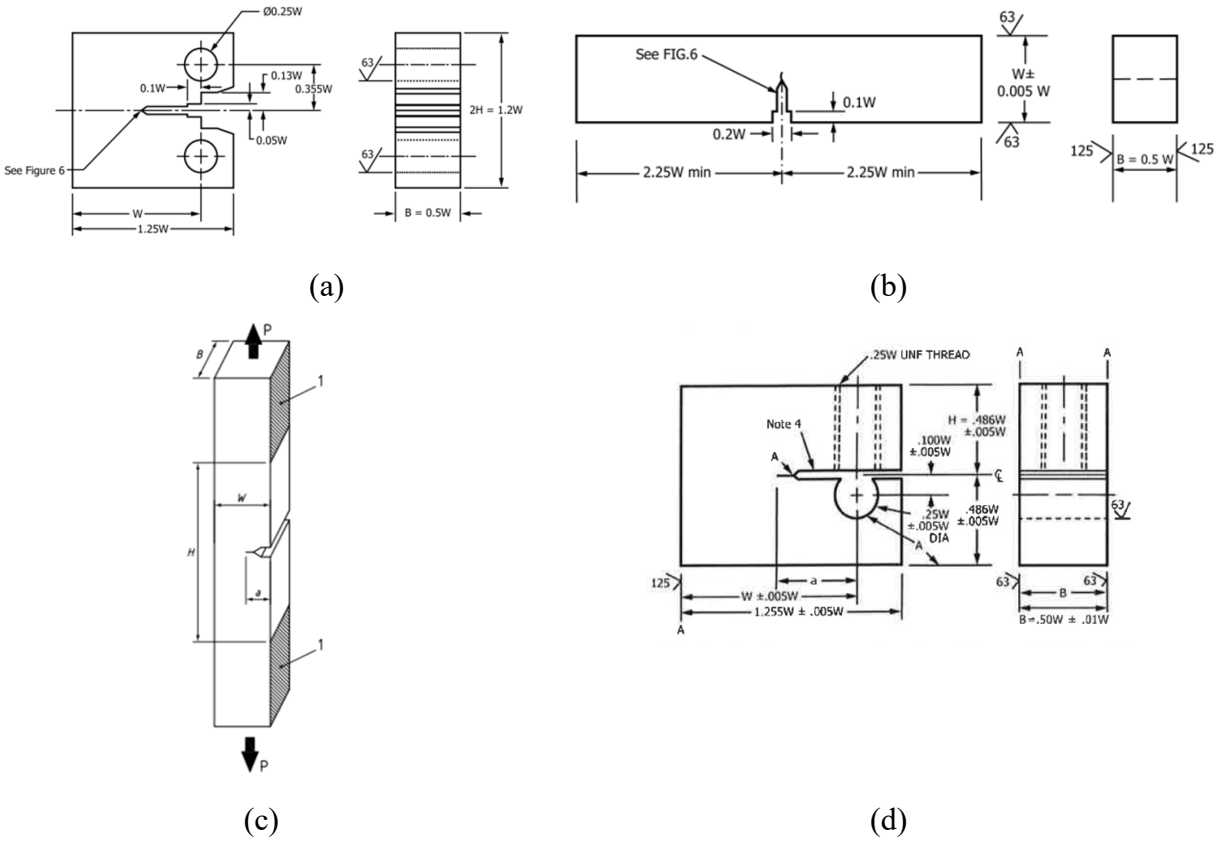

Figure 18-*Sketches of the main specimens used for fracture mechanics testing.* (a) *CT [191]*; (b) *SENB [191]*; (c) *SENT [198]*; (d) *bolt loaded CT [186]*.

Constant-displacement tests for determining K_{IH} require the use of a glovebox with direct access to an autoclave. After the pre-cracking step, the specimens are placed inside the glovebox. The hole they are equipped with allows inserting and tightening a bolt in order to apply a specific load to the crack and enable its growth. Immediately afterward, they are loaded into the autoclave, where H_2 gas is introduced at the pressure and for the duration required by the test. Once the test is completed, the specimen is extracted from the vessel and then heat tinted. Finally the fracture surface is opened in liquid nitrogen (LN_2). This procedure, allows to distinguish the pre-crack, the stable crack growth and the final brittle fracture.

The impact of H on the fracture toughness of pipeline steels depends critically on the microstructure and the level of mechanical strength. It has been widely observed that microstructures containing martensite–austenite exhibit the highest susceptibility to toughness reduction in the presence of H, followed by mixed bainite–pearlite microstructures and finally pearlite [199]. The presence of inclusions is also crucial: they act as preferential fracture-initiation sites and significantly reduce toughness. In X80 steel, Mn–Ti–Si–rich inclusions caused a 35% reduction in J under H charging, an effect even greater than that of pre-existing welding cracks [200].

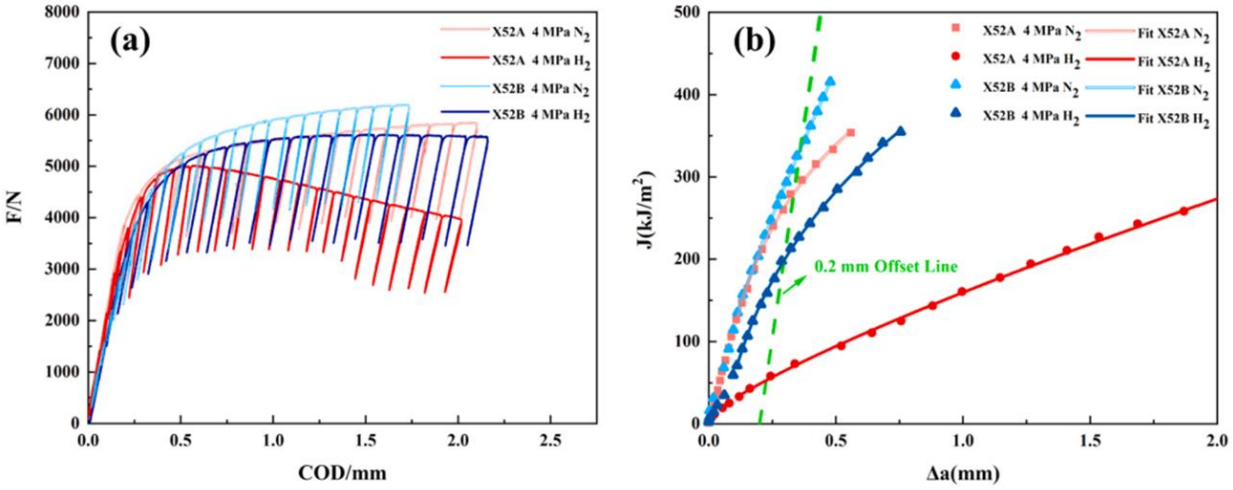

Figure 19-(a) *P vs CMOD curves and* (b) *resulting J-R curves with the blunting and offset line [201].*

Several studies have reported that the BM offers higher fracture toughness than the weld metal (WM) in H environment. Welding modifies the microstructure by increasing the grain boundary density and the fraction of high-angle grain boundaries [202] [203] [204] [205]. However, under certain conditions, the WM can exhibit greater resistance to H-assisted fracture due to the presence of a acicular microstructure, which can act as an effective irreversible trap for H. In this case, H is trapped away from the crack tip, reducing the critical concentration needed to activate decohesion mechanisms [206]. An increase in the yield strength of steels generally leads to greater susceptibility to degradation of fracture toughness in H environment. The main reason lies in the typical microstructure of high-strength steels, characterized by a higher density of crystalline defects that serve as H trapping sites. These sites promote localized H accumulation, increasing the likelihood of activating HEDE (Hydrogen-Enhanced Decohesion) or HELP (Hydrogen-Enhanced Localized Plasticity) mechanisms. In steels with high yield strength, the intrinsic resistance to plastic deformation is greater, meaning that even small H accumulations are sufficient to drastically reduce the microstructure's ability to shield the crack tip through plasticization [207] (Figure 20). The increase of H pressure, according to Eq. 18, increases the amount of H atoms that can dissolve in the metal lattice and thus concentrate at the crack tip. This phenomenon leads to a progressive reduction of fracture toughness, which is evident even at very low pressures and typically becomes more pronounced as pressure increases.

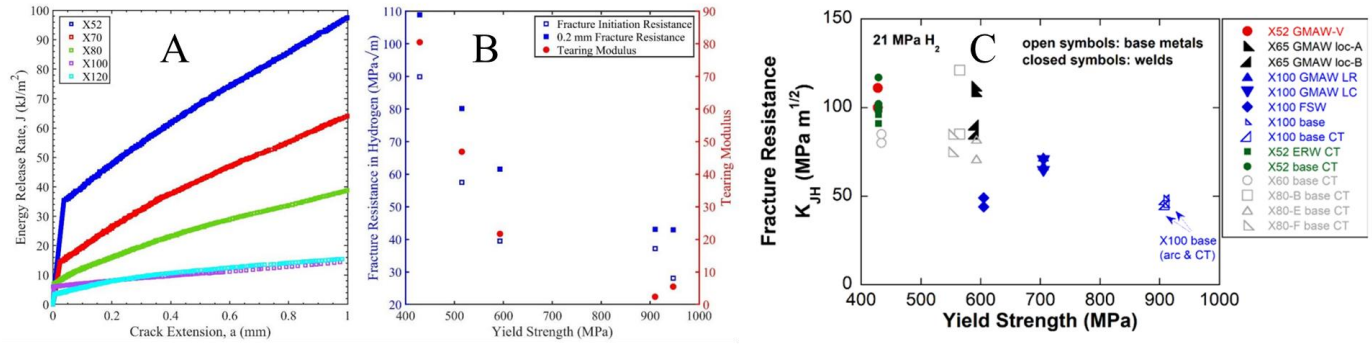

Figure 20-*Effect of increasing yield strength on fracture toughness in H.* (a) *and* (b) *Tests conducted at 200 bar of* H_2, (c) *test conducted at 210 bar of* H_2. *As the steel grade increases, there is a rapid drop in fracture toughness [208].*

A comprehensive study conducted on a range of pipeline steels from different eras and strength classes concluded that the decrease in fracture toughness begins at pressures as low as approximately 0.2 bar, with a significant reduction up to about 20 bar, beyond which embrittlement tends to stabilize, showing only marginal variations up to 100 bar [209]. Another important study on a wide range of pipeline steels demonstrates a clear dependence of fracture toughness on H pressure, with a progressive reduction up to pressures between 100 and 300 bar, beyond which a plateau is reached [210]. Similarly, in cathodic environments, as the current density applied during electrochemical charging increases, fracture toughness systematically decreases. This effect is attributed to the increased concentration of diffusible H, which is more effective in reaching the plastic zone at the crack tip and promoting embrittlement mechanisms [18].

The assessment of fatigue crack growth plays a fundamental role in the safe design of pipelines. Fatigue crack propagation is described by the Paris-Erdogan law [211], which correlates the crack growth rate, da/dN, with the stress intensity factor range, ΔK (Eq. 37):

$$\frac{da}{dN} = C(\Delta K)^m \qquad \text{Eq. 37}$$

Where C and m are material-dependent constants.

Although parameters such as load ratio and cycle frequency can influence the propagation kinetics, most metals exhibit behavior consistent with the typical pattern shown in Figure 21.

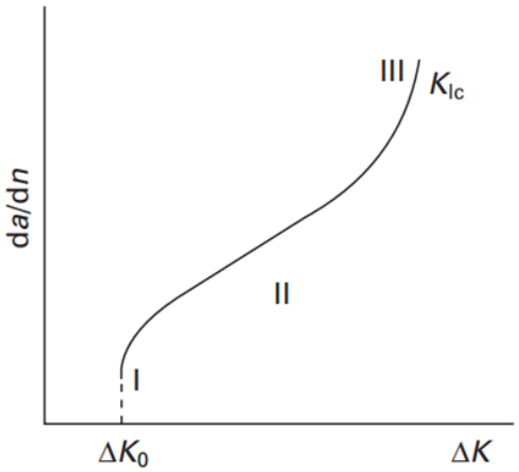

Figure 21-*Typical Paris-Erdogan curve.*

Below a certain threshold of ΔK, the crack does not advance in measurable way. In Stage I, growth increments are extremely small, on the order of 10^{-7} mm, and strongly dependent on the material's microstructure. Stage II begins when the crack reaches a size large enough to generate a plastic zone affecting multiple grains, making the phenomenon progressively less sensitive to local microstructural features. Finally, in Stage III, the stress intensity factor approaches the critical fracture toughness value, K_{IC}, causing a rapid increase in crack growth rate until final failure, no longer described by Eq. 37. During the test, the load is applied according to an opening and closing cycle on the CT specimen, characterized by a defined load ratio, while crack growth is continuously monitored by an extensometer. The presence of H is known to accelerate fatigue crack growth. It is therefore essential to understand how this acceleration depends on parameters such as pressure, load ratio, and loading conditions, in order to accurately assess the fatigue performance of pipelines intended for H transport. In FCGR tests, it is difficult to isolate the contributions of individual parameters. For example, regarding H pressure, the results are not univocal. In general, an increase in H partial pressure increases FCGR [212]. However, experimental results do not show a consistent behavior: depending on the test conditions, pressure increase may cause a marked, moderate, or even negligible increase in FCGR. This variability is attributed to the fact that pressure does not act in isolation but interacts with parameters such as frequency and load ratio (R) [187]. Very low pressures, on the order of 0.2 bar, can already cause a significant increase in FCGR, in some cases up to an order of magnitude compared to air [213]. However, as pressure increases, the FCGR increase does not continue indefinitely: several studies report a saturation behavior, typically between 50 and 100 bar, beyond which further pressure increases do not cause appreciable increases in crack growth rate [214] [215] [216].

Generally, an increase in FCGR is observed as the loading frequency decreases [217]. This behavior is typical of diffusion-controlled mechanisms: lower frequencies allow more time for H transport to the crack tip, amplifying HE effects. Increases of up to 5 times in FCGR have been observed when frequency decreased from 1 to 0.001 Hz [218], but also a very limited effect at high pressures, suggesting a H saturation regime at the crack tip [214].

1.8 Previous activities

As anticipated in the introduction, this thesis is part of a broader project started in 2022 at Istituto Italiano della Saldatura-Ente Morale, aimed at studying the fitness for service in H for NG pipelines [219] [220]. In particular, potentiostatic charging studies and SSRT tests with in-situ cathodic charging were performed to analyze the HE phenomenon in a vintage API 5L X52 pipeline steel (see Chapter 2 for the characterization) [221]. The effects of electrolyte concentration, applied potential, and recombination poison were systematically analyzed and correlated with H uptake of about 1 ppm. This value represents the critical threshold beyond which HE manifests in HSLA steels and corresponds to a H pressure of about 300 bar, considered the maximum tolerable limit for gas pipelines [132] [222]. Polished specimens were used as the working electrode, together with a platinum mesh as the counter electrode and a standard Ag/AgCl electrode as the reference. For the preliminary experiments, a potential of −900 mV was selected to limit the formation of corrosion films on the specimen surface, which could hinder H uptake [122] [123] [223]. To assess the effect of potential, tests were also performed at −750 mV and −650 mV. Each potential was tested in H_2SO_4 solutions of different concentrations (1 M, 0.5 M, 0.1 M, and 0.01 M), and H uptake was measured for charging times of 600, 900, 1800, and 3600 s. To promote H charging in the acidic environment, TU was added as a recombination inhibitor. Several studies have shown that a TU concentration of 2 g/L does not interfere with the results, even in strongly acidic solutions or at highly cathodic potentials [133] [140]. It has also been observed that concentrations above this value can favor the formation of corrosion products on the surface, hindering H absorption and thus requiring more cathodic potentials [224]. For these reasons, TU was kept constant at 2 g/L in all solutions, in order to minimize the number of experimental variables and ensure its recombination-inhibiting effect. The results shown in Fig. 22a indicate that for a charging time of 3600 s, the H concentration in the steel increases both with increasing acid concentration and with more cathodic potentials. This is attributed to the higher activity of H^+ ions in the electrolyte and the more intense cathodic reduction. The effect of acid concentration is particularly pronounced at −900 mV, where the absorption trend follows a power-law behavior. At −750 mV, the increase corresponds to a moderate exponential trend, while at −650 mV it is almost linear. For this reason, at equal acid concentration, the H content obtained at −900

mV is typically twice that obtained at −750 mV and about five times higher than that obtained at −650 mV, with less significant differences in the more diluted solutions. Figures 22b, 22c, and 22d illustrate the time evolution of H uptake for three acid concentrations (0.01 M, 0.1 M, 1 M).

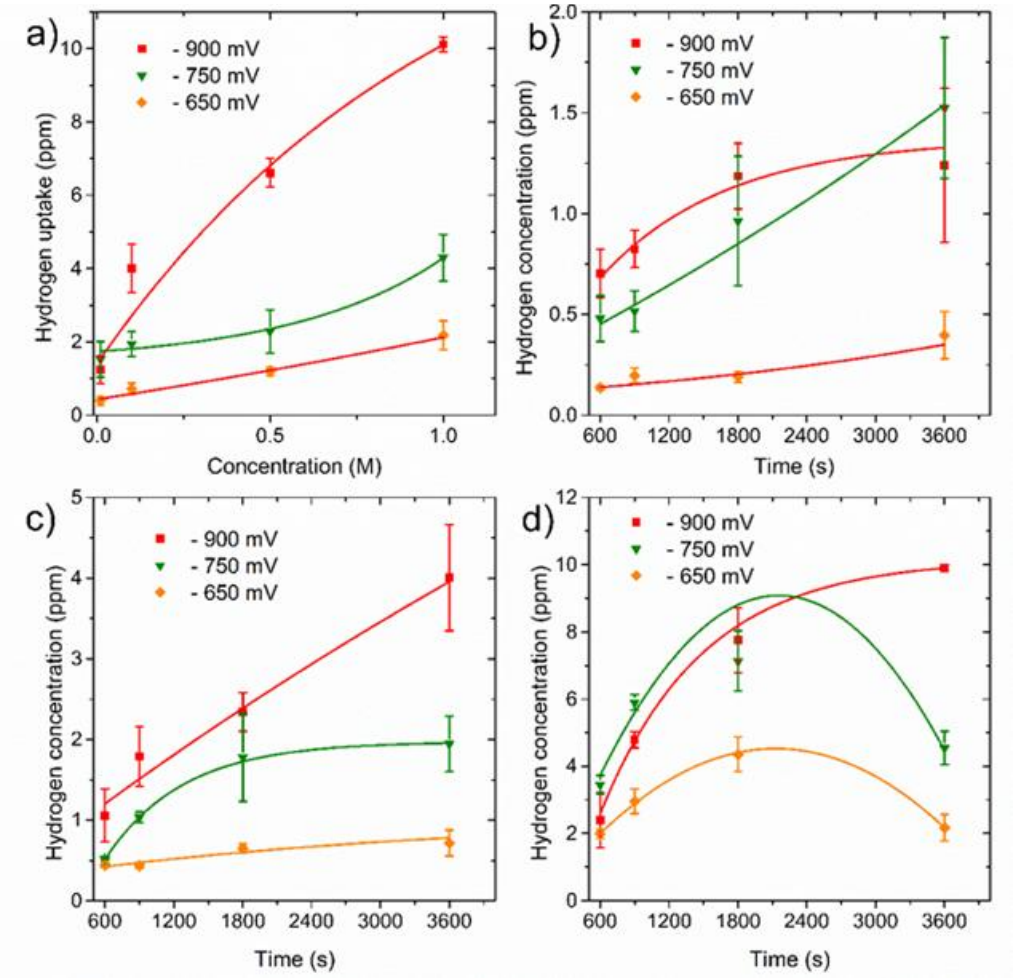

Figure 22-*H uptake as a function of acid concentration after 3600 s* (a) *and as a function of time for an acid concentration of (b) 0,01 M, (c) 0,1 M e (d) 1 M.*

Under all conditions, a more cathodic potential leads to greater H uptake. In the most diluted solutions (0.01 M), absorption at −750 mV and −650 mV shows an essentially linear trend. As the acid concentration increases, however, the behavior changes, with an initial rise followed by a decrease caused by H recombination phenomena. In contrast, at −900 mV the trend becomes more linear as the acid concentration increases, indicating a more efficient transfer of H from the surface into the metal. Post-charging analysis revealed that most experimental conditions resulted in the formation of surface blisters, whose size was proportional to the applied potential and the solution concentration (up to a maximum of 0.5 mm). The phenomenon occurs in all tests performed in 1 M and 0.1 M solutions. In the 0.01 M solution, blister formation disappears only at the least severe potentials, namely −750 mV and −650 mV. The average H contents under these conditions are 1.50 ppm and

0.40 ppm, respectively. Since 1.50 ppm is the closest value above the critical threshold of 1 ppm required for a full manifestation of HE phenomena, −750 mV was selected as the optimal charging condition, free from surface damage. For comparison, the use of deionized water results in only 0.001–0.003 ppm, confirming that it does not significantly contribute to H uptake. The preparation of the SSRT specimens was carried out in accordance with ASTM E8/E8M [225], machining the samples along the axial direction of the pipe. The SSRT tests were conducted following ASTM G129–5, with the aim of identifying the correct displacement ratio for detecting the effect of H on the embrittlement index (EI). The strain-rate window indicated by the standard (10^{-4}–10^{-8} s^{-1}) was explored by analyzing the reduction in area (Z). The results (Fig. 23) show that Z increases with increasing strain rate and tends to stabilize for $\dot{\varepsilon} < 10^{-5}$ s^{-1}. Therefore, a strain rate of 10^{-5} s^{-1} (0.05 mm/min) was selected as the optimal condition for the SSRT tests.

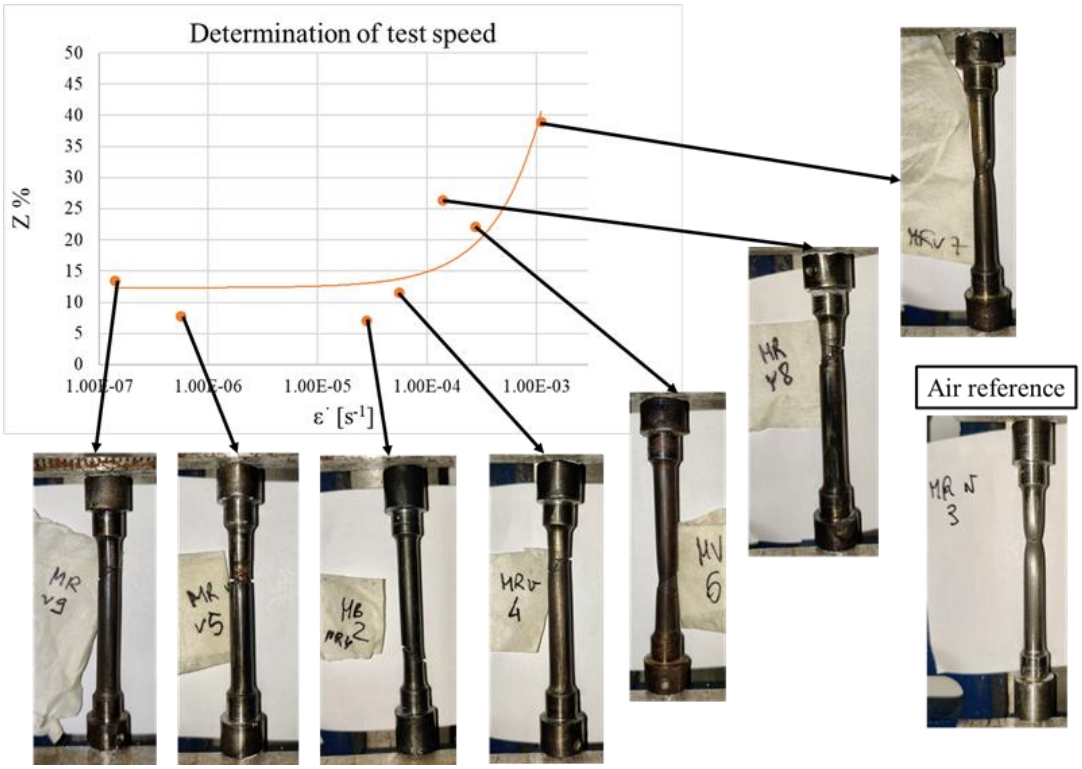

Figure 23-*Determination of the test speed according to ASTM G129.*

The tests were carried out on BM specimens and specimens containing the girth weld (W). H uptake remained consistent between the two groups: approximately 1.21 ppm for the W specimens and 1.10 ppm for the BM specimens. The stress–strain curves in air show significant differences between BM and W (Fig. 24). The W specimens exhibit a typical mild-steel behavior, with yield-point fluctuations caused by Cottrell atmospheres. In contrast, the BM specimens, being more homogeneous, display a distinct yield point that can be identified by the $R_{0.2}$ value.

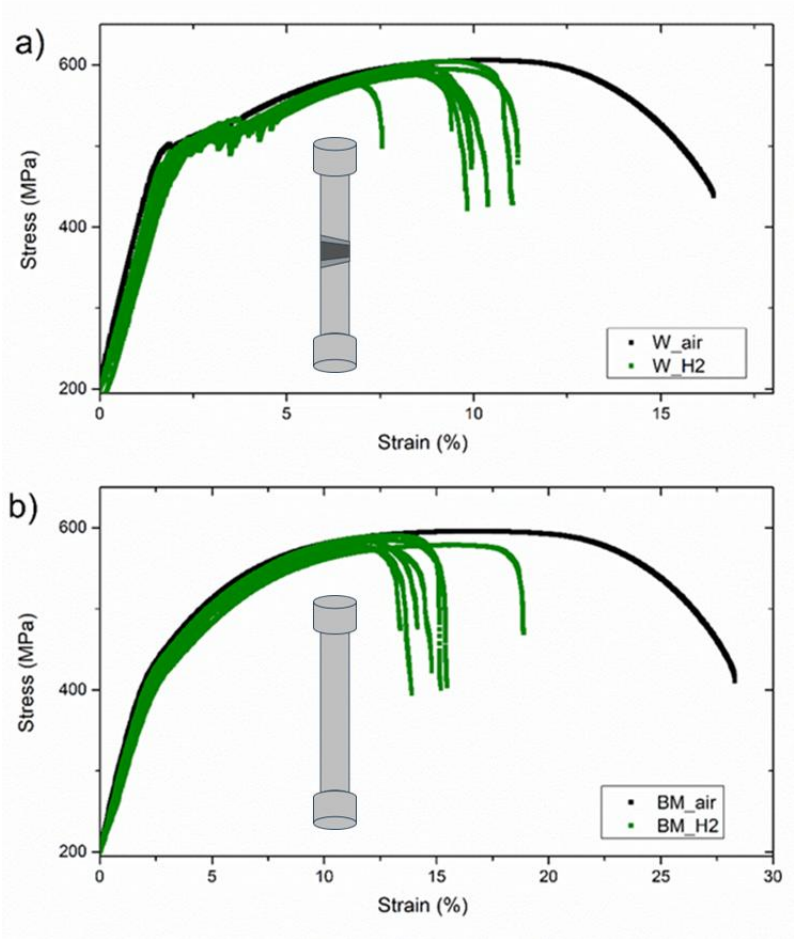

Figure 24-*Stress–strain curves from in-situ SSRT tests conducted in air and under electrolytic charging for W* (a) *and BM* (b) *specimens.*

Since fracture in the W specimens consistently occurs within the BM region, this area was identified as the most vulnerable to HE. H causes a pronounced decrease in the percentage elongation (ε%), dropping from approximately 15% to about 10% in the BM and W specimens, respectively. In both cases, a significant loss of ductility is observed. Similarly, the reduction of area Z decreases sharply from about 70% (tests in air) to less than 20% (tests under electrolytic charging). These values confirm a marked embrittlement effect (Figure 25 a–d). Metallographic observations show that the electrolytically charged specimens exhibit a fracture characterized by a peripheral brittle layer with a thickness of 200–500 μm, followed by a transition zone and a ductile core. In the tests performed in air, the fracture is entirely ductile, with extensive plastic deformation and microvoid formation (Figure 25 e–g).

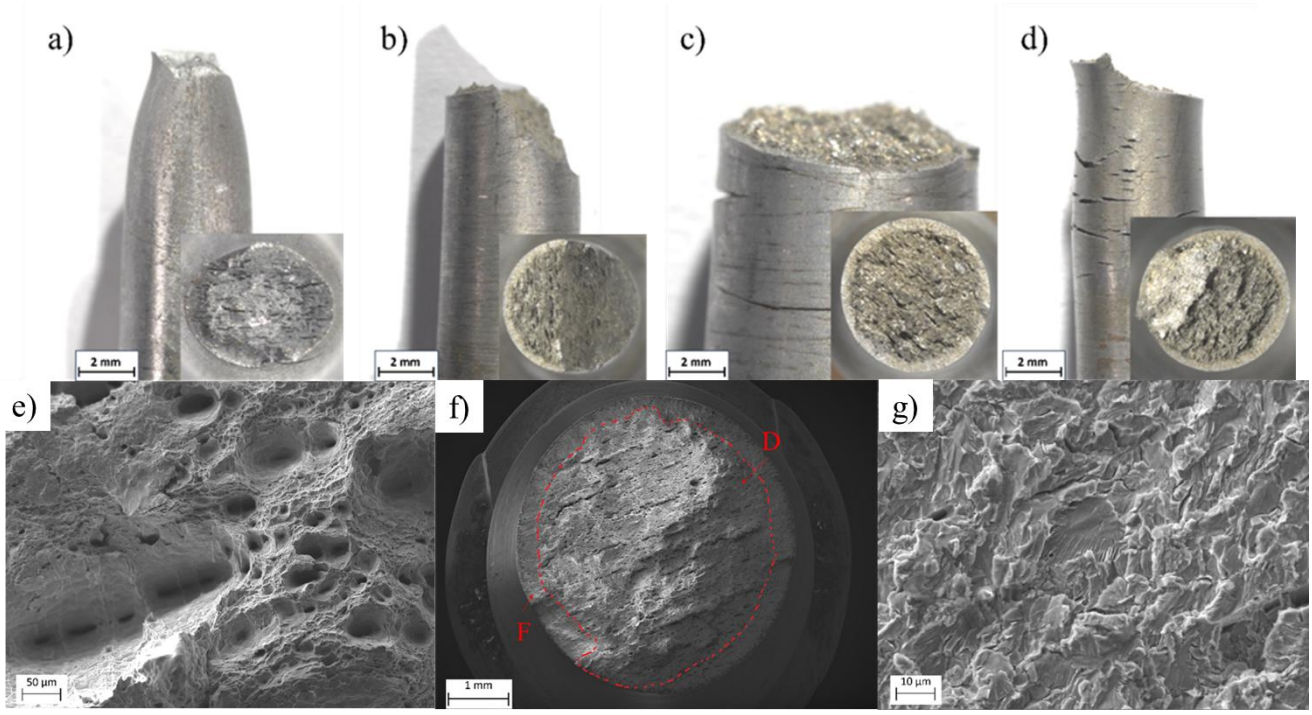

Figure 25-*Fracture propagation and fracture surface for specimens tested in air* (a) *and specimens in situ charged* (b–d). *For all samples, fracture occurred in the BM. SEM images of the fracture surface that developed in the BM of a charged specimen* (f) *reveal a markedly ductile (D) and brittle (F) fracture morphology. Magnified views of the ductile and brittle fracture modes are shown in* (e) *and* (g), *respectively.*

The micrographs in Fig. 26a–b show longitudinal sections of specimens tested under electrolytic charging and in air. In the charged sample, the peripheral region exhibits a distinctly brittle fracture, with flattened surfaces and minimal plastic deformation, whereas the specimen tested in air retains a fully ductile behavior, characterized by continuous granular deformation along the fracture path. In the H-charged samples, the brittle fracture abruptly terminates beyond a certain depth, producing a brittle–ductile transition zone consistent with the H concentration gradient, which is highest at the surface and progressively decreases toward the core of the material. The longitudinal sections also reveal the presence of secondary cracks originating from the surface and propagating transversely to the loading direction and to the rolling direction, eventually intersecting metallurgical inclusions (Fig. 26c). These inclusions may act either as preferential propagation paths or as nucleation sites for new cracks (Fig. 26d), which develop from the tips of the inclusions with a transverse orientation. The high-resolution image (inset in Fig. 26d) confirms this behavior, clearly showing the crack front and the combined influence of H, matrix, and inclusions on its evolution.

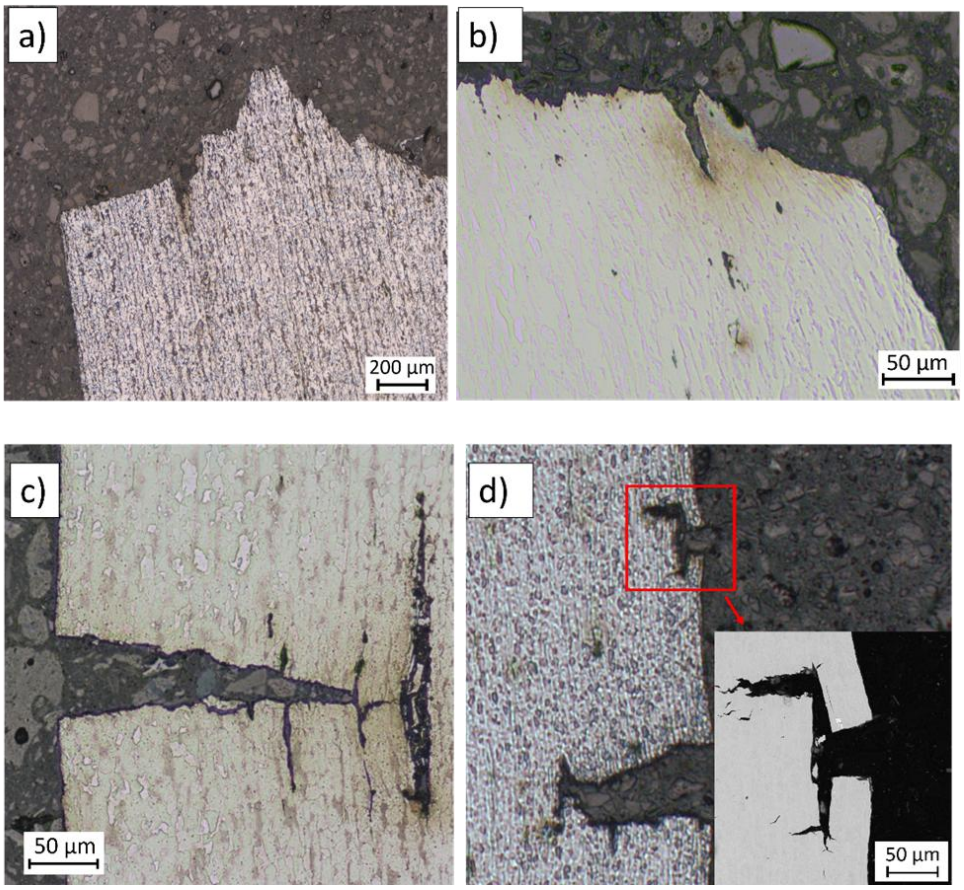

Figure 26-*Longitudinal micrographs of specimens tested under electrochemical charging* (a, c, d) *and in air* (b). *Interaction between secondary cracks and inclusions* (c–d). *Detail of a crack in* (d) *shown after SEM analysis.*

2 Materials and Methods

2.1 API 5L X52 Line Pipe Steel

The study focuses on a API 5L X52 steel natural gas pipeline that has been in service in Italy since the 1970s. (Fig. 27a). The pipeline has an outer diameter of 660 mm and a wall thickness of 12.7 mm. The pipeline features two welds (Fig. 27b): a longitudinal weld produced by the submerged arc welding (SAW) process and a circumferential weld made using the shielded metal arc welding (SMAW) process. The longitudinal weld was carried out with two passes (Fig. 27c), whereas the girth weld was performed with four passes (Fig. 27d). Although the intermediate filler passes are not clearly visible, their presence can be inferred from the profile of the heat affected zone (HAZ) of the entire weld bead. The HAZ exhibits a cup-shaped morphology, open toward the outer surface and narrower on the inner side at the location of the first full-penetration pass. Moving outward, the HAZ widens up to approximately one quarter of the joint thickness, allowing the second filler pass to be identified; this then merges with the capping pass. The latter is clearly recognizable due to the darker tempering zone that crosses the center of the joint. In this study, attention was focused on the

circumferential weld, as it is considered more critical than the longitudinal one. The latter was produced in a controlled environment using the SAW process, which is characterized by higher quality standards, whereas the circumferential weld was executed on site during pipeline installation, making it more exposed to operational and environmental variability.

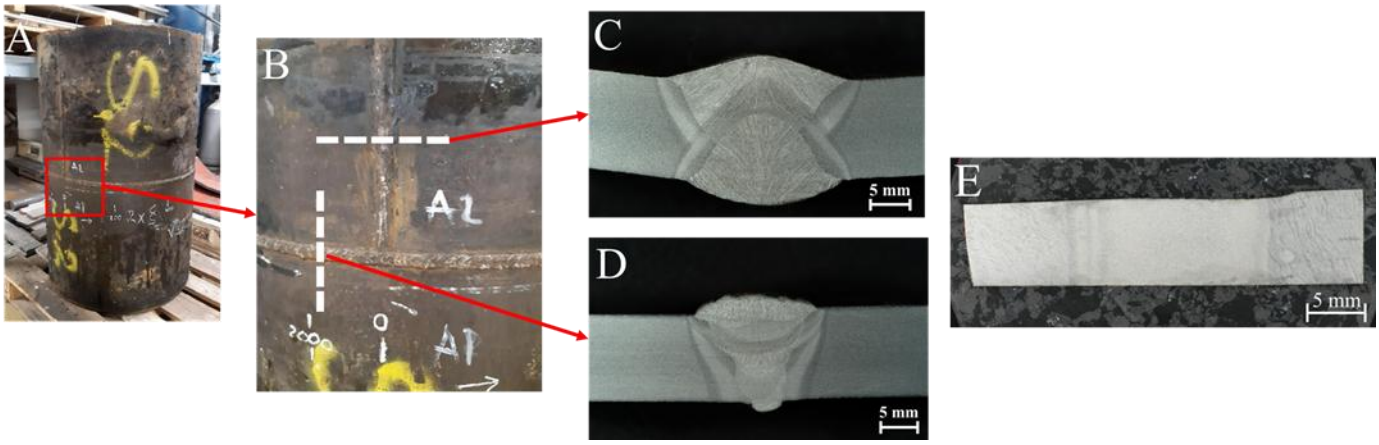

Figure 27-(a) *Pipe studied in this thesis;* (b) *enlargement of the two weld beads; macrograph of the longitudinal weld* (c), *girth weld front view* (d), (e) *girth top view.*

The chemical compositions of the BM and the FZ were analyzed using an ARL 3460 optical emission spectrometer, yielding the results reported in Table 8. The BM was subjected to tensile testing at room temperature. The BM, HAZ, and FZ were tested by Charpy V-notch impact tests using full-size specimens of 10 × 10 × 55 mm³ at 0 °C, and by Vickers hardness testing (HV10) at room temperature. The obtained results are consistent with the API 5L standard [35].

Table 8-*BM and FZ chemical composition (Fe balance).*

Base material composition										
Element	**C**	**Mn**	**P**	**S**	**Si**	**Cr**	**Ni**	**Nb**	**Mo**	**Ti**
wt%	0.250	1,360	0.011	0.019	0.270	0.023	0.027	0.030	0.004	0.006
Weld metal composition										
Element	**C**	**Mn**	**P**	**S**	**Si**	**Cr**	**Ni**	**Nb**	**Mo**	**Ti**
wt%	0.140	0.670	0.011	0.015	0.240	0.020	0.016	0.003	0.428	0.013

Table 9-*Tensile properties of BM tested in air at room temperature.*

Elastic modulus [GPa]	**$R_{p0,2}$ [MPa]**	**$R_{t0,5}$ [MPa]**	**R_m [MPa]**	**Rupture elongation [%]**
207	430	441	605	29

Table 10-*Charpy-V impact test and Vickers HV10 test results.*

Materials	Asorbed Energy [J]	Hardness HV10
BM	121	199
HAZ	116	206
FZ	50	221

For metallographic analysis, portions of the weld bead were mounted in resin and subsequently polished using silicon carbide (SiC) abrasive papers with grit sizes ranging from P500 to P1000, followed by polishing with diamond pastes from 3 to ¼ μm. The samples were then etched with Nital 1% (99 wt.% ethanol and 1 wt.% nitric acid) and examined using a Zeiss Axio Imager Z2 metallographic optical microscope (LOM) and a Zeiss EVO 15 scanning electron microscope (SEM). The microstructure of the BM (Fig. 28a–b) shows the typical ferrite grains elongated by the rolling process. The secondary phase consists of pearlite and, predominantly, very fine carbides, likely formed during the hot roll-forming process to which the plate was subjected. The HAZ exhibits a Widmanstätten-type microstructure, composed of ferrite and bainite with rare pearlite islands (Fig. 28c–d). The different welding passes impart a heterogeneous microstructure to the FZ: the lower region, tempered by the subsequent passes, shows a ferrite/pearlite configuration (Fig. 28f), whereas the surface region is characterized by the presence of acicular structures (Fig. 28e). The characterization of the circumferential weld bead also revealed the presence of numerous elongated inclusions in the BM (Fig. 29a) and globular inclusions in the FZ (Fig. 29b). The appearance of inclusions in the BM was compared with the reference images of the UNI 3244 [226] standard. SEM–EDXS analyses confirmed the presence of oxides, sulfides, and silicates.

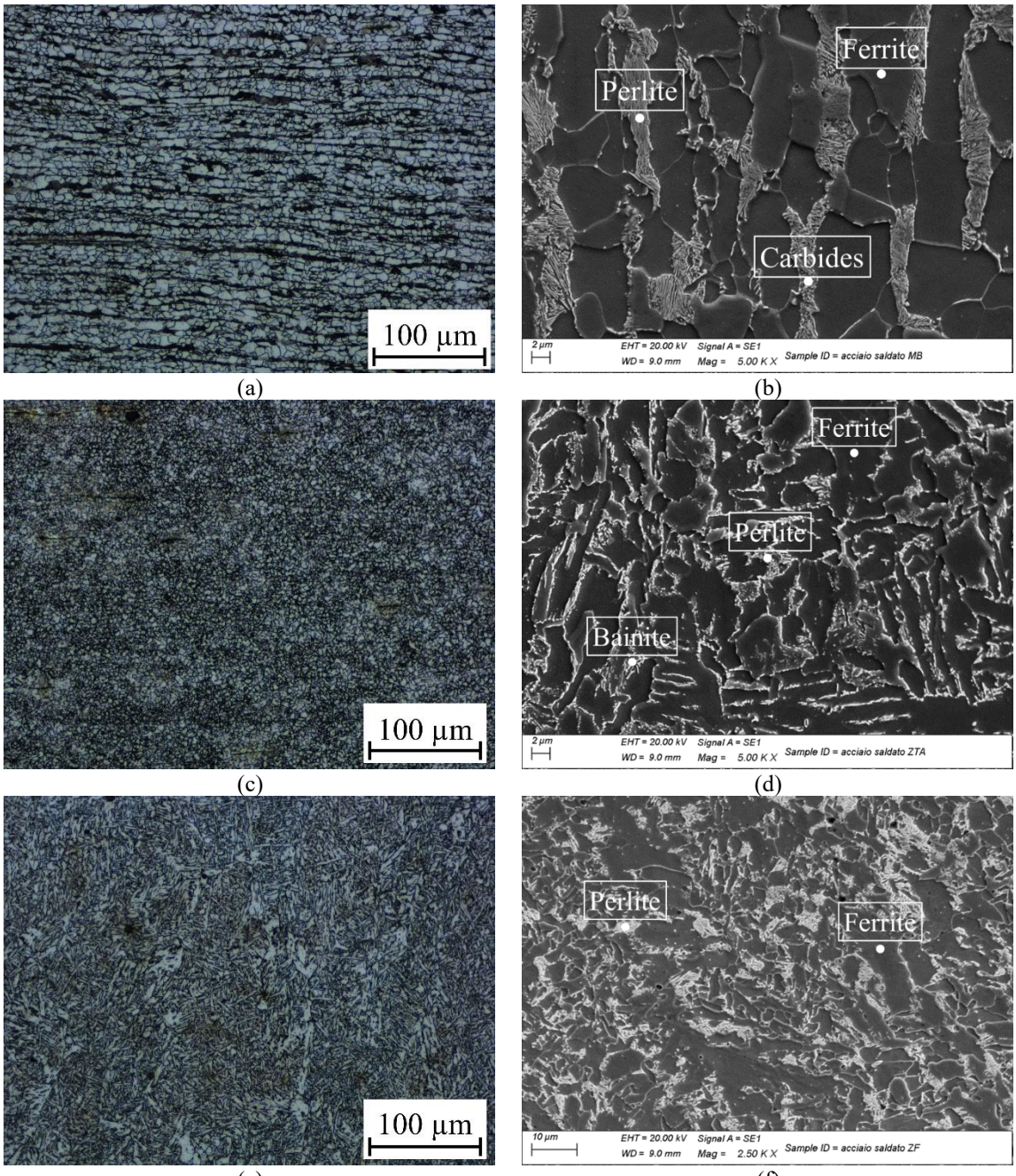

Figure 28-*Weld bead micrographs:* (a) *BM LOM 200X;* (b) *BM SEM 5000X;* (c) *HAZ LOM 200X;* (d) *HAZ SEM 5000X;* (e) *FZ LOM 200X;* (f) *FZ SEM 2500X.*

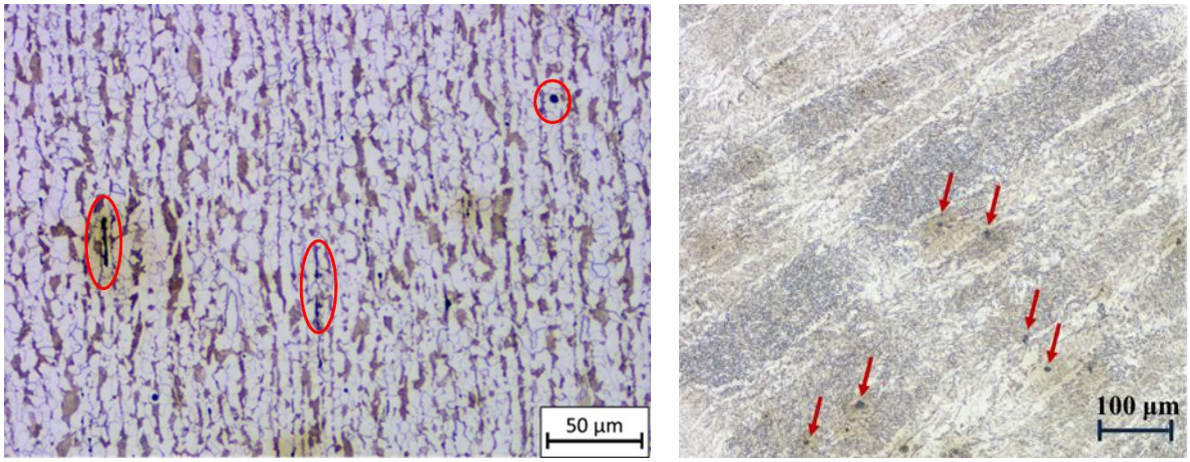

(a) (b)

Figure 29-(a) *Inclusions in the BM;* (b) *globular inclusions in the FZ.*

2.2 Experimental standards

In this work, fracture mechanics tests and permeation tests were performed. The standards followed for the correct conduct of the experimental campaign will be described in detail below. Only those parts of the standards actually used in this work will be described.

2.2.1 ASTM E1820 and ISO 12135 standards

The ASTM E1820 standard represents the primary normative reference for the determination of fracture toughness of metallic materials under elastic–plastic conditions. It defines the experimental procedures, specimen requirements, and validity criteria for the measurement of fundamental parameters such as K, the J-integral, and the crack growth resistance curve (J–R curve). The following specimen parameters must be known: width (W), thickness (B), height (H), net thickness (B_N, equal to B in the absence of side grooves), initial crack length including the notch and fatigue pre-crack (a_0), final crack lenght (a_p), ligament ($b = W - a$), and span, i.e., the distance between the support points in three-point bending tests ($S = 4W$). Among the recommended testing methods, the compliance method was selected because it allows a complete J–R curve to be obtained using a single specimen (Section A1 for SENB specimens). A clip-on extensometer is placed in the knife-edge notches machined on the specimen to monitor the crack mouth opening displacement (CMOD). An increasing load is applied to the specimen, interrupted by unloading cycles, in order to obtain an F vs. CMOD curve such as that shown in Fig. 19a. The inverse of the slopes of the unloading segments corresponds to the compliance (C) values. At this point, the standard follows two parallel paths: one for calculating the crack length and the other for calculating the J-integral. The first step is the heat tinting of the specimen in an oven at 300 °C for 30 minutes. Afterward, the specimen is broken in

LN_2. Subsequently, nine equally spaced measurements of a_0 and a_p, are taken along the crack front. The average value is then calculated according to Eq. 38:

$$a = \frac{1}{8}\left[\left(\frac{a_1+a_9}{2}\right) + \sum_{j=2}^{j=8} a_j\right] \quad \text{Eq. 38}$$

Then the compliance is normalized using Eq. (39):

$$u = \frac{1}{\left[\frac{B_e W E C_i}{S/4}\right]^{1/2}+1} \quad \text{Eq. 39}$$

where $B_e = B - (B - B_N)^2/B$. This allows the influence of specimen dimensions and test system stiffness to be eliminated. The crack length associated with each unloading cycle can now be calculated by solving the polynomial expressed in Eq. (40), substituting the corresponding values of u:

$$\frac{a_i}{W} = 0.999748 - 3.9504u + 2.9821u^2 - 3.21408u^3 + 51.51564u^4 - 113.031u^5 \quad \text{Eq. 40}$$

The crack lengths calculated using Eq. 38 must fit the polynomial. As an alternative to the extensometer, the load line displacement (LLD) method can be used to determine the crack length, as described in Annex E of the UNI ISO 12135 standard. Before performing the actual test, it is necessary to place in the testing machine an unnotched specimen with the same dimensions as the final ones and subject it to a load equivalent to that applied to the other specimens. The resulting curve must be subtracted from that obtained with the notched specimens in order to eliminate the contribution of the testing machine to the measurement. In the case of SENB specimens, the J-integral is given by Eq. (41):

$$J = J_{el} + J_{pl} \quad \text{Eq. 41}$$

where J_{el} and J_{pl} are the elastic and plastic components of the J-integral, respectively. J_{el} is defined by Eq. (42):

$$J_{el} = \frac{(K_i)^2(1-\nu^2)}{E} \quad \text{Eq. 42}$$

where E and ν are the Young's modulus and Poisson's ratio of the material, respectively. K is defined by Eq. (43):

$$K_i = \left[\frac{P_i S}{(BB_N)^{1/2} W^{3/2}}\right] f(a_i/W) \quad \text{Eq. 43}$$

where P is the load associated with the corresponding value of a, and f is a dimensionless geometric function that describes the effect of specimen geometry and crack length on the stress field at the crack tip. It is defined by Eq. (44):

$$f\left(\frac{a_i}{W}\right) = \frac{3\left(\frac{a_i}{W}\right)^{1/2}\left[1.99-\left(\frac{a_i}{W}\right)\left(1-\frac{a_i}{W}\right)\left(2.15-3.93\left(\frac{a_i}{W}\right)+2.7\left(\frac{a_i}{W}\right)^2\right)\right]}{2\left(1+2\frac{a_i}{W}\right)\left(1-\frac{a_i}{W}\right)^{3/2}} \quad \text{Eq. 44}$$

At this point, the calculation of J_{pl} is performed using Eq. (45):

$$J_{pl(i)} = \left[J_{pl(i-1)} + \left(\frac{\eta_{pl(i-1)}}{b_i}\right)\left(\frac{A_{pl(i)}-A_{pl(i-1)}}{B_N}\right)\right] \cdot \left[1 - \gamma_{pl(i-1)}\left(\frac{a_i-a_{i-1}}{b_{i-1}}\right)\right] \quad \text{Eq. 45}$$

where η_{pl} and γ_{pl} are, respectively, the factor that converts the global plastic energy into energy density at the crack tip and the correction factor that accounts for crack growth during the plastic increment. If the LLD method is used, their values are 1.9 and 0.9, respectively; otherwise, they are given by Eq. (46) and Eq. (47):

$$\eta_{pl} = 3.667 - 2.199\left(\frac{a_{(i-1)}}{W}\right) + 0.437\left(\frac{a_{(i-1)}}{W}\right)^2 \quad \text{Eq. 46}$$

$$\gamma_{pl} = 0.131 + 2.131\left(\frac{a_{(i-1)}}{W}\right) - 1.465\left(\frac{a_{(i-1)}}{W}\right)^2 \quad \text{Eq. 47}$$

A_{pl} is the area under the load–displacement curve attributable exclusively to the plastic contribution of the specimen and is given by Eq. (48):

$$A_{pl(i)} = A_{pl(i-1)} + \left[P_{(i)} + P_{(i-1)}\right]\left[v_{pl(i)} - v_{pl(i-1)}\right]/2 \quad \text{Eq. 48}$$

where v_{pl} is the plastic component of the total displacement measured during the test, which can be calculated using Eq. (49):

$$v_{pl} = v_i - (P_i C_i) \quad \text{Eq. 49}$$

Once the J–R curve has been obtained, it is possible to construct the blunting line, i.e., the line that separates the crack-tip blunting region from the onset of crack growth. It is defined by Eq. (50):

$$J = 2\sigma_Y \Delta a \quad \text{Eq. 50}$$

where $\sigma_Y$is the average of the yield strength (σ_{YS}) and the ultimate tensile strength (σ_{TS}) of the material. The blunting line is shifted by $\Delta a = 0.2$mm to obtain the 0.2 mm offset line, which by convention identifies the point at which effective and measurable stable crack propagation begins. The intersection with the J–R curve defines J_{IC}, which, for tests performed in H, is referred to as J_{IH}.

2.2.2 BS 8571 standard

The British Standard BS 8571 provides guidelines for fracture mechanics testing using SENT specimens. Particular attention is given to the schematic representation of the specimen extraction locations in the BM and to the notch orientation in the WM specimens. (Fig. 30).

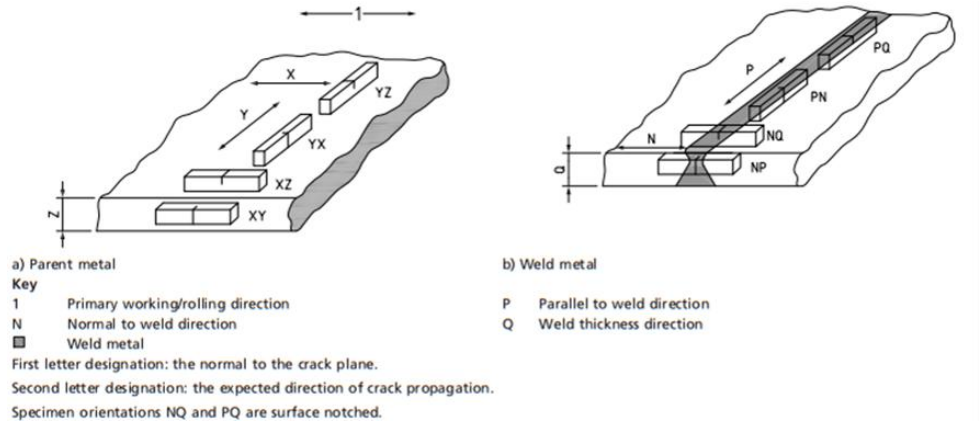

Figure 30-*Crack plane orientation code for fracture toughness specimens of BM and WM.*

The basic method for calculating the J-integral is described below. This method allows the value of J to be estimated at a single point; therefore, it does not make it possible to obtain the entire J–R curve, but only one point on it. The J-integral for clamped SENT specimens is given by Eq. (51):

$$J = J_{el} + J_{pl} = \frac{K^2}{E'} + \frac{\eta_p U_p}{B(W-a_0)} \quad \text{Eq. 51}$$

where U_p is the area of the plastic portion under the F vs. CMOD curve. K is expressed by Eq. (52):

$$K = \frac{P}{(B \cdot B_N)^{0.5} W} \sqrt{\pi a_0} (f_1 - 6\xi_3 f_2) \quad \text{Eq. 52}$$

where f_1, f_2, and $\xi_3$are functions whose values are tabulated.
The compliance method can also be applied to SENT samples following the work of Cravero and Ruggieri [227].

2.2.3 Roberti and Basha's method for calculating fracture toughness

This method, originally proposed by Roberti and Basha, makes it possible to obtain the J–R curve using a single specimen, relying only on the load–displacement curve and on the knowledge of the crack length at the beginning and at the end of the test [228]. For simple test geometries and under conditions where plastic deformation is mainly confined to the remaining ligament, the relationship between the applied load and the load-point displacement can be expressed in normalized form as a function of the crack length and the specimen geometric parameters. In particular, by introducing suitable dimensionless quantities, it is possible to define a so-called *key curve*, which is characteristic of the test geometry and onto which all normalized load–displacement curves collapse as long as the crack remains stationary. During a fracture test with stable crack growth, the experimental load–displacement curve initially follows the key curve up to the onset of crack propagation. Subsequently, due to the progressive reduction of the load-bearing ligament, the specimen response deviates from the theoretical curve corresponding to the stationary-crack case. The first step of the procedure is to normalize the applied load P_i in order to obtain the key curve (Eq. 53).

$$P_i = \frac{PW}{Bb_0^2} \qquad \text{Eq. 53}$$

The methodology proceeds by calculating the final load as if it had been obtained under stationary crack conditions, using Eq. 54:

$$P_{csf} = P_f \frac{b_0^2}{b_f^2} \qquad \text{Eq. 54}$$

Where P_f is the final load, and b_0 and b_f are the initial and final ligament lengths, respectively. From point P_{csf}, a tangent is drawn to the F–CMOD curve, and its equation is then determined. (Figure 31). For all points of the F vs. CMOD curve intercepted by the tangent, the ligament length (and thus the crack length) can be determined using Eq. 55:

$$b_i = b_0 \sqrt{\frac{P_i}{P_{cs}}} \qquad \text{Eq. 55}$$

Where P_{cs} are the solutions of the tangent line for the corresponding CMOD values. The J-integral is then calculated in accordance with the desired standard. The method is compatible with the most common specimen geometries.

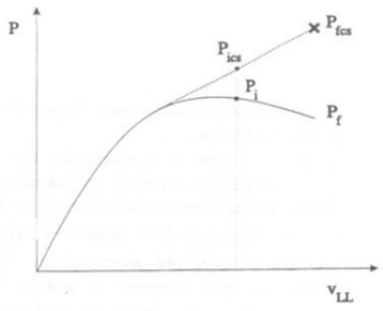

Figure 31-*Diagram of the construction of the key curve*

2.2.4 ASTM G148 standard

The ASTM G148 standard provides a procedure for the evaluation of H absorption, permeation, and transport in metals using the DS cell. To perform a permeation test, the following parameters must be defined: A [cm^2] (exposed area of specimen in the oxidation cell), C_0 [mol/cm^3] (sub-surface concentration of atomic H at the charging side of the specimen), D_{eff} [cm^2/s] (effective diffusivity of atomic H, taking into account the presence of reversible and irreversible trapping), I(t) [μA] (time dependent atomic H permeation current), I_{ss} [μA] (steady-state atomic H permeation current), J(t) [$mol/s\ cm^2$] (time-dependent atomic H permeation fluow as measured on the oxidation side of the specimen), J_{ss} [$mol/s\ cm^2$] (atomic H permeation flow at steady-state), $J(t)/J_{ss}$ (normalized flow of atomic H), L [cm] (specimen thickness), t [s] (time elapsed since the start of H charging), t_{lag} [s] (time to achieve a value of $J(t)/J_{ss}$ = 0.63 s), F [9.6485×10^4 coulombs/mol] (Faraday's constant). Data processing after completion of the test begins by determining the value I_o, defined as the value of I when the I vs. t curve reaches its minimum. This background value must be subtracted point by point from I(t). The corrected I vs. t curve is then obtained, from which the value of I_{ss} can be identified. At this stage, the ratio $J(t)/J_{ss}$ is calculated using Eq. 56:

$$\frac{J(t)}{J_{ss}} = \frac{I(t)}{I_{ss}} \qquad \text{Eq. 56}$$

It is then possible to construct the J/J_{ss} vs. t plot, from which t_{lag} is determined, taking care to subtract the time contribution preceding the charging curve. The effective diffusion coefficient is calculated using Eq. 57:

$$D_{eff} = \frac{L^2}{6t_{lag}} \qquad \text{Eq. 57}$$

The H subsurface concentration can be calculated using Eq. 58:

$$C_0 = \frac{I_{ss}L}{AFD_{eff}} \qquad \text{Eq. 58}$$

2.3 Test setup

This section describes the experimental setups, operating conditions, and the types of specimens used in the experimental testing campaign. In the case of custom-made systems, the design and construction phases of the setups are also described. For the fracture mechanics tests, two different types of specimens were selected: SENT and SENB. The first was chosen because its geometry provides the closest similarity to the stress and strain fields at the crack tip that govern the fracture process [229] [230]. The second was selected because, under the available experimental conditions, it allows a more accurate reading of the extensometer.

2.3.1 H charging test

In order to obtain a clear understanding of the H absorption capacity of the steel, H charging tests were performed in a glass electrolytic cell with a capacity of approximately 500 mL (Figure 32a). H charging was conducted using a Gamry Interface 1010E potentiostat operating in galvanostatic mode with a current density $J = -10$ mA/cm². The electrolyte solution consisted of 0.98 g/L of H_2SO_4 (0.01 mol/L) and 2.00 g/L of CSN_2H_4. The working electrode was the specimen, while the counter electrode was a platinum wire wound in a spiral shape and supported by polycarbonate rods in order to surround the specimen (Figure 32b). The reference electrode was a standard Ag/AgCl/KCl 3M . BM specimens were cut into cuboids with dimensions of 1.0 × 0.9 × 1.5 cm³. FZ specimens were obtained by extracting a cylindrical rod with a radius of 8.0 mm from the center of the weld bead and subsequently cutting it into cylinders with a height of 1.3 cm. Some BM specimens were heat treated at 870 °C for 20 minutes and then cooled with forced air from a compressed air line to simulate the HAZ. These specimens were microstructurally and mechanically characterized to verify their similarity to the actual HAZ (Figure 32c). All specimens were polished using P1200 grit abrasive paper. Three batches of 12 specimens each were prepared in order to charge three samples for each of the four selected charging times: 1800, 3600, 7200, and 14400 seconds. To ensure that the electrolyte solution was not altered due to excessively long charging times, it was replaced every four hours, corresponding to the maximum continuous charging time used in the experiment. Each specimen was connected to the potentiostat terminal by means of a steel wire spot-welded to one end of the specimen (Figure 32d). Before H concentration measurements, the samples were cleaned with ethanol, acetone, and diethyl ether. The diffusible H concentration was determined by placing the samples in a thermal desorption analyzer (TDA) Phoenix G4 (Bruker) for 20 minutes at 400 °C, in accordance with ISO 3690 standard [231]. The charging efficiency, defined as the ratio between the amount of H absorbed and the amount

of H reduced on the specimen surface, was estimated by comparing the measured H concentration with the theoretical concentration [ppm] calculated as described in Equation 59 [232]:

$$C_H = \frac{Q_H^{Ev} \cdot MM_H}{zFVd_{steel}} \cdot 10^6 \qquad \text{Eq. 59}$$

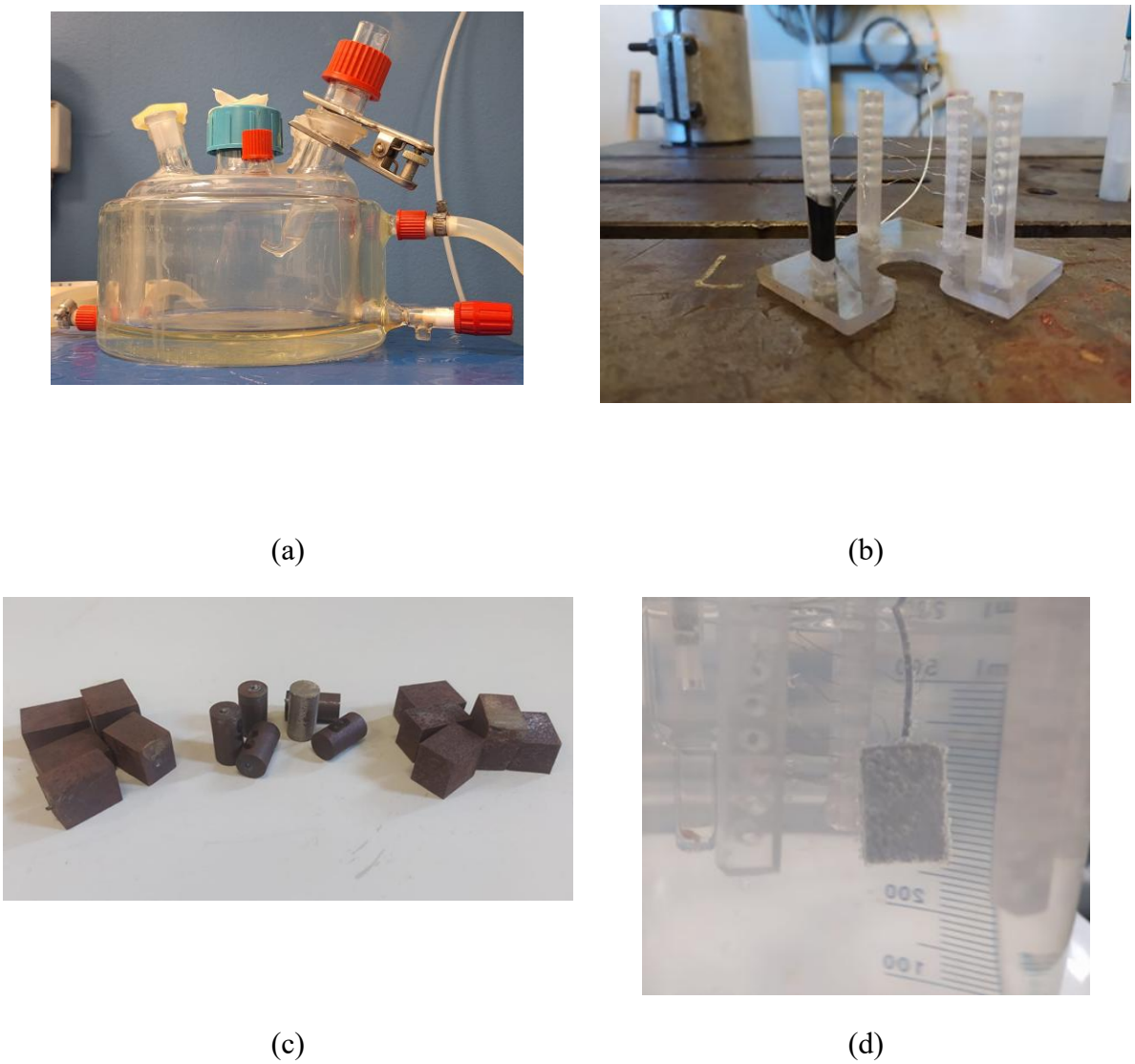

(a) (b)

(c) (d)

Figure 32–(a) *Electrolytic cell used for H charging tests;* (b) *platinum counter electrode;* (c) *appearance of the specimens used for electrolytic H charging tests (after TDA analysis), from left to right: BM, FZ, simulated HAZ;* (d) *BM specimen during a charging test. In the background, the reference electrode and the polycarbonate supports through which the platinum wire passes are visible.*

2.3.2 Fracture mechanics test with SENT specimens

The experimental tests were performed on two distinct sets of specimens. The first set was tested using a Zwick&Roell Z600 universal testing machine adopting the compliance method, whereas the

second set was tested on a Mayes testing machine using the basic method. In both cases, the same experimental setup was employed, specifically designed to be compatible with both testing machines. A cubic test cell with a side length of 12 cm, open on one side, was manufactured using 0.5 cm thick polycarbonate plates. Two threaded holes with a diameter of 12 mm were machined at the bottom of the cell: the first one was intended for draining the electrolyte solution, while the second was used to fix the specimen base. At the top, the specimen was clamped by the upper grip and, from the outside, screwed to the crosshead of the universal testing machine. The grips were manufactured by electrical discharge machining (EDM) from an AISI 316L steel bar and were provided with specially designed slots to accommodate the heads of the SENT specimens used (Figure 33). The specimen heads were wrapped with Kapton tape in order to ensure electrical insulation from the rest of the instrumentation.

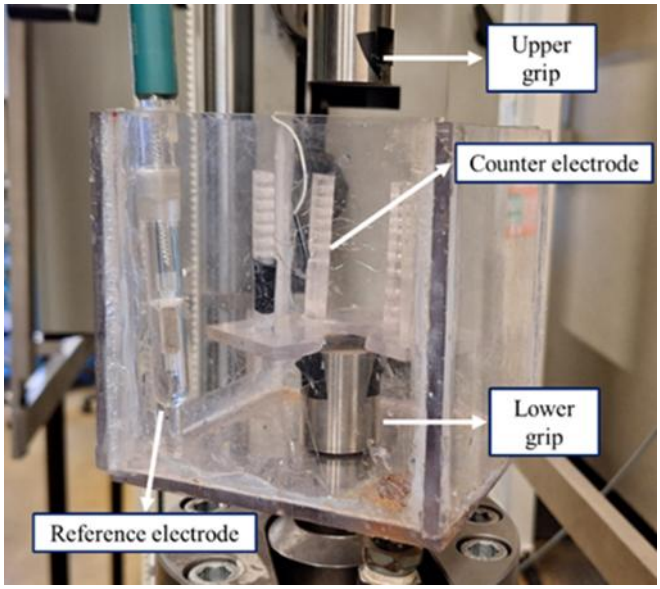

Figure 33-*Electrolytic cell used for mechanical testing with SENT specimen*

For the specimens tested using the compliance method, a commercial extensometer (DT-S/P56, Deltatech) was employed (Figure 34a). For the tests performed using the basic method, a custom-made clip-on device was developed (Figure 34b). This device consists of an aluminum body with a height of 1.4 cm, to which two titanium rods with dimensions of 1.0 × 3.5 cm were bolted. Waterproof, pre-wired strain gauges (1-LE-3/350ZE, HBK) were bonded to each rod and configured in a full Wheatstone bridge, then connected to an InstruNet data acquisition unit. The ends of the rods were covered with PVC adhesive tape in order to ensure electrical insulation of the clip-on device from the specimen. Each of the two specimen groups consisted of six specimens, allowing for one reference specimen tested in air and H charged specimens for the BM, HAZ and FZ. The geometric dimensions of the adopted specimens are reported in Table 11 and in Figure 34b–d. Specimens with

the notch located in the weld were manufactured in the NQ configuration. Prior to testing, all samples were surface-cleaned using P1200 grit abrasive paper. The SENT specimens were fatigue pre-cracked using a Zwick/Roell 250 vibrophore in order to obtain a total crack length (a_0) of approximately 0.5W (Figure 35). In both cases, the crosshead of the tensile testing machine was moved at a displacement rate of 0.05 mm/min, leading to specimen failure in the case of the basic method, and stopping when the load dropped by 20–30% from the maximum load for the compliance method.

Table 11-*SENT specimen dimensions.*

	Basic Method	**Compliance**
W [mm]	7.8	6.0
B [mm]	15.8	12.0
H [mm]	78.0	60
Notch depth	0.5W-2.5	0.5W-2.5

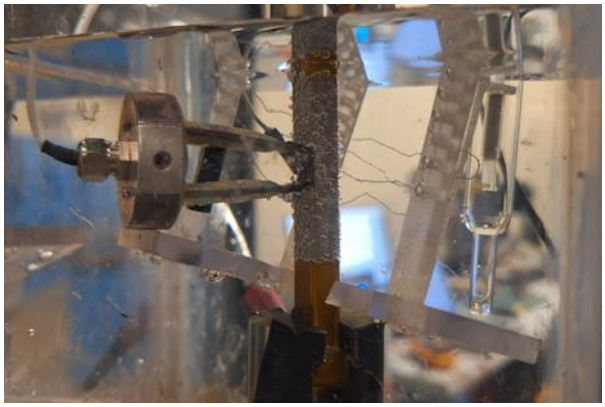

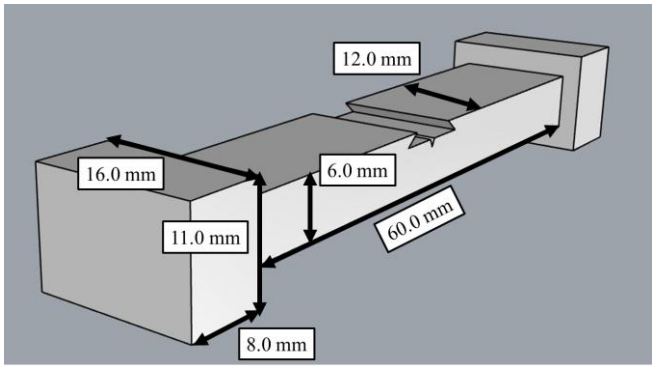

(b)

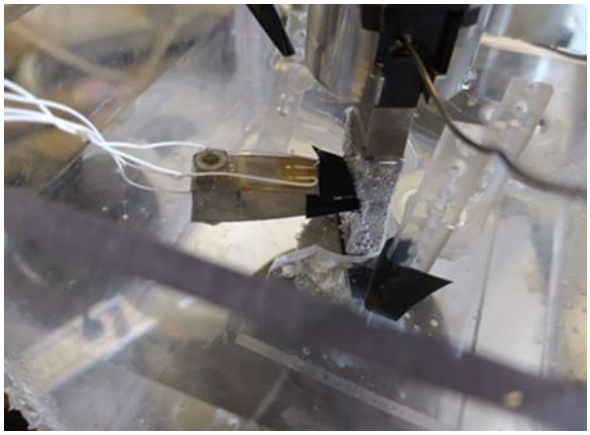

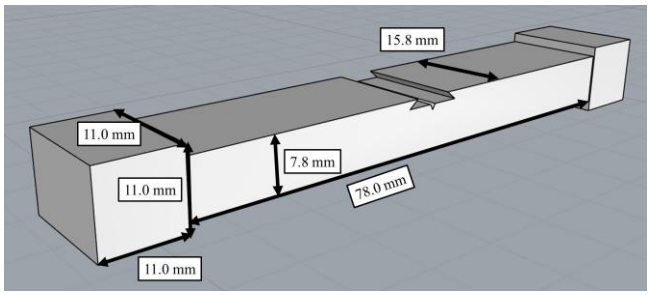

(c) (d)

Figure 34-(a) *Deltatech clip on during the test in electrolytic H;* (b) *SENT specimen compliance method sketch;* (c) *Custom made clip on during the test in electrolytic H;* (d) *SENT specimen basic method sketch.*

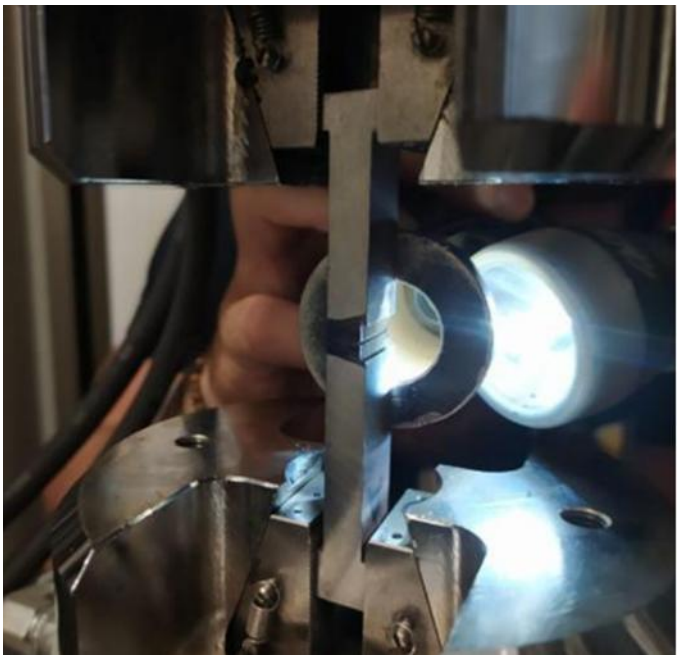

Figure 35-*SENT specimen precraking operation.*

A mild steel wire is spot-welded to the upper head of the specimen and connected to the Gamry Interface 1010E potentiostat. The electrodes, electrolyte solution, and testing conditions are the same as those described in Section 2.3.1.

2.3.3 Fracture mechanics test with SENB specimens

The three-point bending test involves placing the SENB specimen on two rollers, while a punch applies the load from above to induce bending. However, in the case of tests conducted in an electrolytic environment, it is more practical to adopt an inverted configuration, in which the specimen rests on the punch and is loaded from above by the rollers. For this purpose, a new prismatic electrolytic cell with dimensions of 12 × 24 cm was designed and manufactured using 5 mm thick polycarbonate sheets and open on one side. Two threaded holes with a diameter of 12 mm were machined at the bottom of the cell: the first was intended for draining the electrolyte solution, while the second was used to fix the punch. The punch was manufactured from an AISI 304 steel rod with a diameter of 30 mm, on which a hardfacing layer was deposited by SMAW welding using a hard steel filler material (HV10 = 410). Subsequently, the component was machined by EDM to obtain a tip with a curvature radius of 6 mm, and finally cut to reach an overall height of 60 mm. The rollers and their supports were designed using CAD software and manufactured by a specialized workshop using AISI 304 steel. The perspective views of the rollers are reported in Figure 36.

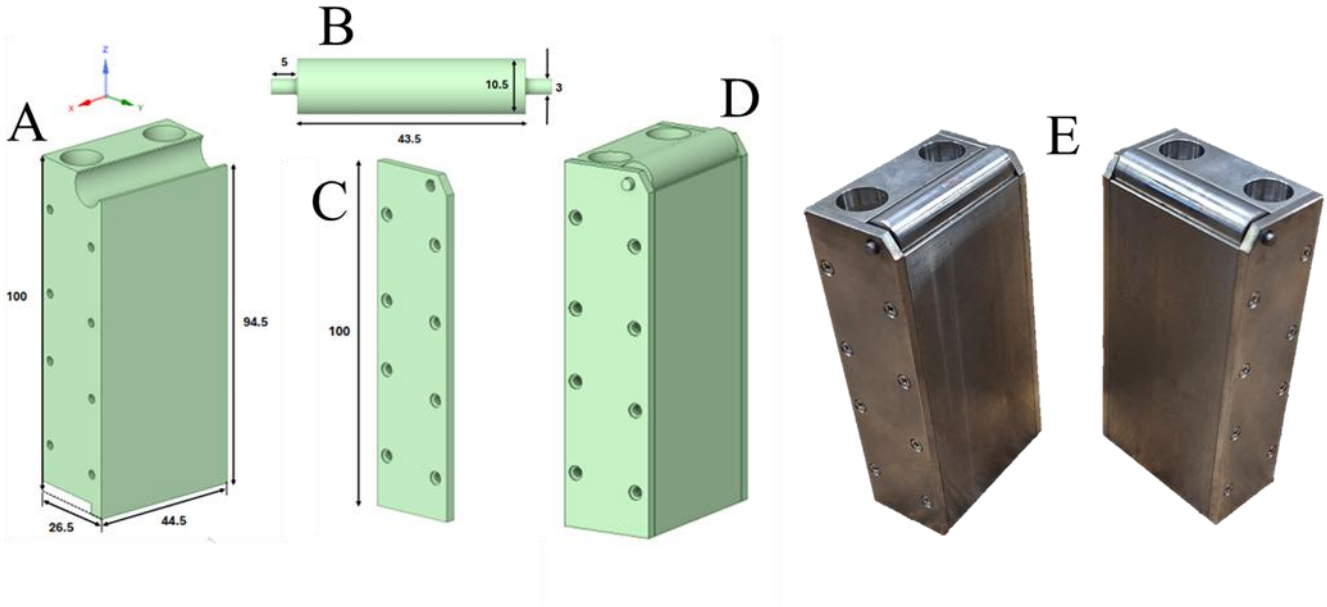

Figure 36–(a) *Body with recess for roller insertion;* (b) *roller;* (c) *plate for locking the roller onto the body;* (d) *roller assembled to the body;* (e) *picture of the actual rollers.*

The recesses at the base of the roller bodies, as well as the geometry of the cell, were designed to ensure compatibility with the Zwick&Roell Z600 universal testing machine. It was also necessary to manufacture a new counter electrode, suitably adapted to the geometry of the new cell. For this purpose, a polycarbonate sheet was shaped to fit inside the cell and centrally drilled to allow the passage of the punch. Four perforated polycarbonate rods were bonded onto this support, through which a platinum wire was threaded and arranged so as to surround the specimen during the test. During testing, the specimen heads and the punch were covered with PVC insulating tape to ensure electrical insulation. For the same reason, the clip-on extensometer was covered with Kapton insulating tape (Figure 37). Five BM specimens, three specimens with notch trought thickness in the HAZ (NP configuration), three with surfcace notch in the HAZ (NQ configuration), and three with notch through thickness in the FZ NP configuration were tested. The specimen dimensions are reported in Table 12 and Figure 38.

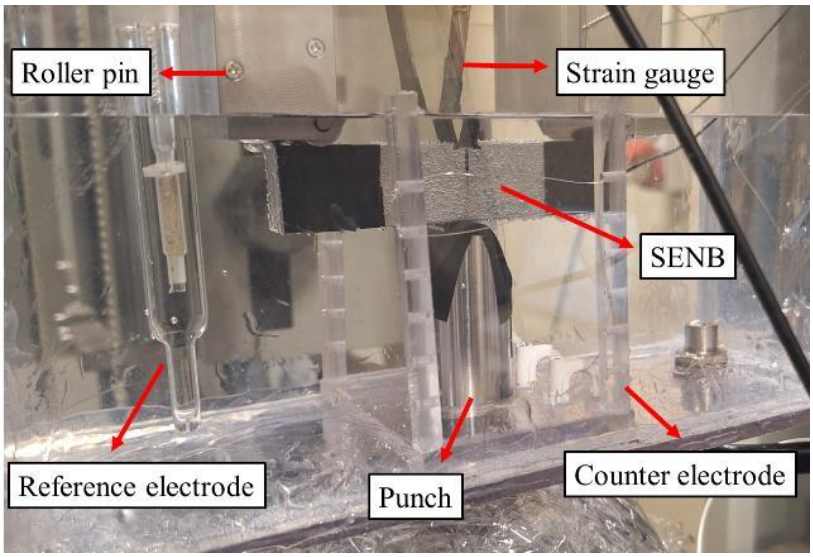

Figure 37-*Electrolytic cell with SENB during the test.*

Table 12-*SENB specimens dimensions.*

Notch position	**BM**	**HAZ NP**	**FZ NP**	**HAZ NQ**
W [mm]	20	20	20	10
B [mm]	10	10	10	10
H [mm]	100	130	130	100
S [mm]	80	80	80	40
Notch depth	0.5W-2.5	0.5W-2.5	0.5W-2.5	0.5W-2

The pre-cracking procedure and testing parameters were the same as those adopted for the SENT specimens (Figure 39). A Sandner EXRC10-12.5o clip-on extensometer was used for the BM specimens, whereas an Epsilon 3541-005M-120M-ST extensometer was employed for the welded specimens. All tests were conducted using the compliance method. The percentage of HAZ in the HAZ NP specimens was calculated in accordance with ISO 15653 [233].

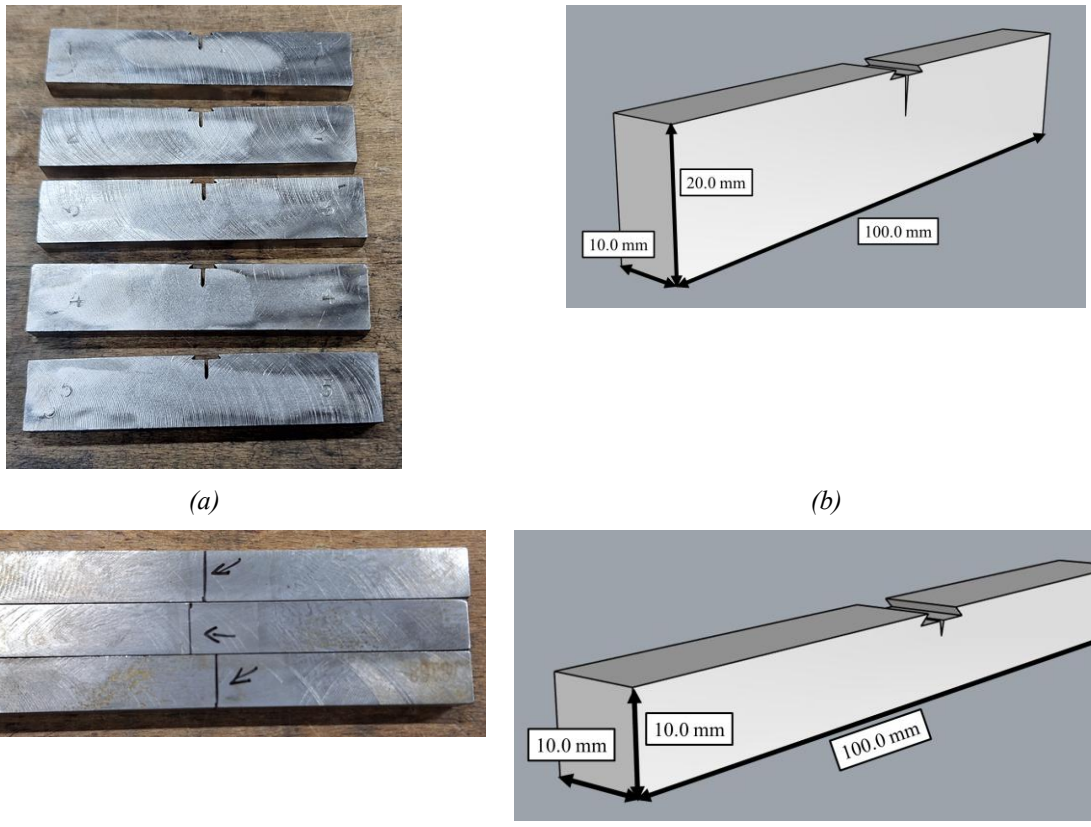

(a) *(b)*

(c) (d)

Figure 38-(a) *SENB BM specimens;* (b) *SENB BM specimens sketch;* (c) *SENB HAZ NQ spoecimens;* (d) *SENB HAZ NQ sketch.*

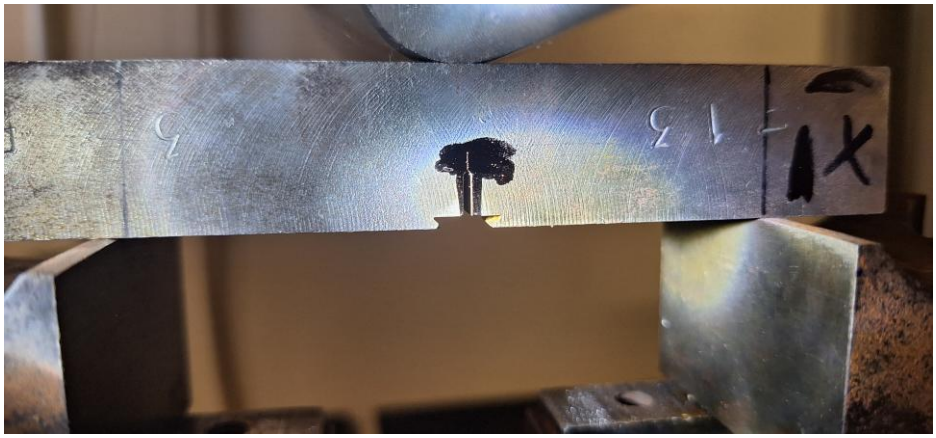

Figure 39–*Fatigue pre-cracking of the SENB specimen. The light highlights the growing fatigue crack, making it sparkle.*

2.3.4 H permeation test

H permeation tests were performed using a Devanathan–Stachurski cell. The experimental setup consists of two half-cells, each with a volume of approximately 500 mL, provided with a lateral opening with an inner diameter of 1.50 cm. The metallic specimen is placed between the two half-

cells and held in position by a clamping device, ensuring hermetic separation of the two compartments. A platinum counter electrode is inserted into the charging compartment, while the discharging compartment contains a platinum electrode, an Ag/AgCl reference electrode in 3 M KCl, and a probe for monitoring the temperature of the electrolyte solution. In both compartments, a capillary for nitrogen purging is also installed in order to maintain a deoxygenated environment. The entire cell is placed on a heating plate, directly coupled to the temperature probe for thermal control of the system (Figure 40).

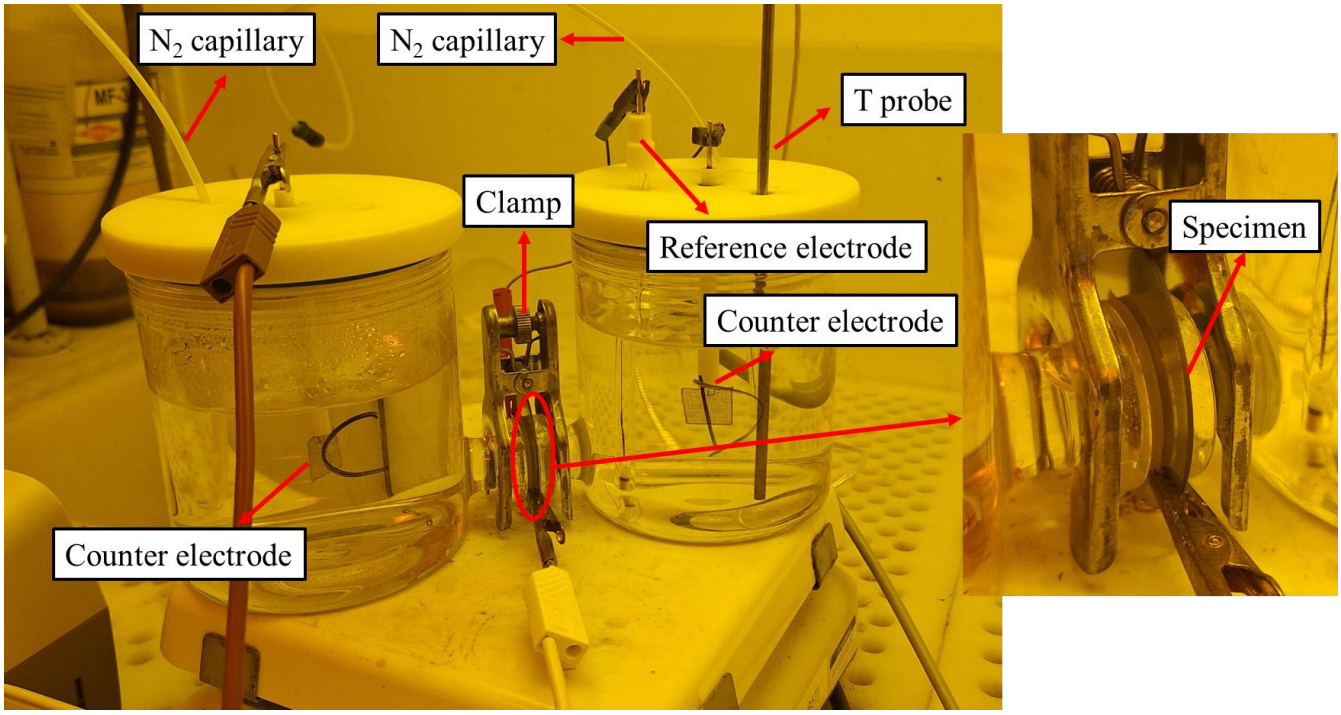

Figure 40-*DS cell; left charging side, right discharging side and specimen magnification.*

From the API X52 steel pipe, sections with dimensions of 60 × 120 × 10 mm³ were extracted, some of which contained the girth weld. Two tiles were subjected to a constant load corresponding to 5% and 10% above the yield strength Rp_{02}, applied for 1 minute, corresponding to stresses of 452 MPa and 473 MPa, respectively. Cylinders with a diameter of 47 mm were then obtained from the tiles by EDM and subsequently sectioned into disks with a thickness of 1 mm. The disk surfaces exposed to the electrolyte solution included the weld zone with NQ orientation and the BM with XZ orientation (Figure 30). Overall, 7 BM specimens, 7 welded specimens (W), and 2 specimens for each applied stress level (S5 and S10) were tested. Prior to testing, all samples were conditioned in an oven at 80 °C for 24 hours. Subsequently, the surfaces were prepared by grinding with abrasive papers up to P1200 grit. The welded specimens were additionally chemically etched with 5% Nital to highlight the weld bead (Figure 41). Then the specimens were cleaned in an ultrasonic bath with isopropanol

for 5 minutes. The boundaries of the FZ were marked with a white insulating marker in order to allow exposure of only the weld to the charging solution. The thickness of each specimen was measured three times using a caliper, and the average value was used for data analysis. The charging (0.01 M H_2SO_4 with 2.00 g/L TU) and discharging (0.1 M NaOH) electrolyte solutions were preheated to 30 °C on a heating plate and degassed by nitrogen purging for 30 minutes. Once the DS cell was assembled with the specimen placed between the two half-cells, the discharging solution was initially introduced. The specimen was anodically polarized at +300 mV vs. SCE and maintained in the discharging phase for 1.5 hours. Subsequently, the charging solution was introduced into the left compartment and the specimen was cathodically polarized at a constant current density of −10 mA/cm², recording the first permeation transient for 1.5 hours. At the end of the charging phase, the specimen was disconnected from the charging circuit and the electrolyte solution was removed using a peristaltic pump. The exposed surface was then rinsed three times with deionized water. During this phase, the discharging process continued for an additional 3.5 hours. Afterwards, the charging solution was reintroduced and cathodic polarization was restored in order to record a second permeation transient for an additional 1.5 hours. At the end of the test, the specimen was removed from the cell, washed with deionized water, dried, and stored between two lens-cleaning tissues, sealed inside a zip-lock bag.

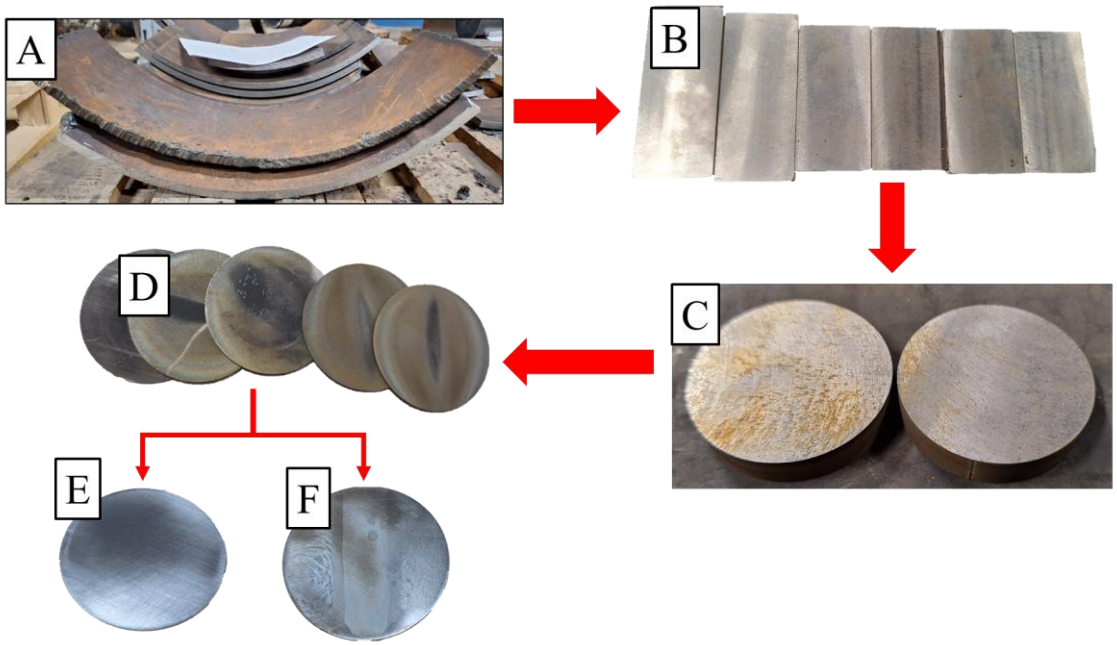

Figure 41–(a) *API 5L X52 pipe;* (b) *tiles extracted from the pipe;* (c) *cylinders cut from the tiles;* (d) *specimens before cleaning;* (e) *polished BM specimen;* (f) *polished W specimen etched with 5% Nital.*

Once the test is completed, the total trap concentration (N_T), as well as the reversible (N_{rev}) and irreversible (N_{irr}) trap concentrations, can be calculated using Eq. 60 [234]:

$$N_T = \frac{nC_0}{3}\left(\frac{D_L}{D_{eff}} - 1\right) \quad \text{Eq. 60}$$

where n is the number of electrons exchanged by H, and D_L is the lattice diffusion coefficient (1.28×10^{-4} cm²·s⁻¹). The calculation of N_{rev} also follows Equation 60 and is determined from the second H permeation curve. Conversely, the trapping density obtained from the first H permeation test corresponds to the total trapping density, which includes both reversible and irreversible traps. Therefore, N_{irr} is derived by subtracting the reversible trapping density calculated from the second test from N_T.

2.3.5 Novel permeation set up

The new permeation setup is based on the use of a quadrupole mass spectrometer (QMS) for H detection, replacing the oxidation compartment of the traditional DS cell. This approach allows a direct measurement of the permeating H flow. The resulting system is therefore a hybrid configuration in which H is electrolytically charged and detected in the gas phase by QMS. A polycarbonate electrolytic cell with a wall thickness of 3 mm and dimensions of 22 × 22 × 30 cm³, equipped with a lid, was manufactured. The connection between the specimen and the cell is ensured by a tube pressed against the specimen surface by means of a clamp. The first tube prototype was machined on a lathe from a polycarbonate bar; however, this component proved to be too small and fragile and required silicone bonding to the cell wall (Figure 42a). Subsequently, the design was revised in order to increase the tube thickness to improve mechanical robustness and to enlarge the specimen area exposed to the electrolyte solution. Moreover, the body was threaded to allow direct screwing into the electrolytic cell (Figure 42b). This second prototype was manufactured by 3D printing in polylactic acid (PLA). The final version of the component was 3D-printed in polyethylene terephthalate (PET) and equipped with an additional inner tube. This tube, directly connected to the peristaltic pump, allows suction of the H_2 bubbles forming on the specimen surface and, at the same time, ensures continuous renewal of the electrolyte solution at the surface (Figure 42c). Two nuts made of the same material were also produced for fastening the component to the cell, with a flat O-ring inserted to prevent possible solution leakage. All components intended for vacuum operation were supplied by LewVac. The specimens used are the same as those employed in the DS permeation tests, since their diameter is compatible with standard CG40 copper gaskets, which are required to ensure the ultra-high vacuum conditions demanded by the QMS. The gaskets were mounted between

two DN40CF flanges (one threaded and one plain). The specimen disk was bonded between the two gaskets, forming a sandwich structure. This assembly was tightened between two standard DN40CF flanges and placed in an oven at 50 °C for 24 hours to allow complete curing of the adhesive Araldite 2014-2 (Figure 43).

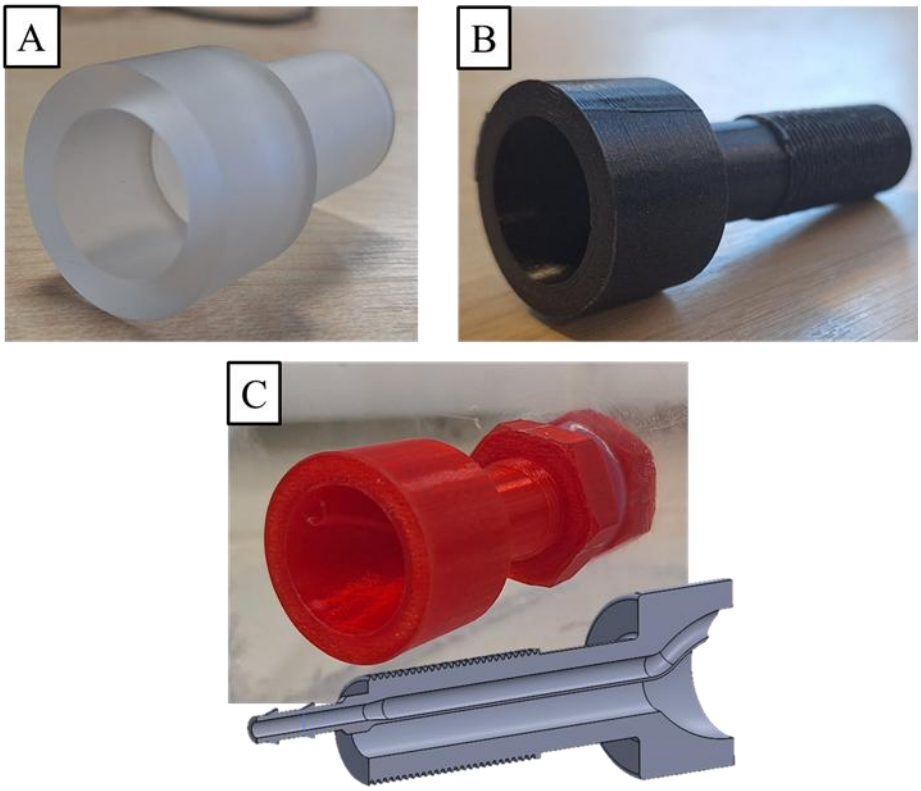

Figure 42–(a) *First polycarbonate tube prototype;* (b) *second prototype in PLA with threaded body;* (c) *final specimen holder and its design cross-section.*

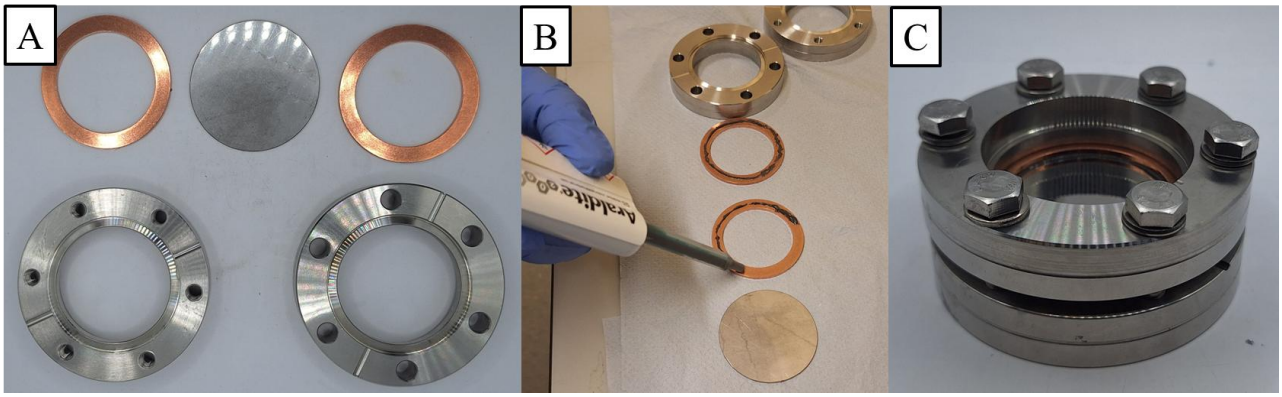

Figure 43–(a) *Flanges, copper gaskets, and specimen;* (b) *specimen assembly;* (c) *specimen placed in the oven.*

The specimen support clamp was obtained by machining a blind DN40CF flange so that it could be screwed together with the specimen sandwich onto the 125 mm FL-SC40CF adapter. This adapter

leads to the gate valve GV-40CF-C-M, which allows interruption of the H flow if necessary, thus acting as a safety device for the QMS. Downstream of the valve, a ZFL cross adapter is installed, featuring two DN40CF ports and two KF25 ports. A Pfeiffer HiCube turbomolecular pump is connected to the lower KF25 outlet to ensure the operating pressure required for the QMS (≈10^{-7} mbar). At the upper outlet, a two-way fitting is mounted for connection of the pressure sensor and the calibration leak. A further FL-SC40CF adapter finally connects the system to the e-Vision 2 mass spectrometer. On the front wall of the cell, dedicated holes were machined to allow the passage of the peristaltic pump lines, the nitrogen line for solution degassing, the platinum counter electrode, and the Ag/AgCl, KCl 3M reference electrode (Figure 44).

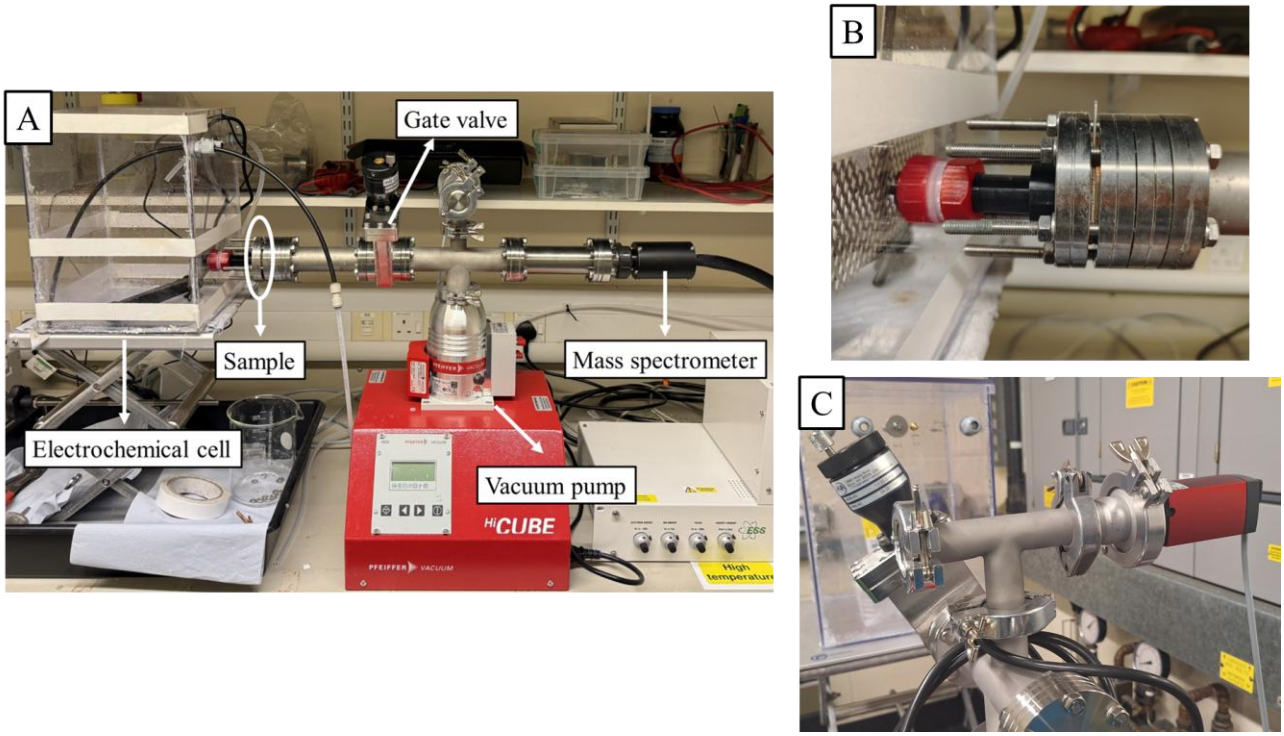

Figure 44-(a) *New apparatus for direct evaluation of H permeation;* (b) *detail of the specimen, clamp, pipe and counter electrode;* (c) *pressure probe.*

3. Results and Discussion

3.1 Electrolytic H charging test

The girth weld HAZ is too small to allow isolation from the surrounding material and subsequent experimental characterisation. For this reason, it was decided to reproduce it artificially from the BM using appropriate heat treatments. Three prismatic BM samples, obtained according to the dimensions indicated in paragraph 2.3.1, were heated in an oven at 870 °C for 20 minutes. Subsequently, the samples were cooled in three different ways: the first in calm air, the second in forced air and the third quenched in water at room temperature. The resulting microstructures were analysed using LOM and SEM (Figure 45). The sample cooled in calm air shows a microstructure similar to that of BM, consisting mainly of ferrite and pearlite, but characterised by significant grain refinement and loss of preferential grain orientation. The faster cooling in forced air favoured the formation of a bainite fraction in the second specimen, accompanied by further microstructural refinement. As expected, the water-quenched specimen has an extremely fine microstructure, consisting mainly of lower bainite and limited martensitic regions. Samples were subsequently subjected to Vickers HV10 hardness tests and the results were compared with those for the original HAZ (Table 13). The analysis clearly shows that the water-quenched sample has neither a microstructure nor a hardness value comparable to those of the actual HAZ. Among the air-cooled samples, the sample cooled in forced air shows a hardness value closer to that of the original HAZ. Based on these preliminary results, the average grain size was determined in accordance with DIN EN ISO 643:2012 [235], supported by ASTM E112-10 [236]. The results (Table 14) indicate that the sample cooled in forced air has a grain size more similar to that of the original HAZ than the sample cooled in calm air. Therefore, the sample cooled in calm air was discarded, while the sample cooled in forced air was further characterised by quantitative analysis of the microstructural phases, conducted in accordance with ASTM E562-11 [237] and ASTM E1245-03 [238] standards, in order to confirm its representativeness with respect to the actual HAZ. The results, shown in Table 15, show good agreement between the two analysis methods. In this evaluation, ferrite was considered as the primary phase, while bainite and pearlite were grouped as secondary phases. The phase percentages obtained for the sample cooled in forced air are comparable to those measured in the original HAZ.

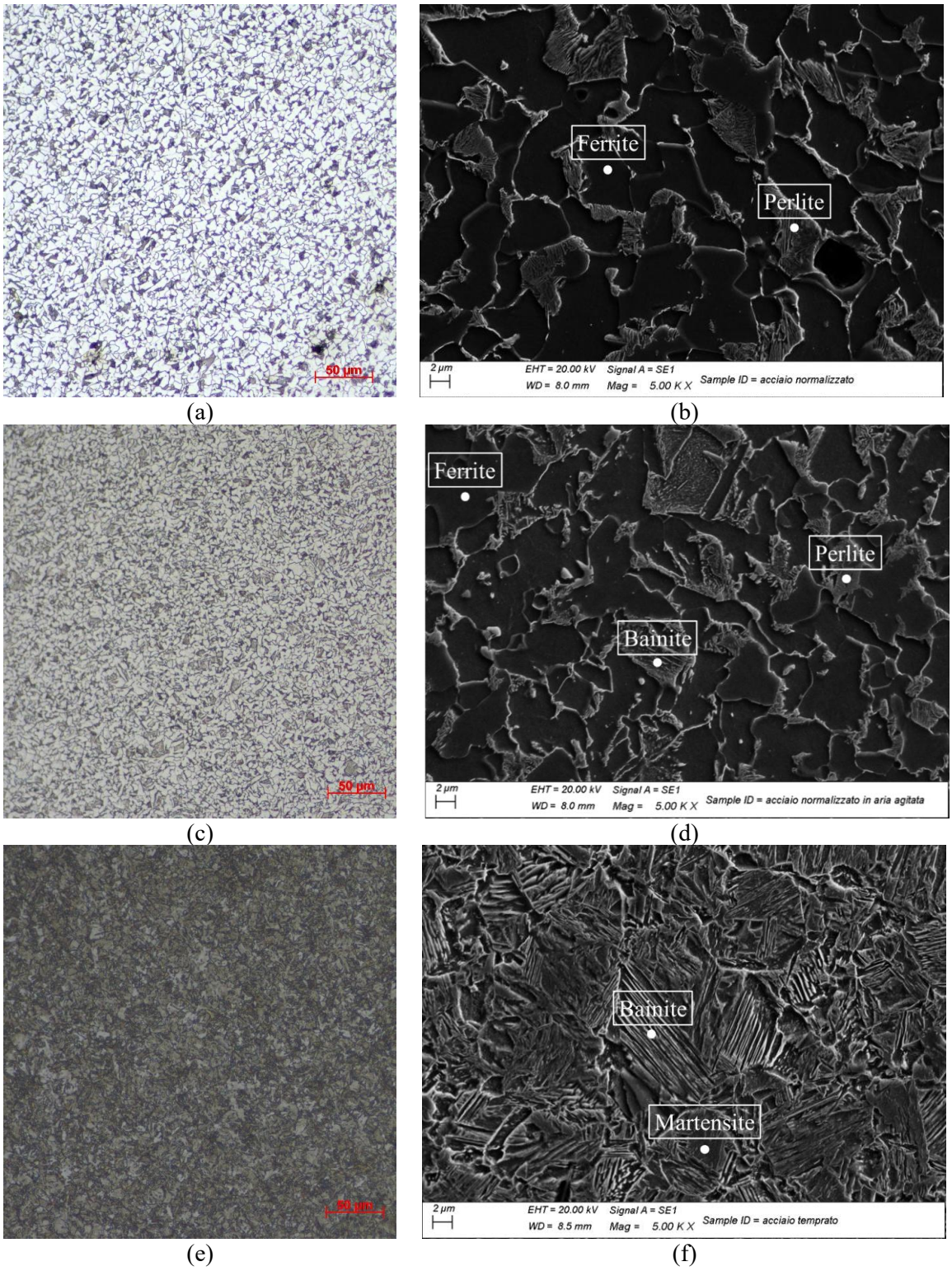

Figure 45-*Micrographs of the heat treated samples:* (a) *BM normalised calm air LOM 200X;* (b) *Normalised BM in calm air SEM 5000X;* (c) *Normalised BM in forced air LOM 200X;* (d) *Normalised BM in forced air SEM 5000X;* (e) *BM quenched in water LOM 200X;* (f) *BM quenched in water SEM 5000X.*

Table 13-*Hardness of the original HAZ and test specimens after heat treatment*

Specimen	HAZ	Calm air	Forced air	Water
HV10	206,9 ± 10,7	170,4 ± 2,2	190,5 ± 7,3	417,3±34,9

Table 14-*Grain size of the original HAZ and samples cooled in calm and forced air.*

Specimen	HAZ	Calm air	Forced air
N°ASTM grain size	13,4±0,9	12,0	13,0

Table 15-*Phase percentage analysis for ZTA samples and material cooled in forced air.*

Specimen	HAZ	Forced air
Phase percentage ASTM E562	23,87±3,93	23,73±4,26
Phase percentage ASTM E1245	21,66±1,92	19,43±1,95

Considering the similarity in terms of microstructure, hardness, grain size and phase percentages between the sample cooled in forced air and the original HAZ, it was decided to use this sample as a substitute material for the HAZ in subsequent H loading tests.

The results obtained for the H charging test are shown in Figure 46. The H absorption efficiency, calculated according to Eq. 59, is summarised in Table 16. All three materials showed sensitivity to hydrogenation under the selected loading conditions. A certain dispersion of the data is attributable to:

- Non-deaerated solution. oxygen competes with H in the reduction process, thus reducing the HER yield (paragraph 1.2.2).
- Non-constant distance between the samples and the electrodes. The electrical resistance of the solution varies depending on the distance between the electrodes and the samples. If a sample is further away, it may experience greater resistance, reducing the efficiency of the applied current and therefore the rate of H evolution [239].
- Complex chemical equilibria that develop at the metal-solution interface. In acidic solution, H is reduced and absorbed by a series of chemical equilibria described by the Volmer, Tafel and Heyrovsky equations.
- Time elapsed between sample collection and the start of TDA. In fact, H concentrations are very low and H diffuses rapidly into ferrite [56].

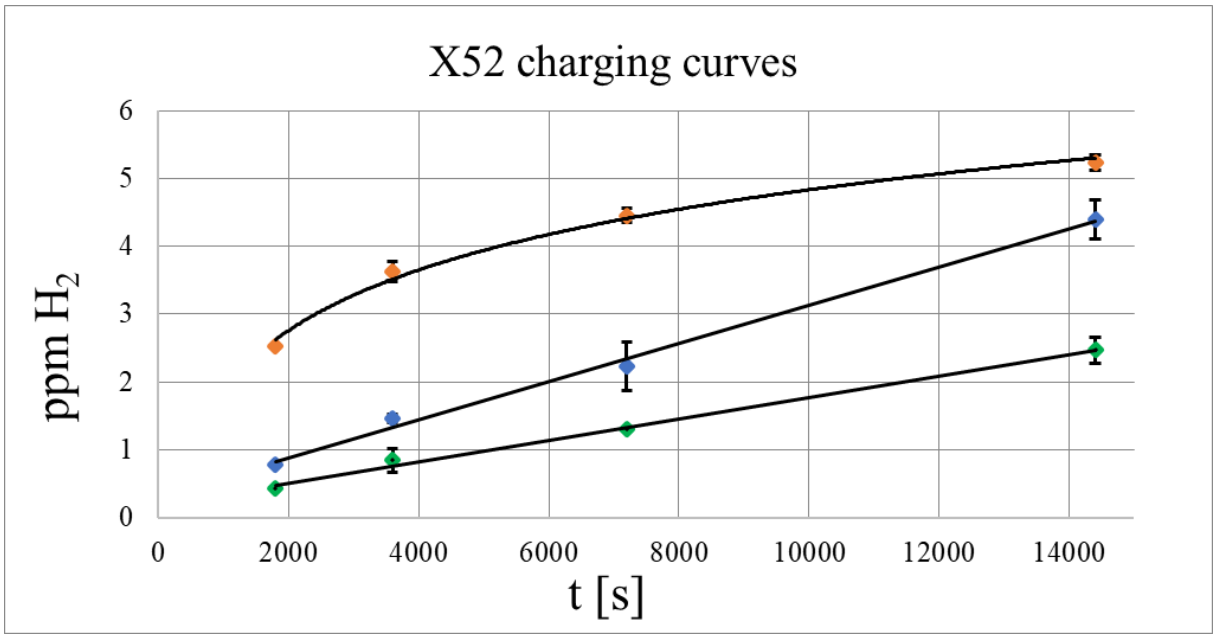

Figure 46-*Electrolytic hydrogen charging curves of BM (blue), HAZ (green) and FZ (orange).*

The typical trend of H charging in steel is a curve that rises until it reaches a plateau when saturation conditions are reached [131] [240] [241]. Specifically, the three curves show an upward trend that culminates in the maximum H concentration value for t = 14400 s. It is interesting to note that for BM it was possible to load approximately 1 ppm of H/h. The higher amount of H charged by the FZ was predictable, as it was caused by the finer microstructure, high concentration of dislocations and residual stresses typical of the welding process. However, fine structures, such as bainite or acicular ferrite, are less sensitive to HE, as they act as irreversible traps, slowing down the movement of H [139]. Similarly, one would expect the HAZ to be able to store more H than the BM, but this was not the case. The explanation is in the microstructure of the BM. The morphology of the inclusions is fundamental in the development of HE, which is more pronounced when they have an elongated shape (created by the rolling process). This is because H atoms tend to concentrate more at the ends of the inclusions, where the stress concentration is usually higher [242]. Furthermore, for the same mass, an elongated inclusion has a larger surface area than a globular one and therefore offers more preferential sites for H storage. In general, a low concentration of elongated inclusions is more critical than a high concentration of rounded inclusions, as described by the stress concentration theory [243].

Table 16-*H charging yields of the specimens tested in this work*

	t [s]	Yield %
BM	1800	0.63
	3600	0.53
	7200	0.43
	14400	0.37
HAZ	1800	0.31
	3600	0.32
	7200	0.25
	14400	0.25
FZ	1800	1.61
	3600	1.17
	7200	0.72
	14400	0.42

Under charging conditions, these elongated inclusions are susceptible to H accumulation at the interface and produce cracks, which in turn attract even greater amounts of H. This phenomenon creates a concentration of stress at the tip of the crack, from which it spreads along the rolling direction. The HAZ grains, however, have undergone a normalisation process: they have entered the γ field and cooled rapidly. The heat treatment has refined the grains and caused them to lose their rolling orientation. Therefore, with the same number of phases (ferrite and pearlite), the HAZ can store less H than the BM because the grains and inclusions are not elongated and oriented in a single direction. Three BM samples were tested under the same conditions, but for 18,000 s. The average H concentration observed was 2.43 ppm. As already reported [133] [134], after a certain charging period, the H concentration decreases due to the high number of bubbles that form on the surface of the sample. They have a dual effect: on the one hand, they improve the strength of the steel (in fact, the surface potential gradually increases during the test) and, on the other hand, they hinder the introduction of additional H into the crystal lattice. Regarding charging yields, calculations show that even under improved configuration conditions, almost all the H produced recombines into a molecule and leaves the electrolytic cell. The rate of entry depends on many variables: the nature of the metal, its composition and thermomechanical history, surface conditions, electrolyte composition, cathode

current density, electrode potential, temperature, pressure, concentration and chemical nature of the recombination inhibitor, and saturation of the subsurface layers. As shown in Table 16, the charge yield decreases with increasing time, since in all solutions, as the amount of dissolved solute increases, it becomes increasingly difficult to solubilise it.

3.2 Fractographic analysis of SSRT specimens

The fracture surfaces of the SSRT specimens described in paragraph 1.8 were characterised using Electron Backscatter Diffraction (EBSD) in order to determine the nature of the inclusions and clarify the mechanisms responsible for the HE phenomenon. The results relating to the scanned area (Fig. 47a) show a marked concentration of manganese in the elongated inclusions. EBSD analysis performed on the same inclusions identified α-MnS as the main phase present (Fig. 47b).

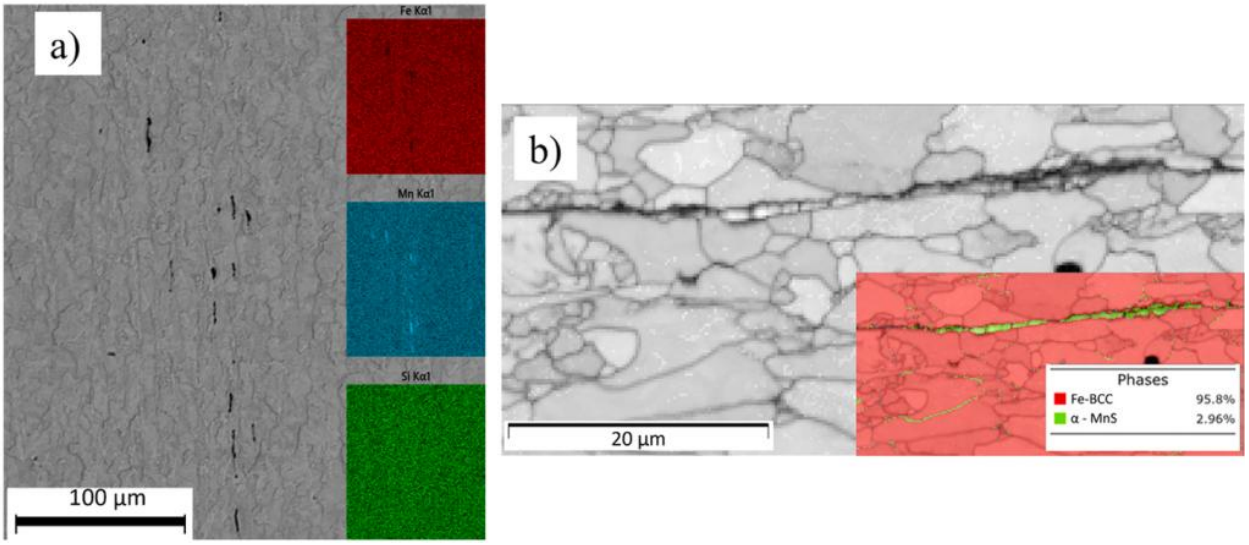

Figure 47-*SEM image of inclusions in the BM* (a). *EDS composition maps for Fe, Mn and Si are shown.* (b) *EBSD map shows composition of an elongated inclusion.*

EBSD also made it possible to identify more clearly the pearlite bands in both the brittle outer ring (Fig. 48a) and the ductile inner core (Fig. 48d), which were oriented along the rolling direction, corresponding to the x-axis of the figures. Fig. 48d shows that the elongated inclusions located near the pearlite bands, particularly in the regions adjacent to the fracture surface, are associated with the formation of microvoids during mechanical testing. The Kernel Average Misorientation (KAM) maps show the absence of significant plastic deformation in the brittle fracture region (Fig. 48c), while in the core of the specimen the level of deformation near the fracture is high (Fig. 48f). These maps also highlight a concentration of crystalline distortion at the pearlite bands in both the ductile and brittle regions of the sample. The Inverse Pole Figure (IPF) maps reveal a mixed transgranular and intergranular fracture mechanism in the outer zone of the specimen (Fig. 48b), confirming the crack

propagation path previously observed. In the central part of the sample (Fig. 48e), on the other hand, there is marked grain deformation, indicative of predominantly ductile behaviour. From a fractographic point of view, the ductile fracture mechanism observed in the samples tested in air, dominated by the nucleation and coalescence of microvoids at the inclusions, is progressively replaced by a brittle fracture induced by H. This fracture originates from the periphery of the sample and propagates towards the inner core. The presence of secondary cracks near the fracture zone is attributable to H absorption, which causes local stress concentration. Their relatively uniform distribution around the fracture surface contributes to a progressive reduction in the resistant section, favouring the coalescence of cracks on different planes and determining the fracture mode observed. The presence of a mixed brittle-ductile fracture in HE phenomena is widely reported in the literature [28] [244] [245]. In the samples charged with H, notches oriented transversely to the direction of crack propagation were observed, developed along the direction of rolling and applied load, in correspondence with the brittle fracture regions. These notches are associated with inclusions which, under uniaxial loading, favour the nucleation of microvoids, as commonly observed in steels containing inclusions. However, during brittle fracture, these inclusions are sheared off, preventing their elongation under tensile stress and hindering the formation of cavities. This behaviour can be interpreted in the light of the HEDE and HELP models, as well as their interaction as a function of loading conditions. H can be distributed both inside the specimen and near the surface [246]. While the migration of H from the surface to the core of the material is governed by a diffusive process described by Fick's laws, the sub-surface concentration depends heavily on the efficiency of the electrochemical loading method and can be traced back to a surface-type model. The results obtained show that the electrochemical parameters used have a decisive influence on H absorption, generating different behaviours depending on the charging conditions. A significant example is the blistering observed in the sample when particularly severe parameters are applied. During electrochemical charging, H is initially absorbed in the sub-surface regions and then slowly diffuses into the material. When the charging efficiency is high enough to ensure significant absorption without causing blistering, the diffusion rate is lower than the absorption rate, resulting in H accumulation in the sub-surface areas. The high concentration of H in these regions promotes the saturation of trapping sites (grain boundaries, inclusions and dislocations), contributing to the formation of a zone characterised by a high triaxial stress state, in which nucleation and dislocation mobility are strongly inhibited. EBSD maps show an accumulation of crystalline distortion along the pearlite bands in both ductile and brittle regions, confirming that pearlite is a more effective H trapping site than ferrite [234]. Ferrite/pearlite interfaces and inclusions represent irreversible traps [247]; therefore, the high density of these interfaces, due to the chemical composition of the material and the manufacturing process,

suggests a greater susceptibility of this vintage steel to accumulate H. The experimental results highlight the presence of a brittle fracture ring in the outer region of the sample, with no obvious signs of plastic deformation on the fracture surface, behaviour mainly attributable to the HEDE mechanism. However, this interpretation is only valid after H saturation and does not fully describe the initial condition of the in situ mechanical tests, in which the H concentration within the sample volume is close to zero. It has been proposed that crack nucleation at the sample surface is caused by the pinning effect of adsorbed H on surface dislocations, in accordance with the HELP mechanism. The literature indicates that the predominance of the HELP or HEDE mechanism depends on the local concentration of H [248]. It is therefore reasonable to assume that the fracture in the outer region results from competition between both mechanisms: HELP is dominant during crack nucleation at low H concentrations, while propagation occurs when the concentration becomes high enough to generate a critical triaxial stress state, leading to a brittle fracture attributable to the HEDE mechanism. In the core of the sample, the H concentration is determined exclusively by diffusion from the surface, resulting in lower concentrations than in the sub-surface regions. Under these conditions, the amount of H is not sufficient to generate high triaxial stress states, but it is still adequate to activate the shielding effect on dislocations, promoting their mobility and inducing localised plasticity. The fractographic images show larger dimples in terms of size and density in the core of the sample, confirming a more ductile behaviour. The combination of a low H concentration and a high density of elongated inclusions allows the development of accentuated localised plasticity during mechanical testing, producing voids that are larger than those in samples tested in air. The results indicate a variation in the role of MnS inclusions depending on the fracture mechanism: at low H concentrations, they promote the nucleation and growth of voids along the direction of the applied load; at higher concentrations, they promote the propagation of secondary cracks oriented transversely to the load. During mechanical testing, brittle and ductile fracture contribute independently to the failure of the specimen; however, their combined effect results in a marked reduction in fracture elongation. Integrated fractographic analysis using SEM and EBSD provides clear evidence of the coexistence of the two mechanisms. The mixed fracture nucleates from the surface of the specimen and penetrates to a certain depth, followed by a brittle-ductile transition zone, and then evolves into completely ductile behaviour in the inner core. This trend is consistent with the results of SSRT tests conducted both in gaseous environment [196] [234] [244] [245] and under electrochemical conditions [28].

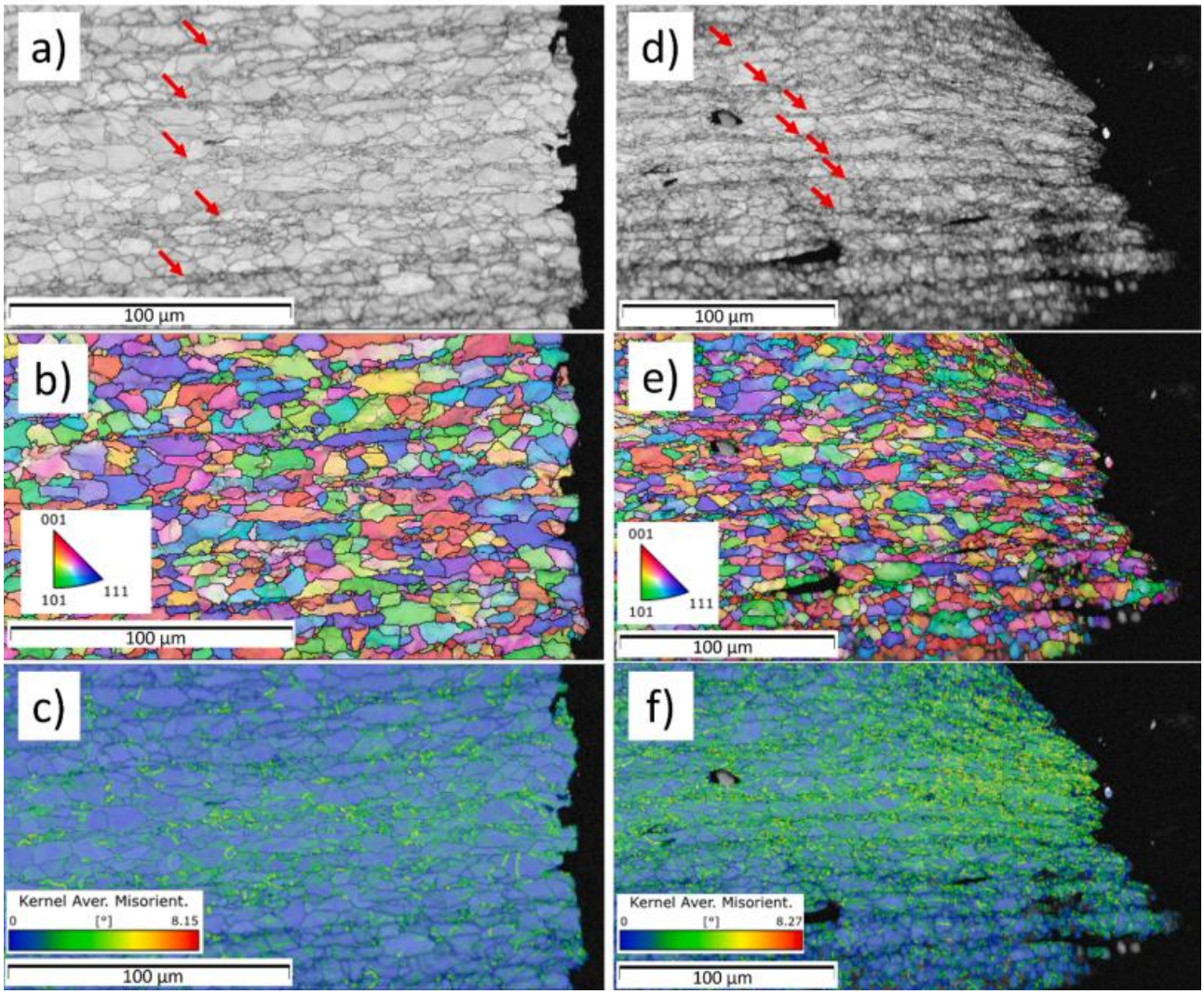

Figure 48-*EBSD characterization of the outer brittle fracture* (a, b, c) *and the inner ductile core* (d, e, f). *Maps shown are, from top to bottom, GB + Pearlite bands (red arrows), GB+ IPF and KAM.*

3.3 Fracture mechanics tests

3.3.1 SENT Specimen-Compliance Method

This experimental campaign yielded unsatisfactory results because the sensitivity of the strain gauge was insufficient to record acceptable data (Figures 49a). In fact, the geometry of the SENT sample, with the same force and dimensions, produces lower CMOD values than other types of samples such as SENB. As can be seen from Figures 49b-c-d, the F vs CMOD plots show some disturbed unloadings, especially in the first part of the curve, which do not allow for correct post-test processing.

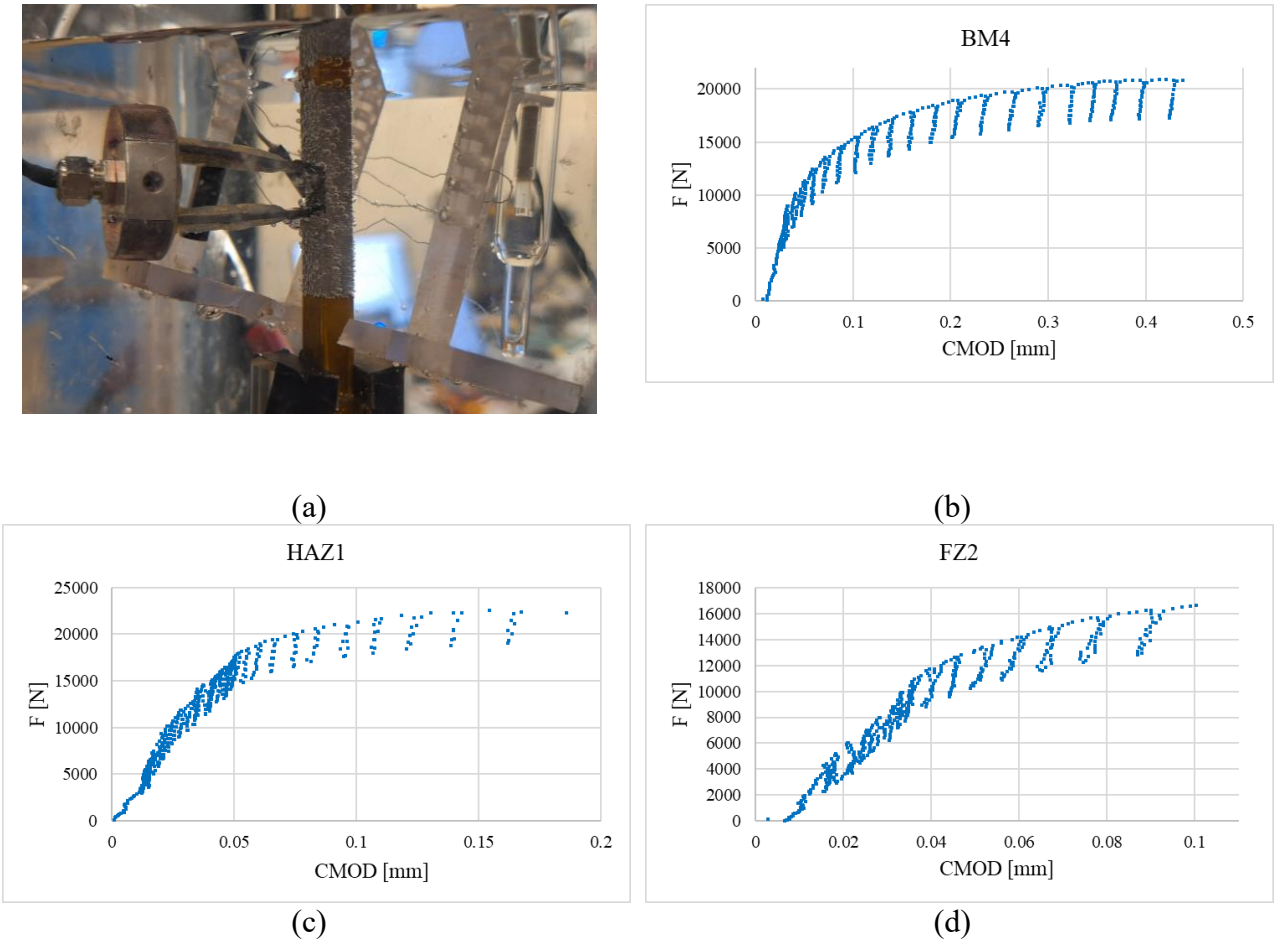

Figure 49-(a) *SENT with in situ charging;* (b) *BM H charged specimen;* (c) *HAZ air tested specimen;* (d) *FZ H charged specimen.*

3.3.2 SENT Specimen-Basic Method

The Force–CMOD curves of the samples tested in air and under electrolytic loading are shown in Figure 50, while the maximum values of the integral J, calculated according to Eq. 51, are summarised in Table 17. The ratio $J_{MAX\,H}/J_{MAX\,Air}$ was adopted as a quantitative index of the embrittlement induced by the H charge. The charging conditions considered, already used in the previous experiment, determined an H concentration during the test time (approximately 5400 s) higher than the critical value of 1 ppm. Analysis of the Force vs. CMOD curves shows that the H charged samples reach the maximum load at lower CMOD values than those tested in air and undergo early failure, thus showing a lower final CMOD. Although BM has greater toughness in air, it is more sensitive to H loading, as shown by the data in Table 6. As discussed in Section 3.2, elongated inclusions play a decisive role in H absorption mechanisms and crack nucleation [243]. Under air test conditions, the ferritic-pearlitic microstructure of the BM shows superior toughness compared to that of the FZ and HAZ, which are characterised by acicular ferrite and carbides. However, the behaviour in the presence of H is different. In the HAZ and FZ samples, a less pronounced reduction in toughness is observed (see J values in Table 6), attributable to a lower tendency for stress concentration and greater resistance to H diffusion. Consequently, despite being subjected to the same loading conditions and an aggressive environment, these zones show greater tolerance to HE than the BM. The significant decrease in fracture toughness observed in a hydrogenated environment is mainly due to the accumulation of H near the crack tip in the SENT samples. This accumulation compromises the plastic deformation capacity of the material and reduces the stress state and energy required for crack initiation and propagation. The J_{MAX} values obtained are in good agreement with those reported in previous studies [249] [250] [251]. In this experimental work, the value of J_{MAX} is reduced by approximately 40% for BM and 30% for HAZ and FZ. It is widely documented in the literature that fracture resistance decreases as the applied cathodic current increases [18] [202] [252]. Similar results have also been observed in tests conducted with H gas charging. In general, pipeline steels show a reduction in fracture resistance of between 40% and 60% in the presence of H gas [253]. In particular, X52 steel tested at 40 bar of H_2 showed a 40.9% reduction in the J parameter [254], while a 50% decrease was observed for X70 at 100 bar of H_2 [255] and 46% for X42 at 65 bar of H_2 [256].

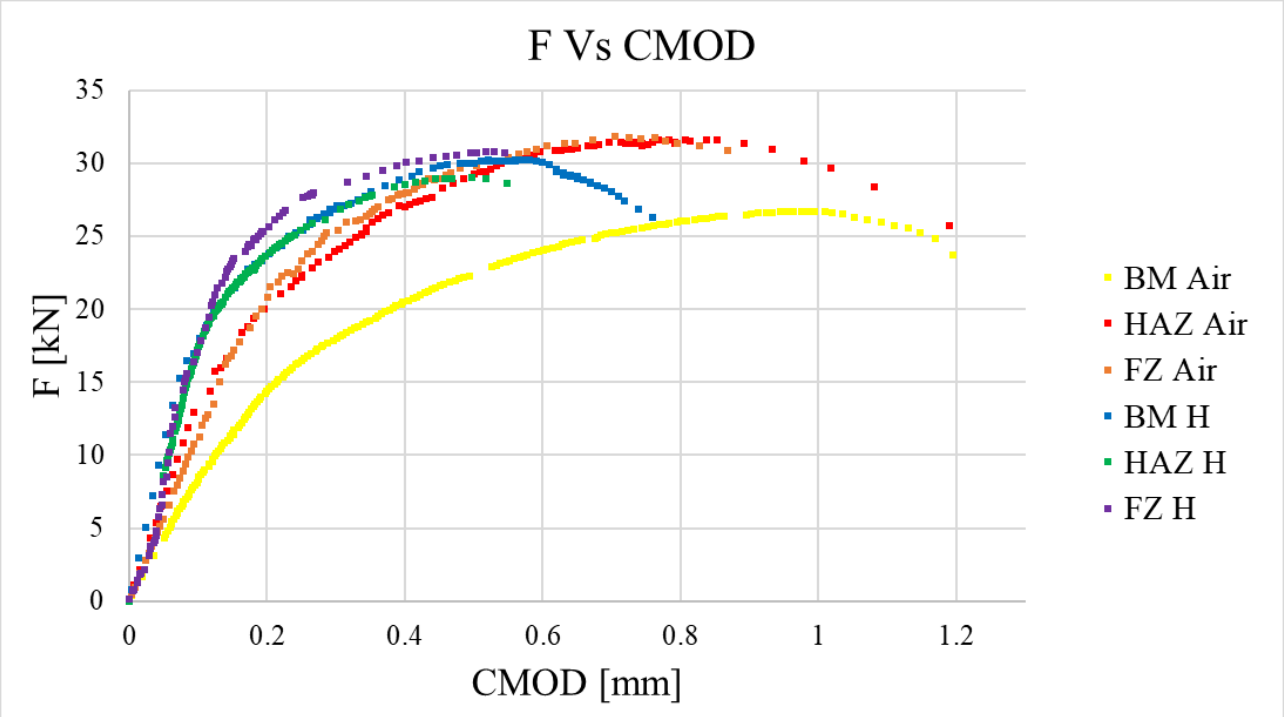

Figure 50-*Force vs CMOD curves for the SENT specimens tested.*

Table 17-*Values of J_{MAX} calculated for the SENT specimens tested.*

Specimen	$J_{MAX\ Air}$ [kJ/m^2]	$J_{MAX\ H}$ [kJ/m^2]	$J_{MAX\ H}/J_{MAX\ Air}$	H concentration [ppm]
BM	1233	727	0.590	1.20
HAZ	1094	751	0.686	1.08
FZ	1032	713	0.690	1.19

The fracture surfaces of the uncharged and charged specimens are shown in Figure 51. An overview of the fracture surface is shown in Figure 51a, while higher magnification SEM micrographs are presented in Figures 51b–f. The fatigue pre-fracture zone is clearly identifiable in the lower part of the specimen (Figure 51b). Starting from this region, a narrow band of stable crack propagation can be observed, which progressively evolves towards a final fracture zone characterised by rapid and unstable failure, as shown in the overview of the fracture surface (Figure 51a). High-magnification observation of the fracture surfaces of the samples tested in air reveals the presence of dimples typical of a ductile fracture mechanism (Figure 51c). In several cases, the dimples are nucleated around non-metallic inclusions, in particular silicon oxide particles, which act as preferential sites for fracture initiation (Figure 51d). In samples tested in the presence of H, the fracture surface shows a clearly distinct morphology between the fatigue pre-crack zone and the subsequent fracture region. In this intermediate area, characteristic ‘river’ patterns can be observed, indicative of a predominantly brittle transgranular fracture mechanism due to splitting (Figures 51e and 51f). This morphology is commonly associated with HE phenomena and confirms the role of H in promoting the transition from ductile to more brittle behaviour.

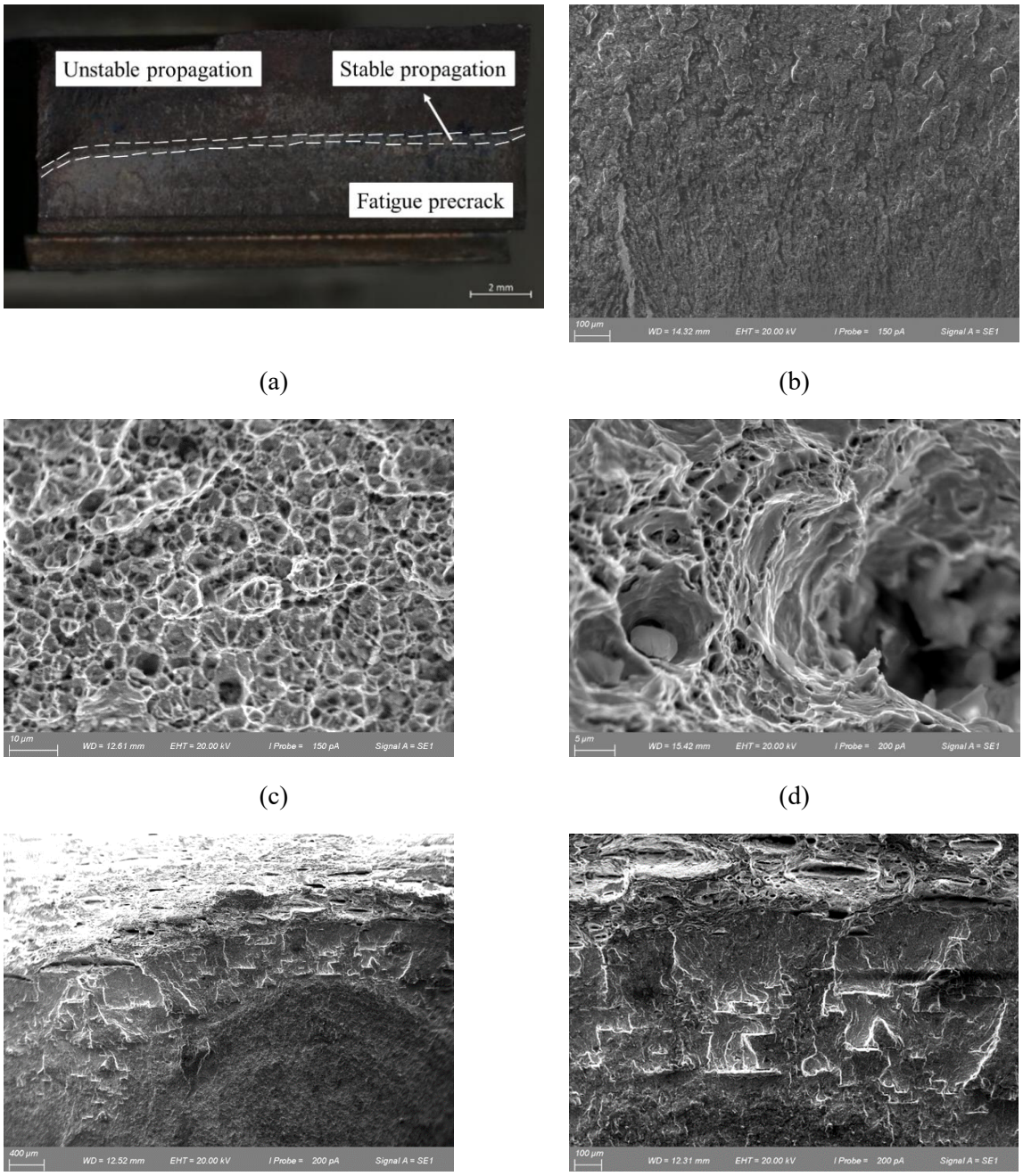

Figure 51-(a) *Image recorded at 5X with stereographic microscope in which the three different zones of the billing surface (BM) were highlighted.* (b) *Fatigue enhanced zone (BM).* (c) *Dimples in the stable propagation part (SENT with notch in FZ).* (d) *Microvacuum accreted around silicon oxide particles.* (e) *SENT with notch in HAZ charged with H. A brittle fracture section can be seen between the fatigue precrack zone and ductile fracture zone.* (f) *Cleavage planes in the stable propagation zone of a HAZ-notched SENT.*

The longitudinal micrographs of the samples, acquired using LOM, are shown in Figure 52. In general, three distinct regions can be identified along the crack path: the fatigue propagation zone, the stable propagation zone and the unstable propagation zone of the crack. The fatigue propagation

region is characterised by an almost linear and regular profile, while the subsequent stable propagation zone shows a more irregular profile, associated with evident plastic deformation of the material.

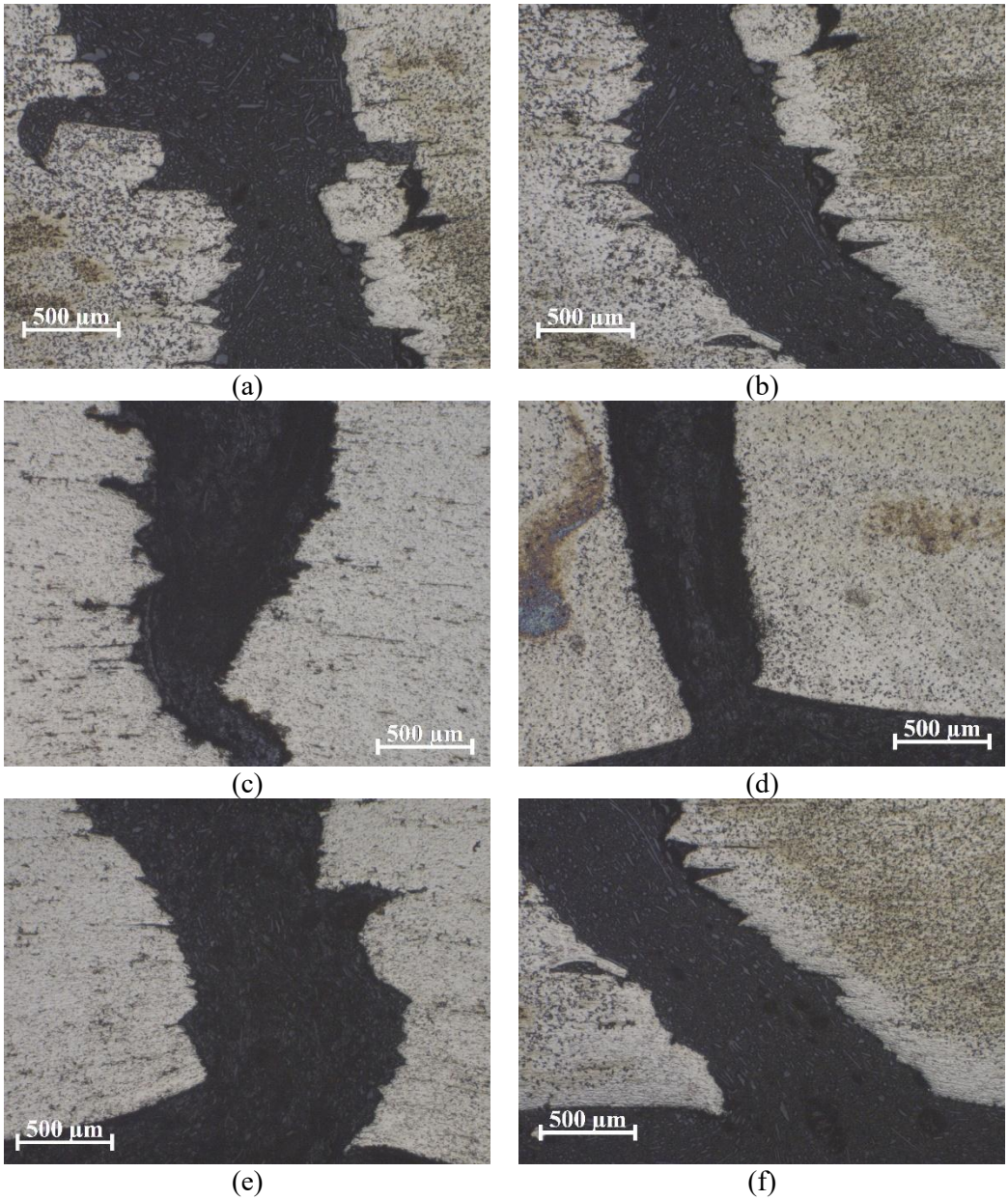

Figure 52-(a) *Transition between fatigue pre-crack and stable propagation in a HAZ specimen charged with H.* (b) *Transition between stable and unstable propagation zone of the previous specimen*. (c) *Overall view of the three zones in a BM specimen charged with H.* (d) *Crash failure zone of a ZF specimen tested in air*, (e) *HAZ in air and* (f) *HAZ in H.*

The final phase of unstable propagation, on the other hand, can be identified by a straight profile again, related to the rapid final failure of the specimen. The main nucleation sites of microvoids are located within the stable propagation zone, mainly associated with the presence of non-metallic inclusions, in particular manganese sulphides (MnS), which act as triggers for cavitation and the subsequent coalescence of voids. In a hydrogenated environment, the final fracture occurs along a

plane inclined at approximately 45° to the load axis and involves a significant portion of the material, as shown in Figure 52f. In contrast, in the samples tested in air, the area affected by the final failure is more limited and the fracture angle is less pronounced (Figure 52d), indicating a more gradual final failure process characterised by a lower propagation speed than that observed in the presence of H [257].

3.3.3 SENB Specimen-Compliance Method

The F/CMOD curves for the SENB BM samples tested in air and in electrolytic H are shown in Figure 53a, while the corresponding J-R curves are shown in Figure 53b. Figure 54 illustrates the correlation between the measured J_{IC} values and the diffusible H content in each sample. In the force-CMOD diagram (Figure 53a), samples with longer initial cracks have steeper curves due to a smaall starting ligament. H charged samples reach maximum load earlier, indicating reduced plastic deformation capacity at the crack tip. This premature yield suggests that H compromises local ductility, thereby accelerating the onset of failure. The J-R diagram (Figure 53b) shows that the air tested sample has greater resistance to crack propagation; in fact, it requires more energy to propagate the crack for the same length. As the concentration of H in the specimen increases, fracture resistance decreases, which is a clear sign of HE. At the same time, J_{IC} values decrease progressively as the concentration of diffusible H increases (Figure 54). This trend is consistent with the microstructure of the X52 steel used, as explained in section 3.3.2. The J_{IC} value in H decreases by up to 40% compared to tests carried out in air (Table 18). These results suggest that even low concentrations of H, close to 1 ppm, are sufficient to activate embrittlement mechanisms in this steel. However, the lower JIC value obtained is higher than the limit suggested by the ASME code (K_{IC} = 55 MPa·$m^{0.5}$/J_{IC} = 13 kJ/m^2) [179]. The fracture surfaces analysed by SEM show behaviour comparable to that described in section 3.3.2. The air tested sample is characterised by the presence of numerous dimples, while the others also show quasi-cleavage planes (Figures 55).

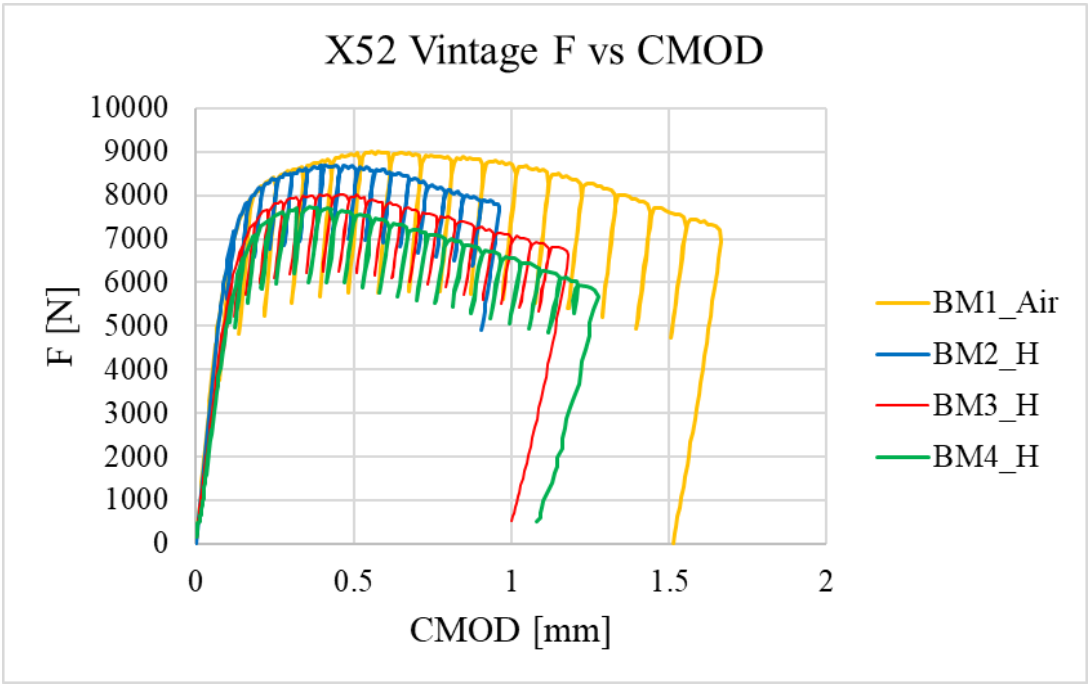

(a)

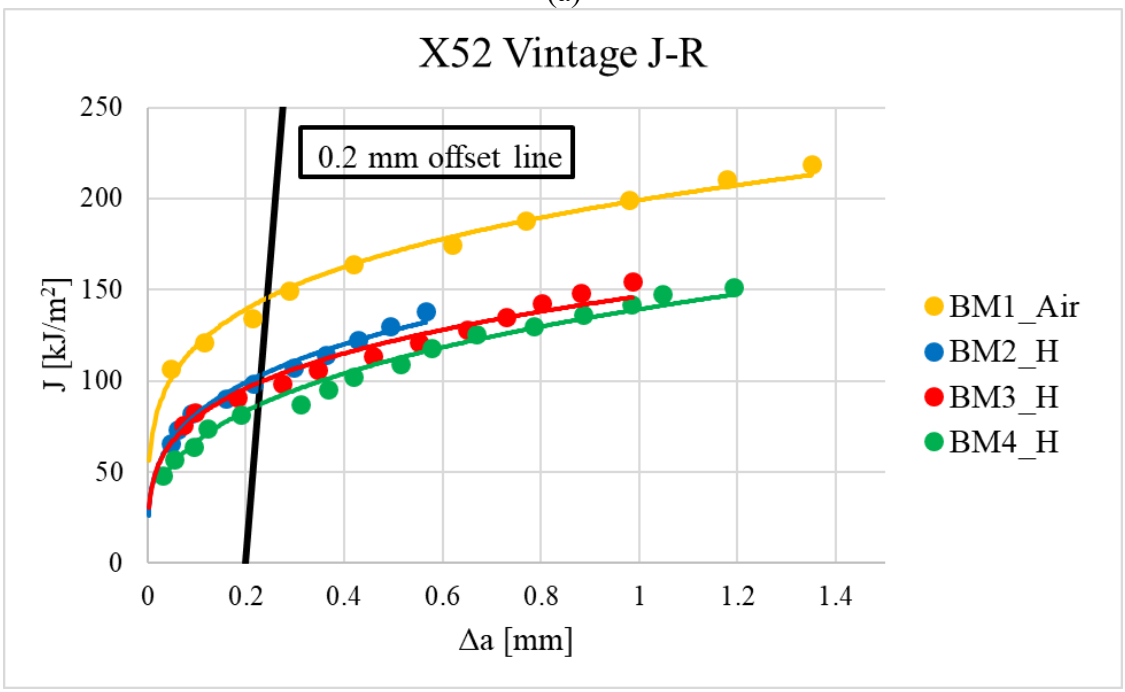

(b)

Figure 53-(a) *Force vs CMOD curves for the SENB specimens tested.* (b) *J-R curves elaborated from previous F vs CMOD curves.*

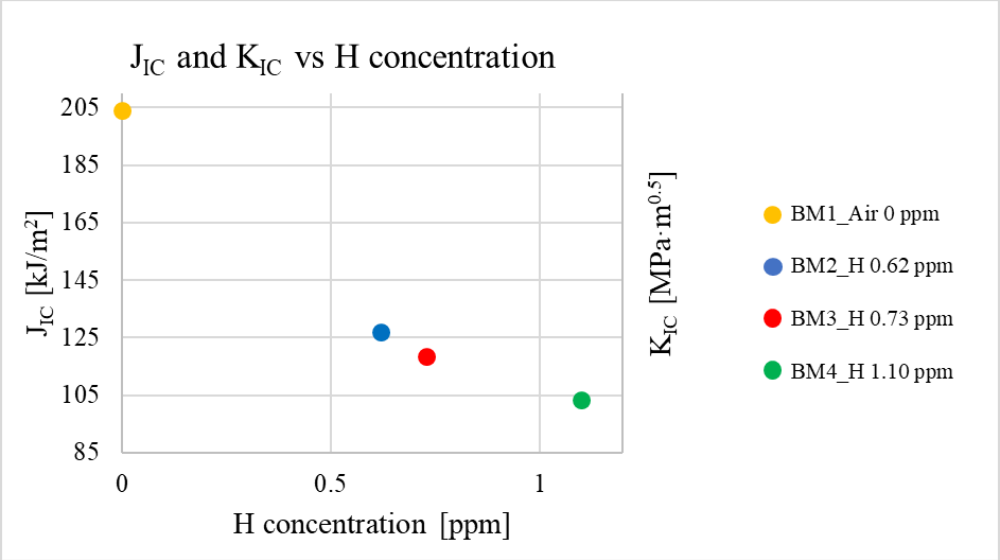

Figure 54- *Effect of H concentration on J_{IC} and K_{IC}.*

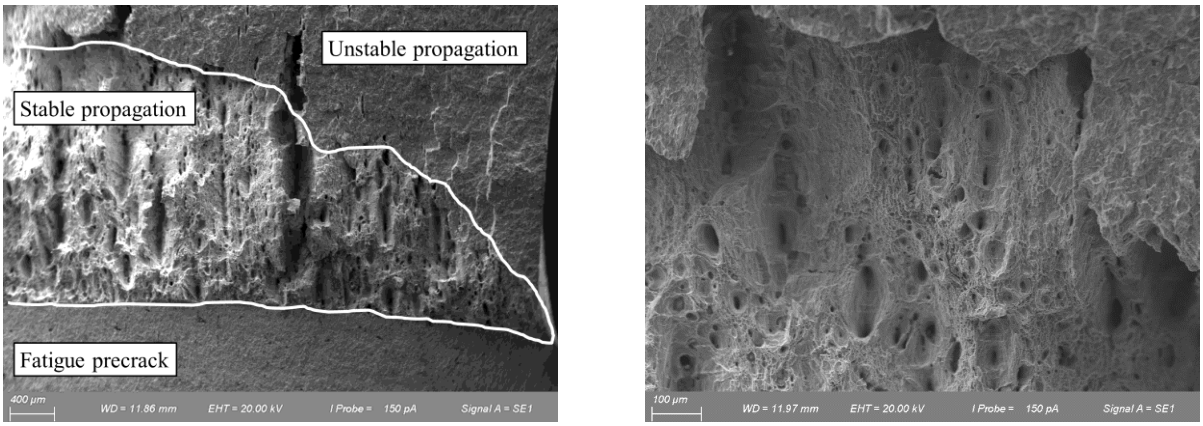

(a) (b)

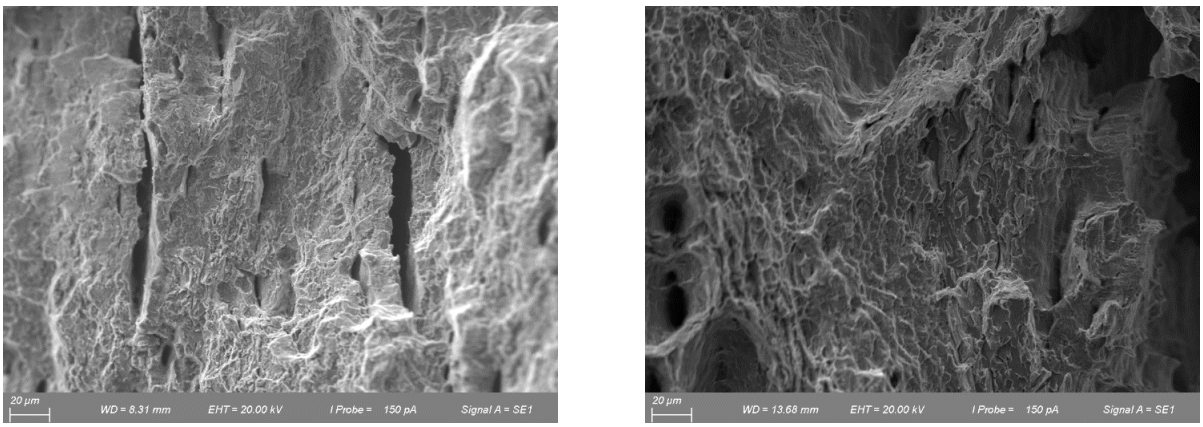

(c) (d)

Figure 55-(a) *General view BM1_Air specimen. The three different zones of which the fracture surface is composed are clearly visible.* (b) *Stable propagation zone of the BM1_Air specimen.* (c) *Stable propagation zone of the BM3_H specimen.* (d*) Stable propagation zone of specimen BM2_H.*

Table 18-*Relationship between $J_{Ic\ Air}$ and J_{IH}*

Specimen	$J_{IH}/J_{IC\ Air}$
BM2_H	0.70
BM3_H	0.68
BM4_H	0.59

The fracture surfaces of the air tested (a) and H cathodic (b) SENB specimens are shown in Figure 56. In both cases, fatigue pre-cracking is clearly visible at the root of the notch, followed by the fracture zone.

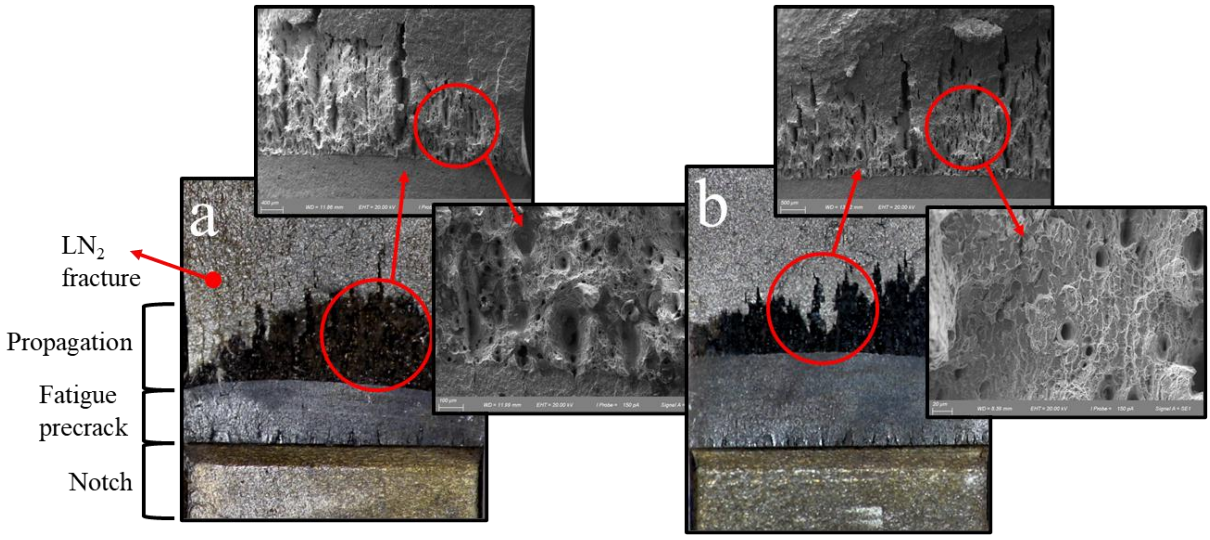

Figure 56-*SEM fractographic images of SENB specimens:* (a) *BM1_Air;* (b) *BM3_H*

In sample a, the fracture surface has a predominantly ductile morphology. The main area of crack propagation is characterised by well-defined dimples, a typical feature of ductile overload fracture. In contrast, the H tested sample (b) shows a distinctly different fracture morphology. In fact, high-magnification images reveal a mixed fracture composed of randomly disposed dimples in a brittle matrix. The longitudinal micrograph of the sample tested in air shows the stable propagation zone with an irregular morphology, marked by plastic deformation (Figure 57a). Within this area, microvoids were observed as fracture nucleation sites at the ends of elongated non-metallic inclusions. In the cathodic H charged samples, a different aspect of the crack propagation profile was observed: the crack is straight and changes its path along an inclined plane of approximately 45° and appears to be related to a lower local plastic deformation than the sample tested in air (Figure 57b).

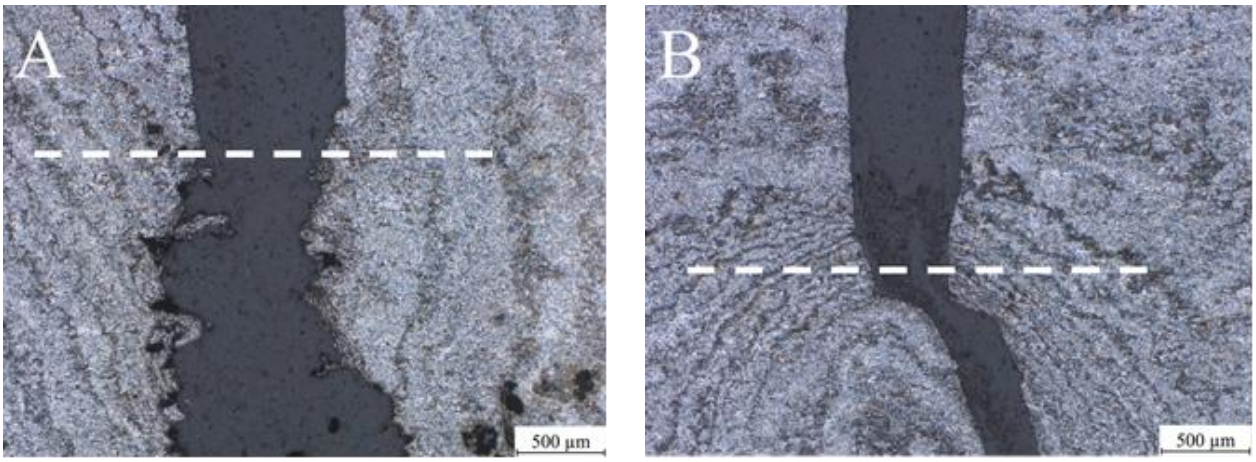

Figure 57–*Panel* A *(left): specimen BM1 air tested; panel* B *(right): specimen BM3 cathodic H tested. The white dashed lines indicate the zone were the fatigue precrack (on the top) ends and the stable crack propagation starts on each specimen.*

The F/CMOD curves for the FZ NP, HAZ NP and HAZ NQ samples tested in air and in electrolytic H are shown in Figure 57 a-c-e respectively, while the corresponding J-R curves are shown in Figure 57 b-d-f respectively. The FZ2 sample, tested in H environment, has lower J values than the air tested specimen FZ1 for the same Δa. The FZ3 sample suffered a sudden and pronounced loss of load capacity, resulting in a much flatter J-R curve than the other two samples. The fracture may have encountered a brittle microstructure along its propagation path, typical of welded joints, causing very rapid fracture propagation. Figure 59 shows the fracture surfaces after heat tinting of FZ1 and FZ3, marked A and B respectively, together with their SEM magnifications The fracture surface of the air tested specimen has a ductile morphology (Figure 59c), characterised by the presence of typical dimples. In contrast, in the H-tested material, dimples are mainly observed in the central region (Figure 59d), while quasi cleavage planes, characteristic of brittle fracture, appear on the edges (Figure 59e). The geometry of the NP notch in the HAZ specimens allows the crack to propagate on one side (B) in the HAZ and on the other in the FZ. This makes it possible to monitor two microstructures with a single specimen. For this reason, the crack propagation differs on specimen surface. Observations made with a stereomicroscope reveal that the region where the crack propagated most deeply corresponds to the FZ, which appears less coarse than the HAZ (Figure 60a-b). SEM observations show that the FZ is characterised by very fine dimples, within which globular oxides are incorporated (Figure 61a). In contrast, the HAZ has larger dimples and a lower concentration of oxides (Figure 61b). The behaviour in H environment is similar to that observed for the FZ series of samples: the two edges have a brittle appearance (Figure 62a-b), while the central region of the fracture surface remains ductile (Figure 62c). The percentage of HAZ calculated in accordance with ISO 15653 [233] for samples HAZ1, HAZ2 and HAZ3 is 80.70 %, 64.22 % and

61,85 %, respectively. The HAZ NQ samples provide clearer evidence of the effect of H. As shown in Figure 58f, H did not affect the material as severely as in the case of the FZ samples. However, fractographic examination reveals that the two edges of the fracture surface are embrittled, showing well-defined quasi-cleavage planes (Figure 63a-b).

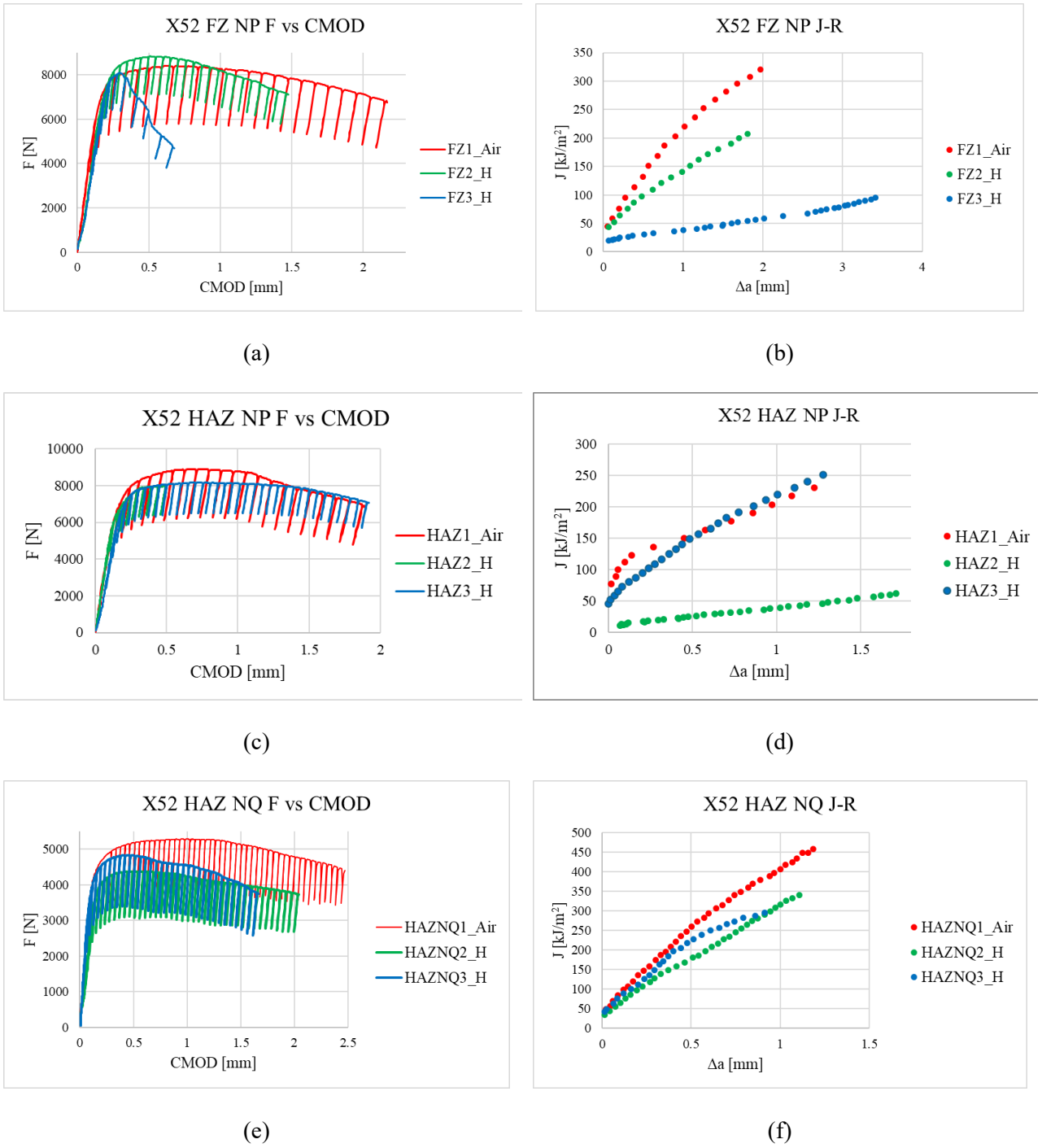

Figure 58-(a) *FZ specimens A* (a) *F vs CMOD curves and* (b) *J-R curves; HAZ NP specimens* (c) *F vs CMOD curves and* (d) *J-R curves; HAZ NQ specimens* (e) *F vs CMOD curves and* (f) *J-R curves.*

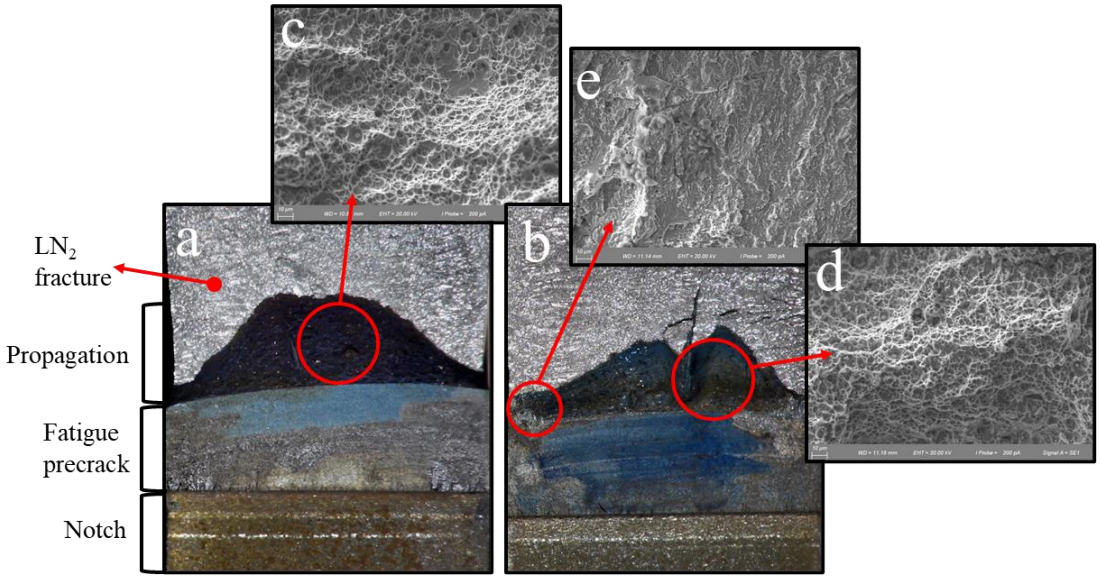

Figure 59-(a) *FZ1 air tested sample farcture surface;* (b) *FZ3 H tested.sample fracture surface; (c) dimples in FZ1 sample; (d) dimples in FZ3 sample; (e) embrittled edge in FZ3 sample.*

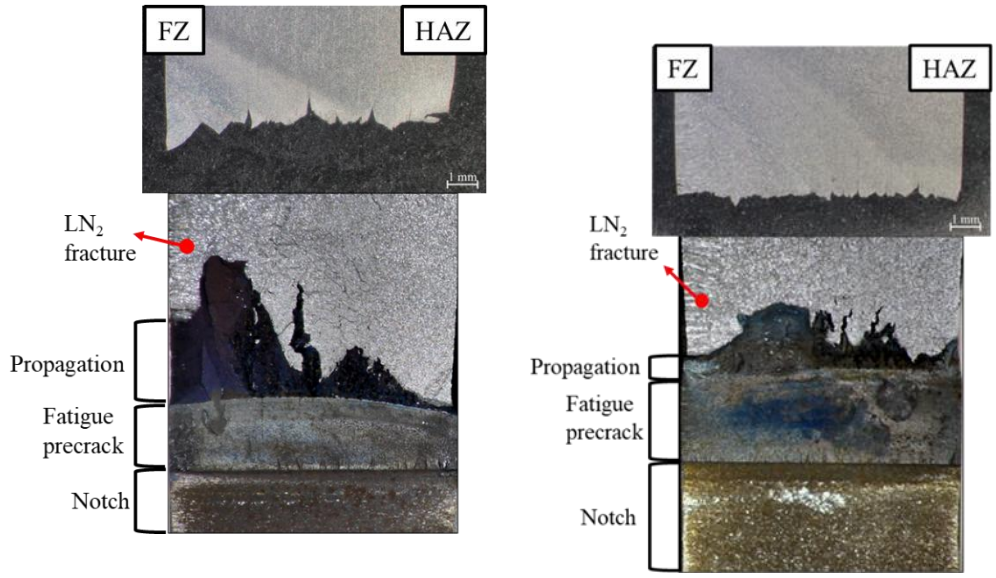

(a) (b)

Figure 60-*(a) HAZ1 NP air tested specimen and (b) HAZ3 NP H tested specimen with the macrograph on top and the fracture surface below.*

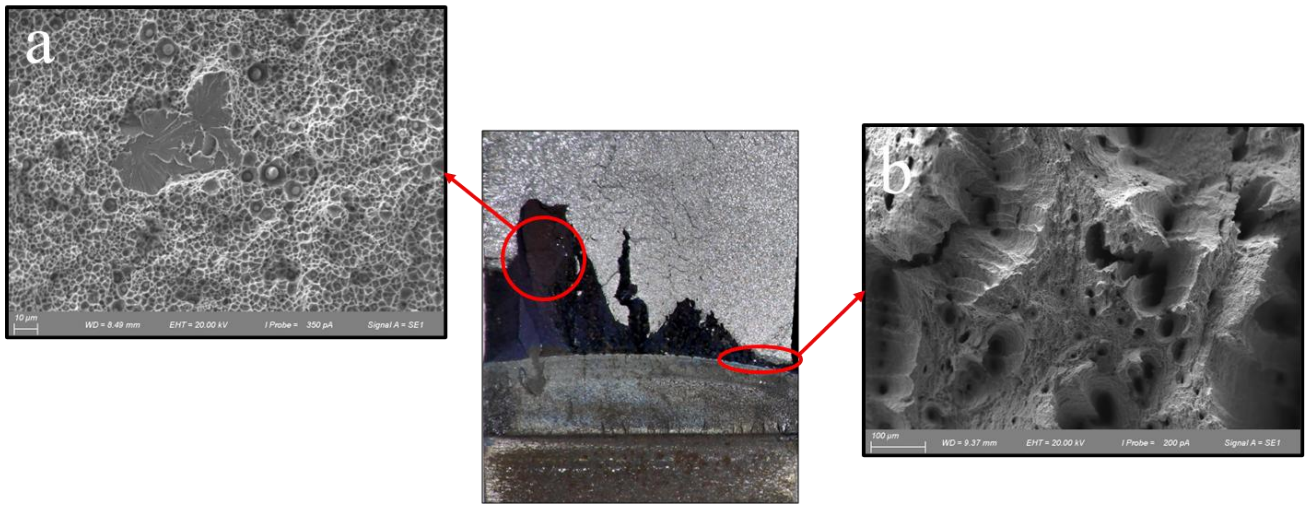

Figure 61-(a) *FZ1 NP Air tested specimen fracture surface;* (b) *fine dimples in FZ region;* (c) *coarse dimples in HAZ region.*

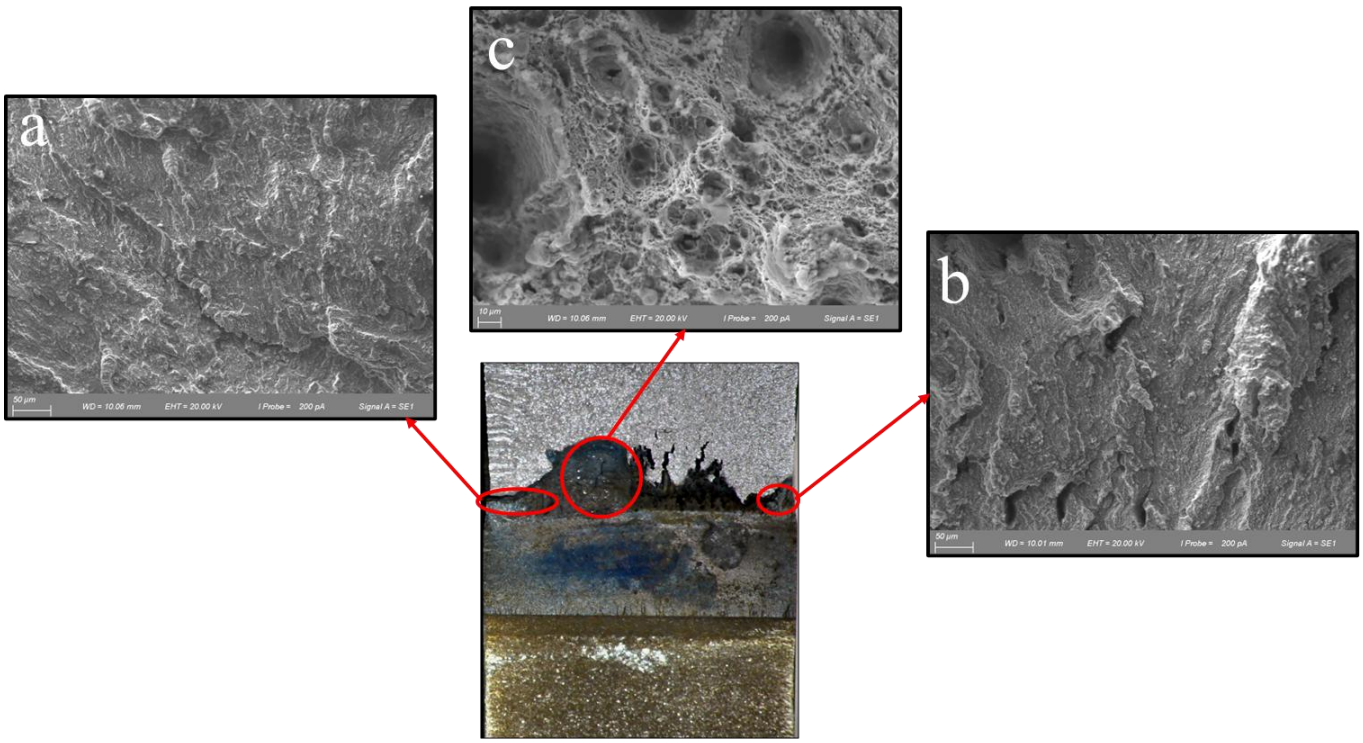

Figure 62-(a) *FZ2 NP H tested specimen fracture surface;* (b)-(d) *quasi cleavage planes in the edges;* (c) *dimples in the central region.*

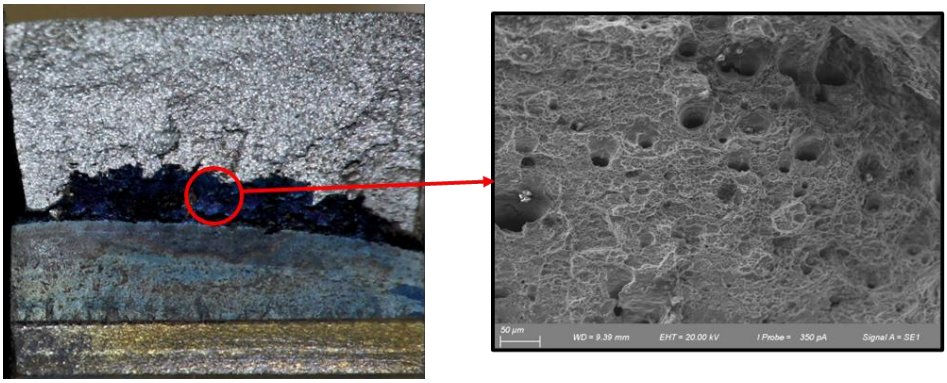

(a)

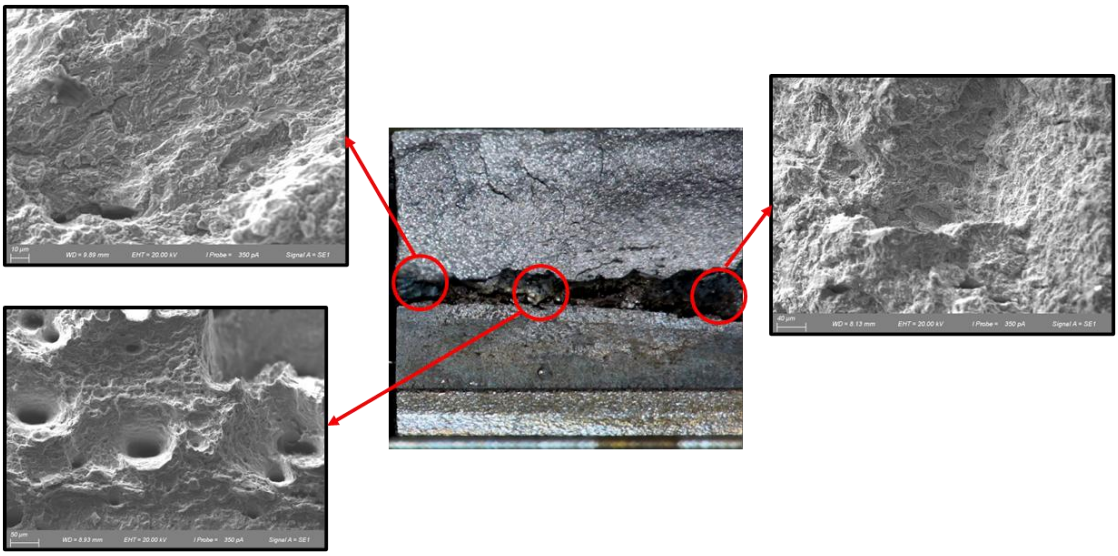

(b)

Figure 63-(a) *HAZNQ1 air tested specimen fracture surface and SEM magnification;* (b) *HAZNQ3 H tested specimen fracture surface and SEM magnification. Note that in the central region there are coarse dimples like HAZ NP specimen and the edges are embrittled with quasi cleavage planes.*

In Figure 64, the behavior of BM, HAZ, and FZ in cathodic H is presented. In general, embrittlement was higher in the weld than in the BM. Often the welding process often introduces residual stresses or flaws that may compromise the outcome of the test regardless of the effect of H. This led to significant scattering of the results for FZ and HAZ. The blunting line, the 0.2 mm offset line and ASME B31.12 limit (13.0 kJ/m^2) were plotted. The values of J_0 (value of J at the blunting line) and $J_{0.2}$ (value of J at the offset line) are in the range between 0.4-48.3 kJ/m² and 18.0-103.3 kJ/m² respectively. This implies that more detailed characterisation is required for FZ and HAZ, as the J_0 values are below the limit required by ASME B31.12.

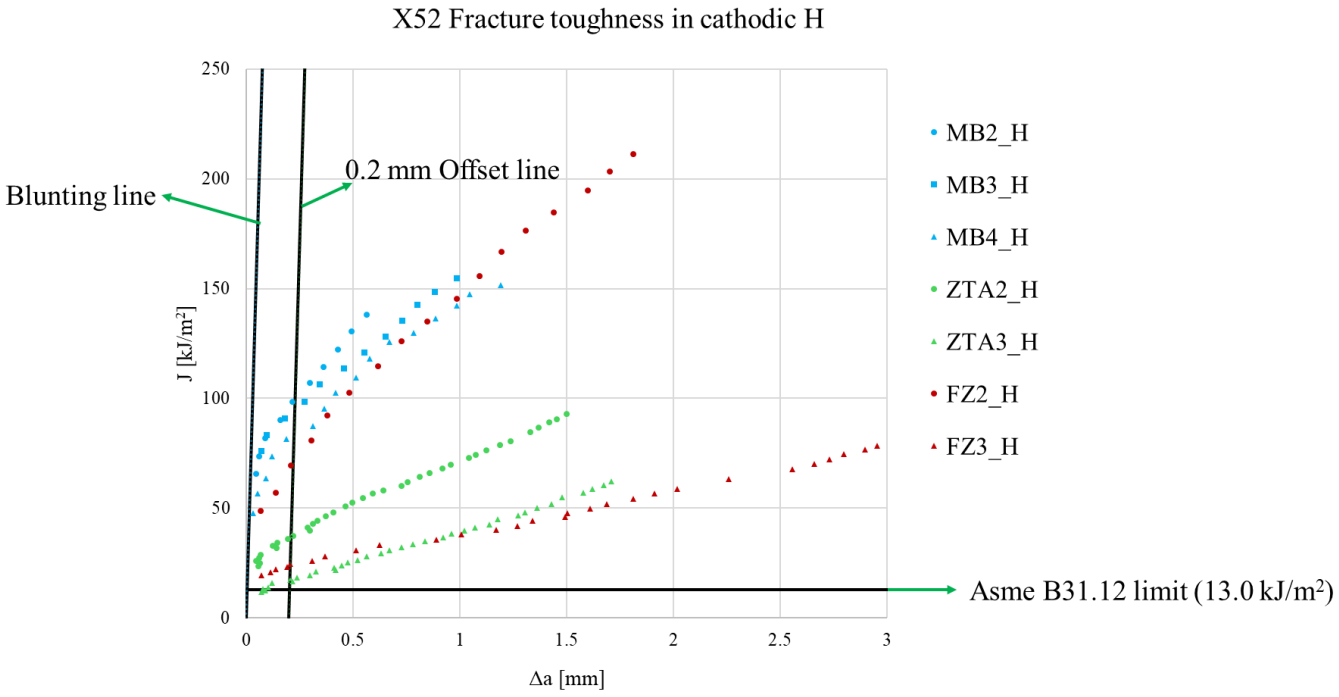

Figure 64-*J–R curves for BM, HAZ, and FZ in H environment, including indication of the ASME B31.12 limit.*

3.3.4 Permeation test with DS cell

A total of 7 BM, 7 W, 2 5S and 2 10S samples were tested. The most significant results are shown in Figure 65. The first part is the discharge phase, where the current decreases to close to 0. After 5400 seconds, the charge phase begins until a steady-state current value is reached: this is the first transient. At t = 10800 s, the second discharge begins, lasting 3.5 hours, before the test is completed with the second transient. Quantitative analysis of the permeation parameters shows a clear relationship between D_{eff}, C_0 and N_T (Table 19).

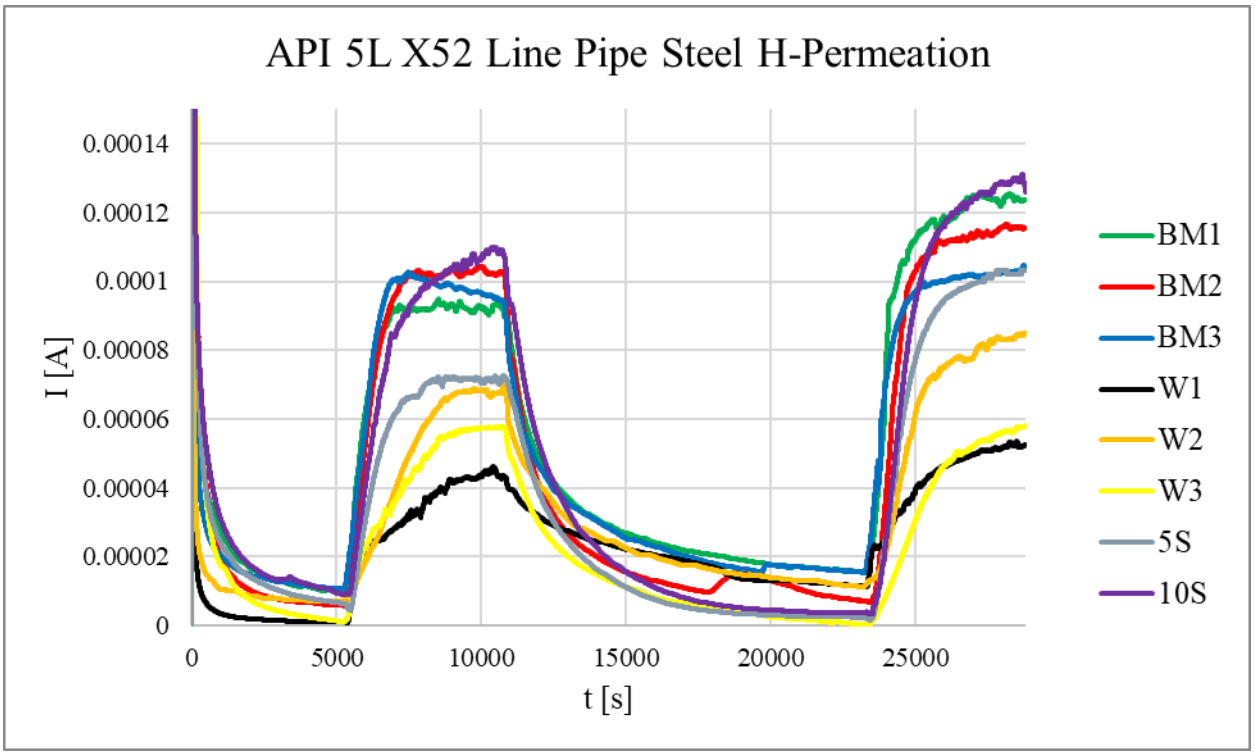

Figure 65-*Current versus time graph for selected X52 samples.*

Table 19-*Effective diffusivity, subsurface concentration and trap density of BM, W, 5S and 10S samples.*

	$D_{eff\,1}$ [cm^2/s]	$D_{eff\,2}$ [cm^2/s]	C_0 [ppm]	N_T [$n°/cm^3$]
BM1	$2.36 \cdot 10^{-6}$	$2.18 \cdot 10^{-6}$	2.64	$2.22 \cdot 10^{20}$
BM2	$1.78 \cdot 10^{-6}$	$1.44 \cdot 10^{-6}$	4.01	$4.49 \cdot 10^{20}$
BM3	$1.98 \cdot 10^{-6}$	$2.48 \cdot 10^{-6}$	3.37	$3.39 \cdot 10^{20}$
W1	$9.10 \cdot 10^{-7}$	$9.71 \cdot 10^{-7}$	3.49	$7.71 \cdot 10^{20}$
W2	$7.31 \cdot 10^{-7}$	$9.34 \cdot 10^{-7}$	6.23	$1.71 \cdot 10^{21}$
W3	$8.87 \cdot 10^{-7}$	$7.88 \cdot 10^{-7}$	4.74	$1.07 \cdot 10^{21}$
5S	$1.55 \cdot 10^{-6}$	$1.22 \cdot 10^{-6}$	3.22	$4.14 \cdot 10^{20}$
10S	$1.46 \cdot 10^{-6}$	$1.13 \cdot 10^{-6}$	4.53	$6.20 \cdot 10^{20}$

In particular, the W samples show lower diffusivity and higher trap density than the other samples. This indicates a greater ability of the weld microstructure to trap H, thus reducing its mobility through the material. This behaviour is consistent with the presence of more complex and fine microstructures in the weld metal than in the BM, such as bainite and acicular ferrite. The pearlite is the main site of H trapping. These sites are located at the interface between ferrite and cementite. Therefore, the high number of fine cementite interfaces in a bainitic structure such as those observed in the weld acts as a strong inhibitor of H diffusion [70]. The welding process also reduces grain size. It is reported in the literature that H permeation decreases as grain size decreases [82]. Pre-deformed specimens have intermediate values of diffusivity and trap density. As the level of pre-deformation increases, an increase in C_0 and N_T is observed. This effect can be attributed to the higher density of dislocations and crystalline defects generated by plastic deformation, which act as H trapping sites. In fact, it is

known that the concentration of reversible traps, such as dislocations, increases more than that of irreversible traps with increasing plastic deformation [258]. On the other side, BM exhibits the highest diffusivity and lowest trap density, making it less effective at retaining H within its microstructure. These results are certainly predictable from a qualitative point of view; however, their quantification for a specific joint is particularly significant. Observations of the surfaces of the specimens after the permeation tests provide further information on the behaviour of H (Figures 66 and 67).

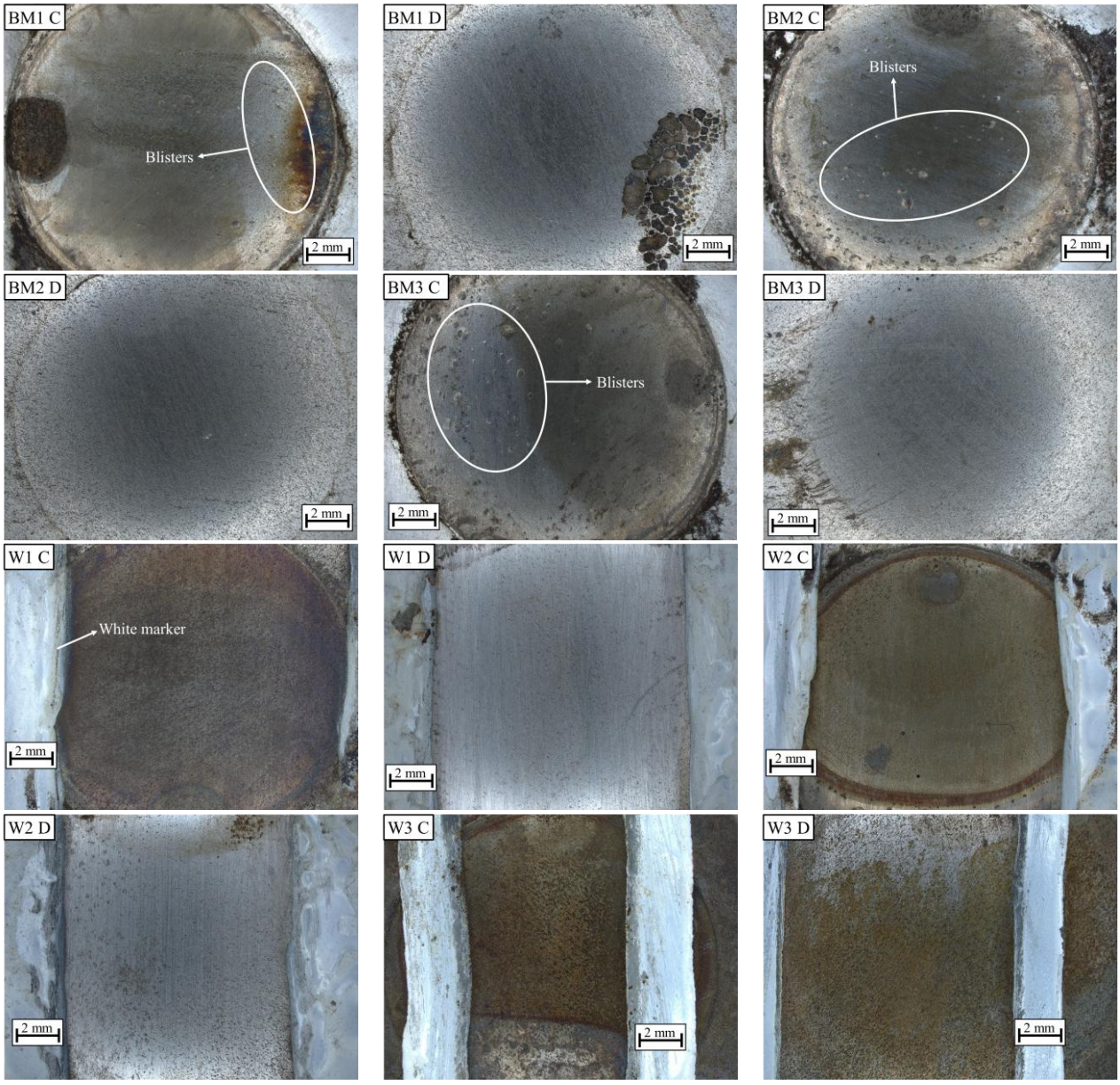

Figure 66-*Charging (C) and discharging (D) side of BM and W specimens.*

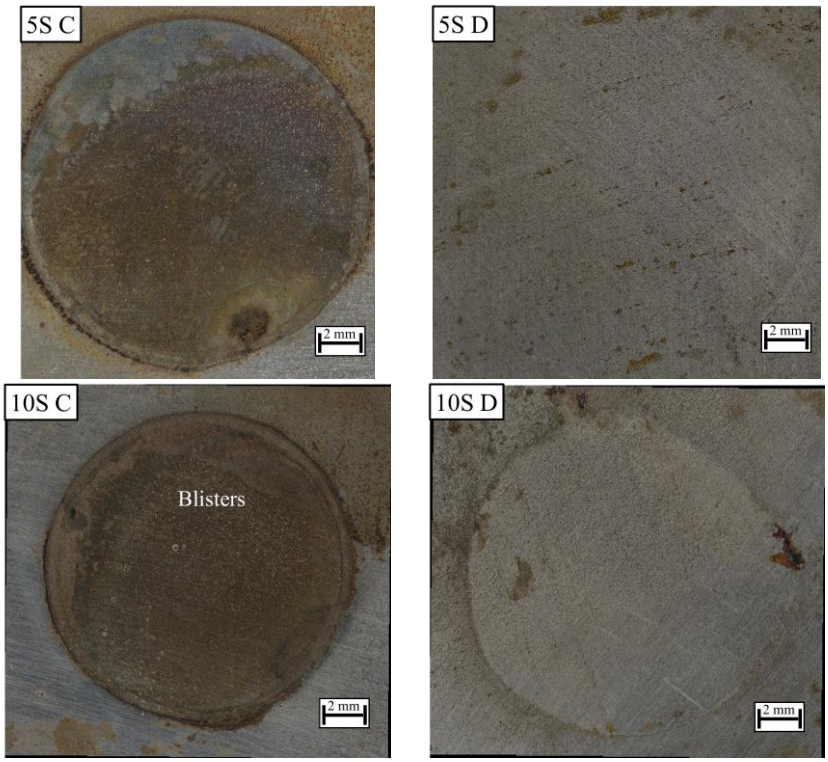

Figure 67-*Charging (C) and discharging (D) side of prestressed specimens.*

The BM shows marked blistering, particularly on the loading side. This phenomenon can be attributed to the limited number of traps available, which causes H to accumulate near the surface rather than being trapped within the volume of the material. In the pre-deformed specimens, blistering is less pronounced, suggesting that the increase in trapping sites promotes a more uniform distribution of H in the material. However, in the 10% pre-deformed specimen, locally more prominent bubbles are observed, indicating that higher levels of deformation can still lead to critical H concentrations in certain areas. The behaviour of the welded material is markedly different from the other specimens. In this case, blistering is minimal or absent, while signs of localised corrosion are observed. This result is consistent with the high trap density and low diffusivity measured, which indicate a strong tendency for H to be trapped within the microstructure of the welded metal. In these samples, H enters perpendicular to the rolling direction. However, it has been reported that if the opposite occurs, D_{eff} increases by an order of magnitude [259] [260]. In general, the values of D_{eff}, C_0 and N_T are comparable to those reported in the literature for this family of steels [72] [261] [262] [263] [264].

3.3.5 Permeation test with novel set up

In the new permeation setup, H detection is performed by a QMS instead of the oxidation compartment of the traditional DS cell. This hybrid configuration allows the electrolytic charging of H on the inlet side of the metal sample and its detection in the gas phase on the outlet side under high

vacuum. In order to understand the signal provided by the QMS to be interpreted in quantitative terms, a calibration leak, i.e., a source of H_2 with a known and constant flow rate, must be introduced into the system. When the calibration leak is opened, the known flow of H generates a signal that can be measured by the QMS in the form of partial pressure. By recording the pressure value corresponding to the known flow rate, it is possible to determine a calibration factor that relates the instrumental signal to the actual flow of H. This factor allows the experimental permeation signal, $P_H(t)$, to be converted into an H flow, $J_H(t)$. In the designed system, the calibration leak would have been connected to the two-way fitting provided for the pressure sensor and for the leak itself. The presence of the gate valve upstream of the QMS would also have allowed the spectrometer to be isolated during any verification operations or in the event of abnormal flows, preserving its integrity. For reasons related to the thesis delivery schedule, it was not possible to proceed with the installation of the calibration leak or to perform the quantitative calibration of the system. However, in order to verify the tightness of the instrumentation and the reliability of the assembly under vacuum conditions, a preliminary test was performed using a BM sample (Figure 68).

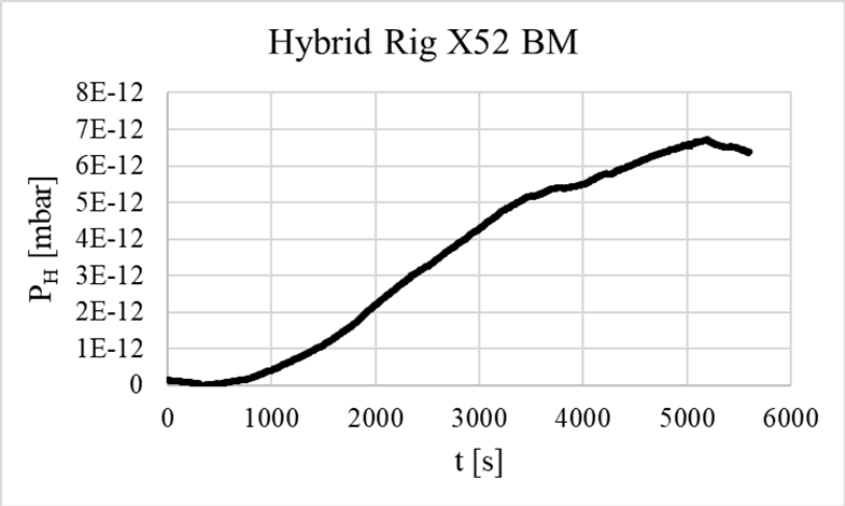

Figure 68-*First test with the hybrid rig*

The signal remains close to the bottom of the instrument scale, indicating stable vacuum conditions and no leaks in the system. Close to t = 1000, the partial pressure of H_2 increases, reaching values of the order of $6\text{-}7 \cdot 10^{-12}$ mbar. This trend is consistent with the start of the H permeation process through the metal sample. Finally, the curve shows a slowdown in the increase and a tendency to stabilize, consistent with the approach to steady state. Therefore, although the test is only qualitative, it confirms the successful assembly of the machine, the sensitivity of the QMS to changes in H flow, and the maintenance of ultra-high vacuum. This type of hybrid rig can also be clearly manufactured with an autoclave instead of an electrochemical cell to study the permeation of H gas.

4. Conclusions and future perspectives

This doctoral research project systematically addressed the study of the effect of electrochemically introduced H on vintage API 5L X52 steel with the aim of assessing its suitability for service with a view to possible repurposing for H transport. Interest in this topic is part of the broader scenario of energy transition, which requires the progressive decarbonisation of energy systems and identifies green H as a strategic vector for the storage and transport of renewable energy. The results obtained allow the following conclusions to be drawn:

- Role of microstructure on H charging.
  The refinement of electrochemical parameters has made it possible to identify effective charging conditions for introducing H into the material in a reproducible and controlled manner. In particular, a solution composed of 0.01 mol/L H_2SO_4 and 2.00 g/L TU with a current density of J = -10 mA/cm^2 proved effective on this material in introducing H without undesirable side effects such as blistering or corrosion. The behaviour towards H was not uniform between the BM, HAZ and FZ. The presence of elongated manganese sulphides and numerous ferrite/pearlite interfaces allow the BM to absorb more H than expected. However, the FZ absorbs the greatest amount for each selected time interval.
- Effect of H on mechanical properties.
  Slow strain rate and fracture mechanics tests showed a reduction in ductility and toughness in the presence of H, with more brittle fracture modes than in air. H crack formation follows a HELP mechanism at nucleation and an HEDE mechanism during propagation. The H susceptibility of the WM was found to be lower than that of the BM in fracture mechanics tests. Although the FZ has lower toughness than the BM in air, it was able to absorb a greater amount of H, with a less detrimental effect on its toughness when tested in a hydrogenated environment. This suggests that, although the weld is harder and typically more brittle, its microstructure is better able to trap H, limiting its diffusion and mitigating the impact of HE. Similar behaviour was observed in slow strain rate tests performed prior to this experimental work, where the welded specimens broke in the BM. In fracture mechanics tests, the effect of H is also recognisable in the fracture surfaces observed with SEM. In fact, compared to the uncharged specimens, it shows a band of planes of quasi cleavage associated with brittle fracture. In the longitudinal micrographs, on the other hand, the propagation zone during the test in the hydrogenated specimens deviates by 45° from the upper part of the fracture. In tests with SENB specimens, despite the wide range covered by the curves obtained, there is a high scattering of results regarding welding. This can be attributed to the duration of the test and

therefore the H charging, the geometry of the specimen, the position of the notch and the geometry of the weld. For this reason, further tests are necessary to confirm the trend obtained. In BM, it was observed that the J_{IH} value decreases as the concentration of loaded H increases, as expected.

- Role of welding and stress state on H permeation.
  Tests with the Devanathan–Stachurski cell made it possible to determine key parameters such as diffusion coefficient, sub-surface H concentration and H trap concentration. It was confirmed that the fine microstructure and lattice defects induced by welding slow down the flow of H due to the formation of H traps. Similarly, plastic deformation introduces new H traps into the microstructure, in particular dislocations, which slow down its path. These traps allow more H to be stored in the subsurface layers. On the other hand, the BM allows faster diffusion, but the microstructure cannot handle the large amount of electrolytic H and therefore develops blistering on the charging side.
- Development of an innovative set-up to study H permeation. The new set-up introduces the novelty of detecting H using a quadrupole mass spectrometer rather than an oxidative electrolytic cell. This allows direct measurement of the H flow without the need to palladium-plate the discharge side of the specimen and is immune to current interferences. An initial qualitative test was performed with a BM specimen, confirming the success of the assembly.

Overall, the results indicate that vintage API 5L X52 steel may exhibit a non-negligible susceptibility to HE, especially at welds and in the presence of stress states. However, there are no elements that would rule out the possibility of repurposing this pipeline (the J_{IC} values for BM are higher than the limit imposed by the ASME B31.12 code), provided that:

- case-by-case assessments are carried out, considering chemical composition, microstructure and state of preservation;
- operating limits are defined in terms of pressure and percentage of H in the mixture;
- appropriate monitoring and inspection protocols are implemented;
- a regulatory code is developed and implemented that suggests specific types of mechanical tests for monitoring H and safety coefficients beyond which the use of the pipeline is unsafe.

Considering the results achieved the following lines of development are outlined:

- Extension of the study to high-pressure gas charging, in order to reproduce operating conditions more realistically for both mechanical testing and permeation testing.

- Analysis of steels of different grades and years of manufacture, in order to build a comparative database representative of the national network.
- Study of the effect of H_2/CH_4 blending, in increasing percentages, to identify operational safety thresholds and because the experiment will begin by mixing H with NG and then move on to 100% H.
- Integration of permeation tests and advanced microanalytical techniques (e.g. EBSD, TEM,) to quantitatively correlate microstructure, trap density and mechanical response. These techniques make it possible to identify and quantify the types of traps.
- Development of an equation that correlates electrolytic charge with gas charge. This would allow mechanical tests to be performed in an electrolytic environment, making them less expensive and safer, and then converting the result into a gas charge.

This work has contributed to expanding the understanding of the interaction between H and pipeline steels, providing experimental data useful for assessing their reliability within the context of the energy transition. A thorough understanding of diffusion, trapping, and embrittlement phenomena represents an essential step to ensure safety, sustainability, and competitiveness in a future energy system in which H plays a central role. However, the realization of an energy scenario consistent with international climate objectives does not depend solely on technological progress. The scientific knowledge required to understand the impact of CO_2 emissions on the climate system has been consolidated for decades, and historical documentation has shown that these risks were already known within major oil industry companies as early as the second half of the twentieth century [265] [266]. Despite this awareness, the industrial and communication strategies adopted over time were not always oriented toward the timely mitigation of the problem, thereby contributing to delays in coordinated global action. In light of this historical responsibility and the substantial profits accumulated over decades by the use of fossil fuels, it appears reasonable that the main actors in the traditional energy sector should contribute to financing the ecological transition. A significant economic contribution on their part would not only represent a redistributive mechanism, but also a sign of accountability towards future generations. Ultimately, the challenge is no longer exclusively technological or scientific: in fact solutions for the production, transport, and utilization of H are already at an advanced stage of development. The central issue is political, economic, and social in nature. How much are governments willing to invest in a structural transformation of the energy system? To what extent are societies prepared to reconsider long-established consumption patterns and economic priorities? The success of the ecological transition will depend on the collective ability to align investments, regulations, industrial strategies, and lifestyles with a clear long-term vision,

while recognising that action is required immediately. Within this framework, research on materials and on the safe integration of H into existing infrastructures must continue in order to foster a deep-rooted transformation of the global energy development model.

Bibliographic References

[1] Shang Y, Han D, Gozgor G, Mahalik MK, Sahoo BM. The impact of climate policy uncertainty on renewable and non-renewable energy demand in the United States. Renewable Energy, 197, 2022, 654-667. https://doi.org/10.1016/j.renene.2022.07.159

[2] Ye L. The effect of climate news risk on uncertainties. Technological Forecasting and Social Change, 178, 2022, 121586. https://doi.org/10.1016/j.techfore.2022.121586

[3] Arrhenius S. On the Influence of Carbonic Acid in the Air upon the Temperature of the Ground. Philosophical Magazine and Journal of Science, 41, 1896, 237-276.

[4] Callendar GS. The artificial production of carbon dioxide and its influence on temperature. Quarterly Journal of the Royal Meteorological Society, 64, 1938, 223-240. https://doi.org/10.1002/qj.49706427503

[5] Plass GN, Fleming JR, Schimdt G. Carbon Dioxide and the Climate. American Scientist, 98 1959, 58-62.

[6] https://keelingcurve.ucsd.edu/ [accessed july 2025]

[7] https://www.bafu.admin.ch/bafu/it/home/temi/clima/info-specialisti/clima--affari-internazionali/politica-climatica-internazionale--convenzione-sul-clima.html [accessed july 2025]

[8] https://unfccc.int/resource/docs/convkp/kpeng.pdf [accessed july 2025]

[9] Official Journal of the European Union of 19/10/2016

[10] Olabi AG, Abdelkareem MA. Renewable energy and climate change. Renewable and Sustainable Energy Reviews, 158, 2022, 112111. https://doi.org/10.1016/j.rser.2022.112111

[11] Sen S, Ganguly S. Opportunities, barriers and issues with renewable energy development – A discussion. Renewable and Sustainable Energy Reviews, 69, 2017, 1170-1181. https://doi.org/10.1016/j.rser.2016.09.137

[12] Abraham KM. Prospects and Limits of Energy Storage in Batteries. The Journal of Physical Chemistry Letters. 2015 doi: 10.1021/jz5026273

[13] Nitta N, Wu F, Lee JT, Yushin G. Li-ion battery materials: present and future. Materials Today, 18, 2015, 252-264. https://doi.org/10.1016/j.mattod.2014.10.040

[14] Climate Change Committee, Hydrogen in a Low-carbon Economy. https://www.theccc.org.uk/publication/hydrogen-in-a-low-carbon-economy/; 2018 [acessed july 2025]

[15] Gotz M, Lefebvre J, Mors F, McDaniel Koch A, Graf F, Bajohr S, Reimert R, Kolb T. Renewable Power-to-Gas: a technological and economic review, Renew. Energy 85 (2016) 1371–1390, https://doi.org/10.1016/j.renene.2015.07.066

[16] EA. The Future of hydrogen, Seizing Today's Opportunities, Int Energy Agency, 2019. https://www.iea.org/reports/the-future-of-hydrogen. [accessed july 2025]

[17] CER European Union Agency for the Cooperation of Energy Regulators Gas factsheet https://www.acer.europa.eu/gas-factsheet [accessed july 2025].

[18] Chatzidouros EV, Papazoglou VJ, Tsiourva TE, Pantelis DI. Hydrogen effect on fracture toughness of pipeline steel welds, with in situ hydrogen charging, Int. J. Hydrogen Energy 36 (2011) 12626–12643, https://doi.org/10.1016/j.ijhydene.2011.06.140.

[19] Wu X, Zhang H, Yang M, Jia W, Qiu y, Lan L. From the perspective of new technology of blending hydrogen into natural gas pipelines transmission: Mechanism, experimental study, and suggestions for further work of hydrogen embrittlement in high-strength pipeline steels. International Journal of Hydrogen Energy. 47 (2022) 8071-8090. https://doi.org/10.1016/j.ijhydene.2021.12.108

[20] Cristello JB, Yang JM, Hugo R, Lee Y, Park SS. Feasibility analysis of blending hydrogen into natural gas networks. International Journal of Hydrogen Energy. 48 (2023) 17605-17629.

[21] D.A. Crowl, Y. Jo, The hazard and risks of hydrogen, J. Loss Prev. Process. Ind. 20 (2007) 158–164, https://doi.org/10.1016/j.jlp.2007.02.002.

[22] IEA, Global Hydrogen Review 2021, International Energy Agency, 2021. https://www.iea.org/reports/global-hydrogen-review-2021 [accessed july 2025].

[23] Shipilov S. Stress Corrosion Cracking and Corrosion Fatigue: A Record of Progress, 1873-1973. In book: Environment-Induced Cracking of Materials: Chemistry, Mechanics and Mechanisms., Edited by S.A. Shipilov, R.H. Jones, J.M. Olive, and R.B. Rebak.Chapter: 9Publisher: Elsevier, Amsterdam

[24] Johnson WH. On some remarkable changes produced in iron and steel by the action of hydrogen and acids, Proceedings of the Royal Society of London, vol. 23, p. 168, (1874).

[25] Oriani, R.A., Whitney Award Lecture—1987: Hydrogen—The Versatile Embrittler. Corrosion, 1987. 43: p. 390-397.

[26] Cotterill, P., The hydrogen embrittlement of metals. Progress in Materials Science, 1961. 9(4): p. 205-301.

[27] Myers, S.M., et al., Hydrogen interactions with defects in crystalline solids. Reviews of Modern Physics, 1992. 64(2): p. 559-617
[28] Arniella V, Zafra A, Álvarez G, Belzunce J, Rodríguez C. Comparative study of embrittlement of quenched and tempered steels in hydrogen environments. International Journal of Hydrogen Energy, 2022. 47(38) 17056-17068.
[29] Walter RJ, Jewett RP, Chandler WT. On the mechanism of hydrogen-environment embrittlement of iron- and nickel-base alloys, Materials Science and Engineering, 1970, 5, 99–110 doi: 10.1016/0025-5416(70)90039-X.
[30] De Marco M, Ferrari E, Zabbia M, L'idrogeno e l'affidabilità dei componenti e delle strutture: un piccolo atomo, ma grandi conseguenze. Rivista Italiana della Saldatura, 2019
[31] Ustolin F, Paltrinieri N, Berto F. Loss of integrity of hydrogen technologies: A critical review. International Journal of Hydrogen Energy 45 (2020); 23809-23840.
[32] M. Nagumo, Fundamentals of Hydrogen Embrittlement, first ed., Springer, 2016.
[33] Pesenti Bucella D. Cathodic protection and hydrogen embrittlement. Università degli studi di Bergamo, 2019
[34] https://mtcsolutions.com/resources/tech-blogs/a-comprehensive-overview-of-environmental-hydrogen embrittlement/ [accessed Aug 2025]
[35] API SPECIFICATION 5L FORTY.SIXTH EDITION, APRIL 2018
[36] Sharma SK, Maheshwari S. A review on welding of high strength oil and gas pipeline steels. Journal of Natural Gas Science and Engineering 38 (2017) 203-217 https://doi.org/10.1016/j.jngse.2016.12.039
[37] Ohaeri EG, Qin W, Szpunar J. A critical perspective on pipeline processing and failure risks in hydrogen service conditions. Journal of Alloys and Compounds 857 (2021) 158240.
[38] Mizuno D, Yasuda K, Ishikawa N, Kimura M, Kobayashi K, Fujishiro T, Tada E, Hara T. Recent activities in ISIJ HLP research committee corrosion working group: proposal of pH buffer test solution for fitness-for-purpose HIC evaluations, ISIJ Int. 56 (2016) 498–503.
[39] Vervynckt S, Verbeken K, Lopez B, Jonas JJ. Modern HSLA steels and role of non-recrystallisation temperature, International Materials Reviews 57 (2012) 187–207
[40] Park GT, Koh SU, Jung GH, Kim YK. Effect of microstructure on the hydrogen trapping efficiency and hydrogen induced cracking of linepipe steel, Corrosion Science 50 (2008) 1865–1871
[41] Hwang B, Kim YM, Lee S, Kim NJ, Yoo JY, Correlation of rolling condition, microstructure, and low-temperature toughness of X70 pipeline steels, Metallurgiical and Materials Transactions A 36 (2005) 1793–1805.
[42] Sun Y, Cheng YF. Hydrogen-induced degradation of high-strength steel pipeline welds: A critical review. Engineering Failure Analysis 133 (2022) 105985.
[43] San Marchi C, Somerday BP. 2007. Effects of high-pressure gaseous hydrogen on structural metals. SAE Trans. 116, 94–110. http://www.jstor.org/stable/44723846.
[44] Lippold JC, 2014. Hydrogen-induced cracking. In: Welding Metallurgy and Weldability. John Wiley & Sons, inc., Hoboken, New jersey, pp. 213–262.
[45] Laureys A, Depraetere R, Cauwels M, Depover T, Hertelè S, Verbeken K. Use of existing steel pipeline infrastructure for gaseous hydrogen storage and transport: A review of factors affecting hydrogen induced degradation. Journal of Natural Gas Science and Engineering, 2022. 101 104534.
[46] Chen Y, Huang C, Liu P, Yen H, Niu R, Burr P, Moore KL, Martínez-Pañeda E, Atrens A, Cairney JM. Hydrogen trapping and embrittlement in metals – A review. International Journal of Hydrogen Energy 136, 2025 789-821
[47] T.A. Jack, F. Fazeli, J. Szpunar, Thermal desorption analysis of hydrogen uptake in pipeline steels after gaseous and electrochemical charging, J. Mater. Sci. 60 (2025) 2580–2606, https://doi.org/10.1007/s10853-024-10571-1.
[48] Q. Liu, A.D. Atrens, Z. Shi, K. Verbeken, A. Atrens, Determination of the hydrogen fugacity during electrolytic charging of steel, Corros. Sci. 87 (2014) 239–258, https://doi.org/10.1016/j.corsci.2014.06.033.
[49] Zhang R, Wang C, Liu C, Zhang H, Zhu M, Song Y, Zhang T, Li Y. Gaseous hydrogen permeation of pipeline steels: A focused review. Renewable and Sustainable Energy Reviews 211 (2025) 115304
[50] Sun Y, Cheng YF. Thermodynamics of spontaneous dissociation and dissociative adsorption of hydrogen molecules and hydrogen atom adsorption and absorption on steel under pipelining conditions. International Journal of Hydrogen Energy 2021; 46:34469–86. https://doi.org/10.1016/j.ijhydene.2021.07.217
[51] Crolet JL. Analysis of the various processes downstream cathodic hydrogen charging, I: Diffusion, laboratory permeation and measurement of hydrogen content and diffusion coefficient. Matériaux & Techniques, 104, p. 205, 2016
[52] Lasia A. Mechanism and kinetics of the hydrogen evolution reaction. International Journal of Hydrogen Energy. Volume 44, Issue 36, 26 July 2019, 19484-19518.

[53] De Marco A. Metodologie di studio dell'interazione Idrogeno-metalli: il caso degli acciai maraging. Univeersità di Pisa, 2015.
[54] Barrera O, Bombac D, Chen Y, Galindo-Nava Y, Gong P, Haley D, Horton R, Katzarov I, Kermode JR; Liverani C, Stopher M, Sweeney F. Understanding and mitigating hydrogen embrittlement of steels: a review of experimental, modelling and design progress from atomistic to continuum. Journal of Material Science, 2018. 53(9): p. 6251-6290.
[55] Nicodemi W. Metallurgia. Principi generali, 2007
[56] Turnbull, A., Hydrogen diffusion and trapping in metals, in Gaseous Hydrogen Embrittlement of Materials in Energy Technologies. 2012. p. 89-128
[57] Mohtadi-Bonab MA, Masoumi M, 'Different aspects of hydrogen diffusion behavior in pipeline steel', Journal of Materials Research and Technology, vol. 24. Elsevier Editora Ltda, pp. 4762–4783, May 01, 2023. doi: 10.1016/j.jmrt.2023.04.026.
[58] V. Olden, C. Thaulow, and R. Johnsen, 'Modelling of hydrogen diffusion and hydrogen induced cracking in supermartensitic and duplex stainless steels', Mater Des, vol. 29, no. 10, pp. 1934–1948, Dec. 2008, doi: 10.1016/j.matdes.2008.04.026.
[59] C.K. Gupta, Chemical Metallurgy: Principles and Practice, Wiley-VCH, 2003.
[60] Hoscke J, Roethig M, Tapia-Bastidas CV, Wahab Chowdhury MF, Venezuela J, Shu Y, Gray E, Atrens A. Determination of the hydrogen fugacity during cathodic hydrogen charging of X65 D pipeline steel. Corrosion Science, 2025, 243, 112580
[61] Yu H, Diaz A, Lu X, Sun B, Ding Y, Koyama M, He J, Zhou X, Oudriss A, Feaugas X, Zhang Z. Hydrogen embrittlement as a Conspicuous material challenge-Comprehensive Review and future directions. Chemical Reviews, 2024, 124/10
[62] Hinotani S, Ohmori Y, Terasaki F. Effects of Fe3C and Mo2C precipitation on hydrogen diffusivity and hydrogen embrittlement in iron alloys. Materials Science and Engineering 76, 1985, 57-69
[63] Silverstein R, Eliezer D, Tal-Gutelmacher E. Hydrogen trapping in alloys studied by thermal desorption Spectrometry. Journal of Alloys and Compounds 747, 2018, 511-522.
[64] Pressouyre GM. A Classification of Hydrogen Traps in Steel. Metallurgical Transactions,1979. 10: 1571-1573
[65] M. Martínez-Madrid, S. Chan, J. Charles, J. López and V. Castaño, "Effect of grain size and second phase particles on the hydrogen occlusivity of iron and steels," Material Research Innovations, vol. 3, no. 5, pp. 263-270, 2000.
[66] Razzini G, Maffi S, Mussati G, Peraldo Bicelli L. The scanning photoelectrochemical microscopy of diffusing hydrogen into metals. Corrosion Science, 37, 1131- 1141, 1995.
[67] Razzini G, Cabrini M, Maffi D, Mussati G, Peraldo Bicelli L. Photoelectrochemical visualization in real-time of hydrogen distribution in plastic regions of low-carbon steel. Corrosion Science 41, 203-208, 1999.
[68] Alraeesi A, Gardner T. Assessment of Sieverts Law Assumptions and 'n' Values in Palladium Membranes: Experimental and Theoretical Analyses. Membranes 2021, 11(10), 778; https://doi.org/10.3390/membranes11100778
[69] Hoschke J, Chowdury MFW, Venezuela J, Atrens A. A review of hydrogen embrittlement in gas transmission pipeline steels. Corrosion Reviews 2023; 41(3): 277–317
[70] Souza RC, Pereira LR, Starling LM, Pereira JN, Simões TA, Gomes JACP, Bueno AHS. Effect of Microstructure on Hydrogen Diffusion in Weld andAPI X52 Pipeline Steel Base Metals under Cathodic Protection. International Journal of Corrosion, 2017, 14. https://doi.org/10.1155/2017/4927210
[71] Mohtadi-Bonab MA, Szpunar JA, Razavi-Tousi SS. A comparative study of hydrogen induced cracking behavior in API 5L X60 and X70 pipeline steels. Engeneering Failure Analysis 2013; 33:163–75. https://doi.org/10.1016/j.engfailanal.2013.04.028.
[72] Koren E, Yamabe J, Lu X, Hagen CM, Wang D, Johnsen R. Hydrogen diffusivity in X65 pipeline steel: desorption and permeation studies. International Journal of Hydrogen Energy 2024; 61:1157–69. https://doi.org/10.1016/j.ijhydene.2024.03.027
[73] Dong CF, Li XG, Liu ZY, Zhang YR. Hydrogen-induced cracking and healing behaviour of X70 steel. Journal Alloy Compounds 2009;484(1–2):966–72. https://doi.org/10.1016/j.jallcom.2009.05.085.
[74] Cabrini M, Lorenzi S, Marcassoli P, Pastore T. Hydrogen embrittlement behavior of HSLA line pipe steel under cathodic protection. Corrosion Reviews,29, 2011, 261-274.
[75] Dong CF, Liu ZY, Li XG, Cheng YF. Effects of hydrogen-charging on the susceptibility of x100 pipeline steel to hydrogen induced cracking, International Journal Hydrogen Energy 34, 2009, 9879–9998.

[76] Huang F, Liu J, Deng Z, Cheng J, Lu Z, Li X. Effect of microstructure and inclusions on hydrogen induced cracking susceptibility and hydrogen trapping efficiency of X120 pipeline steel. Materials Science and Engineering A, 527, 2010 6997-7001-
[77] Mousavi Anijdan SH, Arab G, Sabzi M, Sadeghi M, Eivani AR, Jafarian HR. Sensitivity to hydrogen induced cracking, and corrosion performance of an API X65 pipeline steel in H2S containing environment: influence of heat treatment and its subsequent microstructural change. Journal of Materials Research and Technology
15, 2021, 1-16. https://doi.org/10.1016/j.jmrt.2021.07.118
[78] Parvathavarthini N, Saroja S, Dayal RK. Influence of microstructure on the hydrogen permeability of 9%Cr–1%Mo ferritic steel. Journal of Nuclear Materials, 264, 1999, 35-47. https://doi.org/10.1016/S0022-3115(98)00486-3
[79] Tau L, Chan SLI. Effects of ferrite/pearlite alignment on the hydrogen permeation in a AISI 4130 steel. Materials Letters, 29, 1996, 143-147.
[80] Luu WC, Wu JK. The influence of microstructure on hydrogen transport in carbon steels. Corrosion Science, 38, 1996, 239-245. https://doi.org/10.1016/0010-938X(96)00109-6
[81] Chan SLI, Lee HL, Tang JR. Effect of retained austenite on the hydrogen content and effective diffusivity of martensitic structure. Metall Trans A 1991; 22:2579
[82] Fallahmohammadi E, Bolzoni F, Fumagalli G, Re G, Benassi G, Lazzari L. Hydrogen diffusion into three metallurgical microstructures of a C–Mn X65 and low alloy F22 sour service steel pipelines. International Journal of Hydrogen Energy, 39, 2014, 13300-13313.
[83] Wang SH, Luu WC, Ho KF, Wu JK. Hydrogen permeation in a submerged arc weldment of TMCP steel. Materials Chemistry and Physics 77,2003,447-454
[84] Lan L, Kong X, Hu Z, Qiu C, Zhao D, Du L. Hydrogen permeation behavior in relation to microstructural evolution of low carbon bainitic steel weldments. Corrosion Science, 112, 2016, 180-193.
[85] Xue HB, Cheng YF. Hydrogen Permeation and Electrochemical Corrosion Behavior of the X80 Pipeline Steel Weld. Journal of Materials Engineering and Performance. 22, 2012, 170–175.
[86] Yazdipour N, Haq AJ, Muzaka K, Pereloma EV. 2D modelling of the effect of grain size on hydrogen diffusion in X70 steel. Computational Materials Science, 56, 2012, 49-57.
[87] Zhengli H, Bai A, Takashi I, Chaohua G, Jinyang Z. The finding of crystallographic orientation dependence of hydrogen diffusion in austenitic stainless steel by scanning Kelvin probe force microscopy. Scripta Materialia
131, 2017, 47-50
[88] Masoumi M, Silva CC, Béreš M, Ladino DH, Gomes de Abreu HF. Role of crystallographic texture on the improvement of hydrogen-induced crack resistance in API 5L X70 pipeline steel. International Journal of Hydrogen Energy, 42, 2017, 1318-1326.
[89] Masoumi M, Silva CC, Gomes de Abreu HF. Effect of crystallographic orientations on the hydrogen-induced cracking resistance improvement of API 5L X70 pipeline steel under various thermomechanical processing. Corrosion Science, 111, 2016, 121-131.
[90] D.G. Stalheim, B. Hoh, Guidelines for production of API pipelines steels suitable for hydrogen induced cracking (HIC) service applications, Proceedings of the 2010 8th International Pipeline Conference, 2010 8th international pipeline conference, Calgary, Alberta, Canada.
[91] Jiang Y, Li C, Wang D, Di X. Effect of cyclic plastic deformation on hydrogen diffusion behavior and embrittlement susceptibility of reeling-pipeline steel weldments. International Journal of Hydrogen Energy, 46, 2021, 30158-30172.
[92] Hussein AM, El-Awady JA. Quantifying dislocation microstructure evolution and cyclic hardening in fatigued face-centered cubic single crystals. Journal of the Mechanics and Physics of Solids, 91, 2016, 126-144.
[93] Li L, Song B, Cai Z, Liu Z, Cui X. Effect of vanadium content on hydrogen diffusion behaviors and hydrogen induced ductility loss of X80 pipeline steel. Materials Science and Engineering: A, 742, 2019, 712-721.
[94] Depover T, Verbeken K. Evaluation of the effect of V4C3 precipitates on the hydrogen induced mechanical degradation in Fe-C-V alloys. Materials Science and Engineering: A, 675, 2016, 299-313.
[95] Nagao A, Martin ML, Dadfarnia M, Sofronis P, Robertson IM. The effect of nanosized (Ti,Mo)C precipitates on hydrogen embrittlement of tempered lath martensitic steel. Acta Materialia 74, 2014, 244-254
[96] Li J, Wu J, Wang Z, Zhang S, Wu X, Huang Y, Li X. The effect of nanosized NbC precipitates on electrochemical corrosion behavior of highstrength low-alloy steel in 3.5%NaCl solution. International Journal of Hydrogen Energy, 42, 2017, 22175-22184.

[97] Xiao H, Huang F, Peng Z, Fan L, Liu J. Sequential kinetic analysis of the influences of non-metallic inclusions on hydrogen diffusion and trapping in high-strength pipeline steel with Al-Ti deoxidisation and Mg treatment. Corrosion Science, 195, February 2022, 110006.
[98] Huang F, Li XG, Liu J, Qu YM, Du CW. Effects of alloying elements, microstructure, and inclusions on hydrogen induced cracking of X120 pipeline steel in wet H2S sour environment. Materials and Corrosion. 63, 2012, 59-66.
[99] Kim SJ, Kim KY. Electrochemical hydrogen permeation measurement through high-strength steel under uniaxial tensile stress in plastic range. Scripta Materialia, 66, 2012, 1069-1072.
[100] Kim SJ, Jung HG, Kim KY. Effect of tensile stress in elastic and plastic range on hydrogen permeation of high-strength steel in sour environment. Electrochimica Acta 78, 2012, 139-146.
[101] Serna S, Martínez H, López S, González-Rodríguez J, Albarrán J. Electrochemical technique applied to evaluate the hydrogen permeability in microalloyed steels. International Journal of Hydrogen Energy, 30, 2005, 1333-1338. 2005
[102] Zheng S, Zhou C, Wang P, Chen C, Chen L. Effects of the temperature on the hydrogen permeation behaviours of L360NCS pipeline steel in 1MPa H2S environment. International Journal of Electrochemical Science, 8, 2013, 2880-2891.
[103] Oriani R. The diffusion and trapping of hydrogen in steel, Acta Metallurgica, 18, 1970, 147-157.
[104] Devanathan MAV, Stachursky Z, The adsorption and diffusion of electrolytic hydrogen in palladium. Proceedings of the Royal Societ, 1962, 270, 90-102.
[105] Thomas A, Szpunar JA. Hydrogen diffusion and trapping in X70 pipeline steel. International Journal of Hydrogen Energy, 45, 2020, 2390-2404.
[106] Gajek A, Zakroczymski T. Long-lasting hydrogen evolution on and hydrogen entry into iron in an aqueous solution. Journal of Electroanalytical Chemistry, 578, 2005, 171-182. https://doi.org/10.1016/j.jelechem.2004.12.038
[107] Addach H, Berçot P, Rezrazi M, Takadoum J. Study of the electrochemical permeation of hydrogen in iron. Corrosion Science, 5, 2009, 263-267. https://doi.org/10.1016/j.corsci.2008.10.024
[108] ISO 17081:2014. Method of measurement of hydrogen permeation and determination of hydrogen uptake and transport in metals by an electrochemical technique
[109] Ramunni V, De Paiva Coelho T, De Miranda P. Interaction of hydrogen with the microstructure of low-carbon steel," Materials Science and Engineering A, Vols. 435, 2006, 504-514.
[110] Duval S, Antaño-Lopez R, Scomparin C, Jerome M, Ropital F. Hydrogen permeation through Armco iron membranes in sour media. NACE International Corrosion, Paper 04740, 2004.
[111] Kittel J, Ropital F, Pellier J. New insight into hydrogen permeation in steel: measurements through thick membranes. NACE International Corrosion, Paper 08409, 2008.
[112] Modiano S, Carreño J, Fugivara C, Benedetti A, Mattos O. Effect of hydrogen charging on the stability of SAE 10B22 steel surface in alkaline solutions, Electrochimica Acta, 51, 2005 641-648.
[113] Zhang T, Zhao W, Zhao Y, Ouyang K, Deng Q, Wang Y, Jiang W. Effects of surface oxide films on hydrogen permeation and susceptibility to embrittlement of X80 steel under hydrogen atmosphere. International Journal of Hydrogen Energy. 43 (2018), 3353-3365. https://doi.org/10.1016/j.ijhydene.2017.12.170.
[114] Manolatos P, Jerome M, Galland J. Necessity of a palladium coating to ensure hydrogen oxidation during electrochemical permeation measurements on iron. Electrochimica Acta, 40, 1995 867-871.
[115] ASTM G148-97(2018) Standard Practice for Evaluation of Hydrogen Uptake, Permeation, and Transport in Metals by an Electrochemical Technique
[116] S. Rahimi, K. Verbeken, T. Depover, E. Proverbio, Hydrogen embrittlement of pipeline steels under gaseous and electrochemical charging: a comparative review on tensile properties, Engineering Failure Analysis 167 (2025) 108956, https://doi.org/10.1016/j.engfailanal
[117] G. Bai, Q. Wang, Y. Song, H. Deng, D. Li, Y. Li, Study on hydrogen resistance of X42 pipeline steel under electrochemical hydrogen charging condition, in: Proceedings of the. Volume 6: Materials and Fabrication. Virtual, ASME, 2020 V006T06A086, https://doi.org/10.1115/PVP2020-21229. Online. August 3.
[118] Lasia A. Mechanism and kinetics of the hydrogen evolution reaction, International Journal of Hydrogen Energy 44 (2019) 19484–19518, https://doi.org/10.1016/j.ijhydene.2019.05.183
[119] Venezuela J, Tapia-Bastidas C, Zhou Q, Depover T, Verbeken K, Gray E, Liu Q, Zhang M, Atrens A, Determination of the equivalent hydrogen fugacity during electrochemical charging of 3.5NiCrMoV steel, Corrosion Science 132 (2018) 90–106, https://doi.org/10.1016/j.corsci.2017.12.018

[120] Zheng S, Zhou C, Chen X, Zhang L, Zheng J, Zhao Y. Dependence of the abnormal protective property on the corrosion product film formed on H2S adjacent API-X52 pipeline steel, International Journal of Hydrogen Energy 39 (25), 2014,13919–13925, https://doi.org/10.1016/J.IJHYDENE.2014.04.077
[121] Zhou C, Zheng S, Chen C, Lu G. The effect of the partial pressure of H2S on the permeation of hydrogen in low carbon pipeline steel. Corrosion Science, 67, 2013, 184–192, https://doi.org/10.1016/J.CORSCI.2012.10.016
[122] Archer MD, Grant NC. Achievable boundary conditions in potentiostatic and galvanostatic hydrogen permeation through palladium and nickel foils. Proceedings of the royal society A. 39, 1984. https://doi.org/10.1098/rspa.1984.0096
[123] Zhang P, Laleh M, Hughes AE, Marceau RKW, Hilditch T, Tan MY. A systematic study on the influence of electrochemical charging conditions on the hydrogen embrittlement behaviour of a pipeline steel. International Journal of Hydrogen Energy 48, 2023, 16501-16516.
[124] Pourbaix M. Atlas of electrochemical equilibria in aqueous solution. NACE 1974;307
[125] Venezuela J, Blanch J, Zulkiply A, Liu Q, Zhou Q, Zhang M, Atrens A. Further study of the hydrogen embrittlement of martensitic advanced high-strength steel in simulated auto service conditions. Corrosion Science 2018; 135:120-35.
[126] Yan M, Weng Y. Study on hydrogen absorption of pipeline steel under cathodic charging. Corrosionion Science 2006;48(2):432-44.
[127] Dong C-f, Xiao K, Liu Z-y, Yang W-j, Li X-g. Hydrogen induced cracking of X80 pipeline steel. International Journal of Minerals, Metallurgy, and Materials 2010;17(5):579-86.
[128] Rahman KM, Mohtadi-Bonab M, Ouellet R, Szpunar J, Zhu N. Effect of electrochemical hydrogen charging on an API X70 pipeline steel with focus on characterization of inclusions. International Journal of Pressure Vessels and Piping 2019; 173:147-55.
[129] Yang X, Sun F, Li Q, Zhu R, Liu Z, Du C, Li X. Effect of hydrogen charging on the stress corrosion cracking behavior of X70 steel in simulated deep seawater environment. Metals 2022;12(2).
[130] Kittel J, Martin JW, Cassagne T, Bosch C. Hydrogen induced cracking (HIC) - laboratory testing assessment of low alloy steel linepipe, Corrosion (2008).
[131] Zhang L, Shen H, Lu K, Cao W, Sun Y, Fang Y, Xing Y, Du Y, Lu M, Investigation of hydrogen concentration and hydrogen damage on API X80 steel surface under cathodic overprotection, International Journal of Hydrogen Energy 42 (2017)
29888–29896, https://doi.org/10.1016/j.ijhydene.2017.10.116.
[132] Depover T, Escobar DP, Wallaert E, Zermout Z, Verbeken K, Effect of Hydrogen Charging on the Mechanical Properties of Advanced High Strength Steels, vol. 39, 2014, pp. 4647–4656, https://doi.org/10.1016/j.
ijhydene.2013.12.190
[133] Ren XC, Zhou QJ, Chu WY, Li JX, Su YJ, Qiao LG, The mechanism of nucleation of hydrogen blister in metals, Metallic Materials 52 (2007) 2000–2005, doi:10.1007/s11434-007-0269-y
[134] Rozenak P. Hemispherical bubbles growth on electrochemically charged aluminum with hydrogen, Int. J. Hydrogen Energy 32 (2007) 2816–2823, https://doi.org/10.1016/j.ijhydene.2007.01.009
[135] Kawashima A, Hashimoto K, Shimodaira S. Hydrogen Electrode Reaction and Hydrogen Embrittlement of Mild Steel in Hydrogen Sulfide Solutions. Corrosion NACE, Vol. 32, 1976, 321-331.
[136] Yazici B, Arslan G, Erbil M, Zor S. Effect of thiourea on the hydrogen yield in electrolysis, International Journal of Hydrogen Energy 23 (1998) 867–872, https://doi.org/10.1016/S0360-3199(97)00142-0.
[137] Fuji H, Fujishiro T, Hara T. Effect of ammonium thiocyanate on hydrogen entry behavior of low alloy steel under galvanostatic cathode charging. ISIJ Int 2021;61(4):1151-8
[138] Perez Escobar D, Minambres C, Duprez L, Verbeken K, Verhaege M. Internal and surface damage of multiphase steels and pure iron after electrochemical hydrogen charging. Corrosion Sci 2011;53(10):3166-76.
[139] Cauwels M, Depraetere R, De Waele W, Hertelè S, Depover Tom. Influence of electrochemical hydrogenation parameters on microstructures prone to hydrogen-induced cracking. Journal of Natural Gas Science and Engineering 101 (2022) 104533.
[140] Dwivedi SK, Vishwakarma M. Hydrogen embrittlement in different materials: A review. Inernational Journal of Hydrogen Energy 43 (2018), 21603-21616.
[141] Pfeil LB. The effect of occluded hydrogen on the tensile strength of iron. Proc R Soc Lond - Ser A Contain Pap a Math Phys Character 1926; 112:182-95.
[142] Gerberich WW, Oriani RA, Lji M-J, Chen X, Foecke T. The necessity of both plasticity and brittleness in the fracture thresholds of iron. Philos Mag A 1991; 63:363-76.

[143] Troiano AR. The Role of Hydrogen and Other Interstitials in the Mechanical Behavior of Metals. Metallography, Microstructure, and Analysis. 5, 2016, 557-569.
[144] Ramamurthy S, Atrens A. Stress corrosion cracking of highstrength steels. Corrosion Rev 2013 Mar 1;31(1):1-31.
[145] Sun B, Wang D, Lu X, Wan D, Ponge D, Zhang X. Current Challenges and Opportunities Toward Understanding Hydrogen Embrittlement Mechanisms in Advanced High-Strength Steels: A Review. Acta Metallurgica Sinica (English Letters) (2021) 34:741–754 https://doi.org/10.1007/s40195-021-01233-1
[146] Gerberich WW, Oriani RA, Lji MJ, Chen X, Foecke T. The necessity of both plasticity and brittleness in the fracture thresholds of iron. Philosophical Magazine A: Physics of Condensed Matter, Structure, Defects and Mechanical Properties. 63, 1991, 363-376.
[147] Sun B, Krieger W, Rohwerder M, Ponge D, Raabe D. Dependence of hydrogen embrittlement mechanisms on microstructure-driven hydrogen distribution in medium Mn steels. Acta Materialia 183, 2020, 313-328. https://doi.org/10.1016/j.actamat.2019.11.029
[148] Baechem CD. A new model for hydrogen-assisted cracking (hydrogen "embrittlement"). Metallurgical and Material Transactions 3, 1972, 441-455.
[149] Gangloff RP, Somerday BP. Gaseous hydrogen embrittlement of materials in energy technologies: mechanisms, modelling and future developments. Elsevier; 2012.
[150] Kappes M, Iannuzzi M, Carranza RM. Hydrogen Embrittlement of Magnesium and Magnesium Alloys: A Review. Journal of The Electrochemical Society 160, 2013.
[151] Song J, Curtin WA. Atomic mechanism and prediction of hydrogen embrittlement in iron. Nature Materials 12, (2013) 145-151.
[152] Shih DS, Robertson IM, Birnbaum HK. Hydrogen embrittlement of α titanium: In situ tem studies. Acta Metallurgica, 36, 1988, 111-124.
[153] Robertson I, Birnbaum HK, Sofronis P. Dislocations in Solids, 15, (Elsevier, 2009), 249
[154] Birnbaum HK, Sofronis P. Hydrogen-enhanced localized plasticity—a mechanism for hydrogen-related fracture. Materials Science and Engineering: A, 176, 1994, 191-202 https://doi.org/10.1016/0921-5093(94)90975-X
[155] Martin ML, Dadfarnia M, Nagao A, Wang S, Sofronis P. Enumeration of the hydrogen-enhanced localized plasticity mechanism for hydrogen embrittlement in structural materials. Acta Materialia
165, 2019, 734-750. https://doi.org/10.1016/j.actamat.2018.12.014
[156] Lynch SP. Environmentally assisted cracking: Overview of evidence for an adsorption-induced localised-slip process. Acta Metallurgica 36, 1988, 2639-2661. https://doi.org/10.1016/0001-6160(88)90113-7
[157] Lynch SP. Mechanistic and fractographic aspects of stress corrosion cracking. Corrosion Review 30, (2012), 63-104.
[158] Linch SP. Mechanisms of hydrogen assisted cracking - A review. Proc. of the International Conference on Hydrogen Effects on Material Behaviour and Corrosion Deformation Interactions. 2003.
[159] Lynch SP. Hydrogen embrittlement and liquid-metal embrittlement in nickel single crystals. Scripta Metallurgica 13, 1979, 1051-1056. https://doi.org/10.1016/0036-9748(79)90202-3
[160] Christmann K. Some general aspects of hydrogen chemisorption on metal surfaces. Progress in Surface Science 48, 1995, 15-26. https://doi.org/10.1016/0079-6816(95)93412-Z
[161] Nagumo M, Ohta K, Saitoh K. Deformation induced defects in iron revealed by thermal desorption spectroscopy of tritium. Scripta Materialia 40; 1999, 1359-6462.
[162] Nagumo M. Hydrogen related failure of steels – a new aspect. Materials Science and Technolog 20, 2004. https://doi.org/10.1179/026708304225019687
[163] Sakaki K, Kawase T, Hirato M, Mizuno M, Araki H, Shirai Y, Nagumo M. The effect of hydrogen on vacancy generation in iron by plastic deformation. Scripta Materialia 55, 2006, 1031-1034.
[164] Neeraj T, Srinivasan R, Li J. Hydrogen embrittlement of ferritic steels: Observations on deformation microstructure, nanoscale dimples and failure by nanovoiding. Acta Materialia 60, 2012, 5160-5171.
[165] Hickel T, Nazarov R, McEniry EJ, Leyson G, Grabowski B, Neugebauer J. Ab Initio Based Understanding of the Segregation and Diffusion Mechanisms of Hydrogen in Steels. JOM 66 2014 1399–1405.
[166] Liu J, Zhao M, Rong L. Overview of hydrogen-resistant alloys for high-pressure hydrogen environment: on the hydrogen energy structural materials. Clean Energy 7, 2023, 99–115, https://doi.org/10.1093/ce/zkad009
[167] Lynch SP. Progress towards understanding mechanism of hydrogen embrittlement and stress corrosion cracking. Nace International Corrosion Conference 2007.

[168] Shinko T. Experimental Characterization of Influence of Gaseous Hydrogen on Fatigue CrackPropagation and Crack Tip Plasticity in Commercially Pure Iron. PhD Thesis. Ecole Na-tionale Supérieure de Mécanique et d'Aérotechique - Poitiers, 2019.
[169] Omholt Myhre A. Effect of Hydrogen on Mechanical Performance of Vintage and Modern Pipeline Steels. Doctoral thesis at NTNU, 2025:357.
[170] Anderson TL. Fracture Mechanics - Fundamentals and Application (Third Edition). 2005: Taylor&Francis.
[171] https://www.marinecue.it/2019/08/04/frattura-fragile-liberty-ship-metallo/ [accessed november 2025]
[172] https://pstrust.org/map-of-major-incidents/sanbruno/ [accessed novembre 2025].
[173] Inglis CE. Stresses in a plate due to the presence of cracks and sharp corners. Transactions of the Institution Of Naval Architects, 55, 1913, 219-241.
[174] Griffith AA. The phenomena of rupture and flow in solids. Philosophical Transactions of the Royal Society A, 1921
[175] Westergaard HM. Bearing Pressures and Cracks. Journal of Applied Mechanics, 6, 1939, A49–A53.
[176] Irwin GR. Analysis of Stresses and Strains Near the End of a Crack Traversing a Plate. Journal of Applied Mechanics 24, 1957, 361–364.
[177] Milella PP. Meccanica della frattura lineare elastica ed elastoplatica. Ansaldo Nucleare, 1999.
[178] Rice JR. A Path Independent Integral and the Approximate Analysis of Strain Concentration by Notches and Cracks. Journal of Applied Mechanics 35, 1968, 379–386.
[179] ASME B31.12-2023; Hydrogen Piping and Pipelines. The American Society of Mechanical Engineers: New York, NY, USA, 2023
[180] ASME VIII Div. 3; Rules for Construction of Pressure Vessels, Article KD10 "Special Requirements for Vessels in Hydrogen Service". The American Society of Mechanical Engineers: New York, NY, USA, 2023
[181] ISO 11114-2023; Gas Cylinders—Compatibility of Cylinder and Valve Materials with Gas Content—Part 1 Metallic Materials. International Organization for Standardization: Geneva, Switzerland, 2023.
[182] ANSI/CSA CHMC 1; Test Methods for Evaluating Material Compatibility in Compressed Hydrogen Applications—Metals.
[183] EPRG Draft best practice guidelines for small scale fracture toughness testing in hydrogen gas of carbon steel pipeline material, 2024.
[184] ASTM E1681-03; Standard Test Method for Determining Threshold Stress Intensity Factor for Environment-Assisted Cracking of Metallic Material. American Society for Testing and Materials: West Conshohocken, PA, USA, 2020.
[185] ASTM F1459-06(2017) Standard Test Method for Determination of the Susceptibility of Metallic Materials to Hydrogen Gas Embrittlement (HGE)
[186] Paterlini L, Re G, Curia A, Ormellese M, Bolzoni F. Mechanical Testing Methods for Assessing Hydrogen Embrittlement in Pipeline Steels: A Review. Metals, 15 (2025), 1123. https://doi.org/10.3390/met15101123
[187] Bortolot, P, Beretta S, Bellingardi M. Fitness for Purpose Design of a Steel Cylinder for Hydrogen-Natural Gas Blends, Proceedings of the ASME 2011 Pressure Vessels & Piping Division Conference, 2011
[188] ASTM E399-22 Standard Test Method for Linear-Elastic Plane-Strain Fracture Toughness of Metallic Materials
[189] ASTM E1820-18 Standard Test Method for Measurement of Fracture Toughness.
[190] ISO 12135:2021 Metallic materials — Unified method of test for the determination of quasistatic fracture toughness
[191] ASTM G129-21 Standard Practice for Slow Strain Rate Testing to Evaluate the Susceptibility of Metallic Materials to Environmentally Assisted Cracking
[192] ASTM G142-98(2022) Standard Test Method for Determination of Susceptibility of Metals to Embrittlement in Hydrogen Containing Environments at High Pressure, High Temperature, or Both
[193] ISO 7039:2024 Metallic materials — Tensile testing — Method for evaluating the susceptibility of materials to the effects of high-pressure gas within hollow test pieces
[194] Moro I, Briottet L, Lemoine P, Andrieu E, Blanc C, Odemer G. Hydrogen embrittlement susceptibility of a high strength steel X80. Material Science Engeneering A 527 (2010), 7252–7260.
[195] Boot T, Riemslag TAC, Reinton ETE, Liu P, Walters CL, Popovich V. In-situ hollow sample setup design for mechanical characterisation of gaseous hydrogen embrittlement of pipeline steels and welds, Metals 11 (2021). https://doi.org/10.3390/met11081242
[196] Takasawa K, Ikeda R, Ishikawa N, Ishigaki R. Effects of grain size and dislocation density on the susceptibility to high-pressure hydrogen environment embrittlement of high-strength low-alloy steels. International Journal of Hydrogen Energy 37 (2012) 2669–2675. https://doi.org/10.1016/j.ijhydene.2011.10.099.

[197] Palombo M. Introduzione alle prove di meccanica della frattura per la caratterizzazione di giunti saldati in ambiente idrogeno. Rivista Italiana della Saldatura 1, 2024, 85-90.
[198] BS 8571:2018 – TC Method of test for determination of fracture toughness in metallic materials using single edge notched tension (SENT) specimens
[199] Chatzidouros EV, Papazoglou VJ, Pantelis DI. Hydrogen effect on a low carbon ferritic-bainitic pipeline steel. International Journal of Hydrogen Energy 2014; 39:18498–505.
[200] An T, Zhang S, Feng M, Luo B, Zheng S, Chen L, et al. Synergistic action of hydrogen gas and weld defects on fracture toughness of X80 pipeline steel. International Journal of Fatigue 2019; 120:23–32.
[201] Du Y, Lv L, Chen K, Dang G, Xu H, Zheng S. nvestigating variations in hydrogen-assisted crack propagation of X52 pipeline steel with different microstructural characteristics. Corrosion Science 239 (2024) 112417.
[202] Xing Y, Yang Z, Yao X, Wang X, Lu M, Zhang L, et al. Effects of hydrogen on the fracture toughness of X80 steel base metal and girth weld under strong cathodic current with in-situ hydrogen charging. Engineering Failure Analysis 2022;135:106143.
[203] Xu LY, Kang ZY, Han YD, Zhao L, Jing HY, Zhu WF. Effect of hydrogen on the fracture toughness of X65 high frequency welded pipeline. Welding in the WORLD 2019;63:75–86
[204] Martin ML, Connolly M, Buck ZN, Bradley PE, Lauria D, Slifka AJ. Evaluating a natural gas pipeline steel for blended hydrogen service. Journal of Natural Gas Science Engineering 2022; 101:104529.
[205] Hoyos JJ, Masoumi M, Pereira VF, Tschiptschin AP, Paes M, Avila JA. Influence of hydrogen on the microstructure and fracture toughness of friction stir welded plates of API 5L X80 pipeline steel. International Journal of Hydrogen Energy 2019; 44:23458–71.
[206] Giarola JM, Avila JA, Cintho OM, Pinto HC, de Oliveira MF, Bose Filho WW. The effect of hydrogen on the fracture toughness of friction-stir welded API 5L X70 pipeline steels. Fatigue & Fracture of Engineering Materials & Structures 2022; 45:3009–24
[207] Li X, Zhong Y, Li H, Liu Y, Shan G, Qu D, Zhang J, Djukic MB. Review of hydrogen embrittlement effect on fracture toughness of metallic materials: Influencing factors, and predictive models. Engineering Fracture Mechanics 327 (2025) 111392.
[208] Palombo M. Materiali Metallici-Testing in H2. Corso Aziendale-Saipem-Fano. 2025.
[209] Steiner M, Marewski U, Silcher H. DVGW Project SyWeSt H2—Investigation of Steel Materials for Gas Pipelines and Plants for Assessment of their Sustainability with Hydrogen; DeutscherVerein des Gas und Wasserfaches: Bonn, Germany, 2023.
[210] San Marchi C, Somerday BP. Technical Reference for Hydrogen Compatibility of Materials; Sandia National Laboratories (SNL): Albuquerque, NM, USA, 2012.
[211] Amaro RL, White RM, Looney CP, Drexler ES, Slifka AJ. Development of a Model for Hydrogen-Assisted Fatigue Crack Growth of Pipeline Steel. Journal of Pressure Vessel Technology, 140, 2018.
[212] Slifka AJ, Drexler ES, Amaro RL, Hayden LE, Stalheim DG, Lauria DS, Hrabe NW. Fatigue Measurement of Pipeline Steels for the Application of Transporting Gaseous Hydrogen. Journal of Pressure Vessels Technology 140, 2018, 011407.
[213] Yamabe J, Yoshikawa M, Matsunaga H, Matsuoka S. Effects of hydrogen pressure, test frequency and test temperature on fatigue crack growth properties of low-carbon steel in gaseous hydrogen. Procedia structural integrity, 2, 2016, 525–532.
[214] Xu K. Hydrogen embrittlement of carbon steels and their welds. Gaseous Hydrogen Embrittlement of Materials in Energy Technologies; Elsevier: Amsterdam, The Netherlands, 2012; 526–561.
[215] Ronevich JA, Song EJ, Feng Z, Wang Y, D'Elia C, Hill MR. Fatigue crack growth rates in high pressure hydrogen gas for multiple X100 pipeline welds accounting for crack location and residual stress', Engineering Fracture Mechanics, 228, 2020, 106846. doi: 10.1016/j.engfracmech.2019.106846
[216] Ogawa Y, Matsunaga H, Yamabe J, Yoshikawa M, Matsuoka S. Unified evaluation of hydrogen-induced crack growth in fatigue tests and fracture toughness tests of a carbon steel. International, Journal of Fatigue 103, 223–233 (2017).
[217] Nibur KA, Somerday BP. Fracture and fatigue test methods in hydrogen gas. In Gaseous Hydrogen Embrittlement of Materials in Energy Technologies; Elsevier: Amsterdam, The Netherlands, 2012; pp. 195–236.
[218] Walter, R. & Chandler, W. Cyclic-load crack growth in ASME SA-105 grade II steel in high-pressure hydrogen at ambient temperature (1976).

[219] Recanzone FA. Studio sperimentale della sensibilità all'infragilimento da idrogeno introdotto per via elettrolitica di giunti saldati in acciaio per tubazioni API 5L X52. Università degli Studi di Torino, 2022.
[220] Morando D. Studio dell'effetto di infragilimento indotto da H_2 caricato per via elettrochimica in acciai per gasdotti tramite set-up di prova progettato e costruito autonomamente. Università degli studi di Genova, 2022.
[221] Recanzone FA, Scaglione F, Catalano F, Spotorno R, Palombo M, De Marco M, Mortello M, Baricco M. Investigation of hydrogen embrittlement of an API 5 L X52 pipeline through potentiostatic charging. Corrosion Science 256, 2025, 113251.
[222] UNICEN/IR 17797, Infrastrutture del gas - Conseguenze dell'immissione di idrogeno nelle reti gas e identificazione delle relative esigenze di normazione nell'ambito del CEN/TC 234. 2022.
[223] Liu Q, Atrens A, Reversible hydrogen trapping in a 3.5NiCrMoV medium strength steel. Corrosion Science 96, 2015, 112–120, https://doi.org/10.1016/J.CORSCI.2015.04.011
[224] Hagen AB, Nyhus B, Gerhardt MR, Musinoi Hagen CH, Stenerud G, Alvaro A, Mainçon P, Olden V. Experimental determination of equivalent hydrogen gas pressure from electrochemical hydrogen charging. International Journal of Hydrogen Energy, 82, 2024, 1146-1156.
[225] ASTM E8/E8M-22 Standard Test Methods for Tension Testing of Metallic Materials
[226] UNI 3244:1980. Microscopic examination of ferrous materials. Rating of non-metallic inclusions in steels by reference pictures
[227] Cravero S, Ruggieri C. Estimation procedure of J-resistance curves for SE(T) fracture specimens using unloading compliance. Engineering Fracture Mechanics 74 (2007) 2735–2757
[228] Roberti R, Basha Sh. Un nuovo metodo semplificato per determinare la curva J-R da carico e spostamento registrati in una prova su un singolo campione. IGF 11-XI Convegno Nazionale Gruppo Italiano Frattura Brescia, 4-6 luglio 1995.
[229] Cravero S, Ruggieri C. Correlation of fracture behavior in high pressure pipelines with axial flaws using constraint designed test specimens—Part I: Plane-strain analyses. Engineering Fracture Mechanics, 2005 72(9).
[230] Silva LAL, Cravero S, Ruggieri C. Correlation of fracture behavior in high pressure pipelines with axial flaws using constraint designed test specimens. Part II: 3-D effects on constraint. Engineering Fracture Mechanics, 2006, 73(15).
[231] ISO 3690, Welding and Allied Processes Determination of Hydrogen Content in Arc Weld Metal, 2018.
[232] J. Capelle, I. Dmytrakh, Z. Azari, G. Pluvinage, Evaluation of electrochemical hydrogen absorption in welded pipe, Proc. Mater. Sci. 3 (2014) 550–555, https:// doi.org/10.1016/j.ijhydene.2013.08.118.
[233] ISO 15653:2018 Metallic materials — Method of test for the determination of quasistatic fracture toughness of welds
[234] Zhao Q, Xing Y, Huang X, Liu Q, Wang Z, Du Y, Zhang L. Study on the influence of microstructural defects of API 5L-B, X52, and X52QS pipeline steels on fracture toughness degradation under in-situ hydrogen environment. Journal of Materials Research and Technology 37 (2025) 4613–4630.
[235] ISO 643:2012 Steels — Micrographic determination of the apparent grain size
[236] ASTM E112 – 10 Standard Test Methods for Determining Average Grain Size
[237] ASTM E562-11 Standard Test Method for Determining Volume Fraction by Systematic Manual Point Count
[238] ASTM E1245-03 Standard Practice for Determining the Inclusion or Second-Phase Constituent Content of Metals by Automatic Image Analysis
[239] Chen Y, Li Y, Chen C. Studying the effect of electrode material and magnetic field on hydrogen production efficiency. Studying the effect of electrode material and magnetic field on hydrogen production efficiency, Magnetochemistry. 8 (2022) 53.
[240] Mohtadi-Bonab MA, Eskandari M, Rahman KMM, Ouellet R, Szpunar JA. An extensive study of hydrogen-induced cracking susceptibility in an API X60 sour service pipeline steel, Int. J. Hydrogen Energy 41 (2016) 4185–4197, https://doi.org/10.1016/j.ijhydene.2016.01.031
[241] Wang R. Effects of hydrogen on the fracture toughness of a X70 pipeline steel, Corrosion Science 51 (2009) 2803–2810.
[242] Elboujdaini M, Revie RW, Metallurgical factors in stress corrosion cracking (SCC) and hydrogen-induced cracking (HIC), Journal of Solid State Electrochemistry. 13 (2009) 1091–1099, https://doi.org/10.1007/s10008-009-0799-0
[243] Ohaeri E, Eduok U, Szpunar J, Hydrogen related degradation in pipeline steel: a review, International Journal of Hydrogen Energy 43 (2018) 14584–14617, https://doi.org/10.1016/j.ijhydene.2018.06.064
[244] Ogawa Y, Hino M, Nakamura M, Matsunaga H. Pearlite-driven surface-cracking and associated loss of tensile ductility in plain-carbon steels under exposure to high-pressure gaseous hydrogen, Int. J. Hydrog. Energy 46 (9) (Mar. 2021) 6945–6959, https://doi.org/10.1016/j.ijhydene.2020.11.137

[245] Park C, Kang N, Liu S. Effect of grain size on the resistance to hydrogen embrittlement of API 2W grade 60 steels using in situ slow-strain-rate testing, Corrosion Science 128 (2017) 33–41, https://doi.org/10.1016/j.corsci.2017.08.032.
[246] Zhou C, Ye B, Song Y, Cui T, Xu P. L. Zhang, Effects of internal hydrogen and surface-absorbed hydrogen on the hydrogen embrittlement of X80 pipeline steel, International Journal of Hydrogen Energy 44 (40) (2019) 22547–22558, https://doi.org/10.1016/J.IJHYDENE.2019.04.239
[247] Li X, Zhang J, Shen S, Wang Y, Song X. Effect of tempering temperature and inclusions on hydrogen-assisted fracture behaviors of a low alloy steel, Material Science Engineering A 682 (2017) 359–369, https://doi.org/10.1016/J.MSEA.2016.11.064
[248] Djukic MB, Bakic GM, Sijacki Zeravcic V, Sedmak A, Rajicic B. The synergistic action and interplay of hydrogen embrittlement mechanisms in steels and iron: localized plasticity and decohesion, Jul. 01, Elsevier Ltd, 2019, https://doi.org/10.1016/j.engfracmech.2019.10652810.1016/j.engfracmech.2019.106528.
[249] Weeks TS, Read DT. Comparison of J-integral from single specimen SE(T) tests on API-5L X100 line pipe steel. In ISOPE 2015 Conference (pp. 1-6). Kona, HI.
[250] Pussegoda LN, Tiku S, Park D, Tyson WR, Gianetto J. J-Resistance Results From Multi-Specimen and Single-Specimen Surface Notched SEN(T) Geometry. In Proceedings of the 2012 9th International Pipeline Conference (Vol. 3: Materials and Joining, pp. 539-544). Calgary, Alberta, Canada: ASME. doi:10.1115/IPC2012-90565
[251] Tyson WR, Gianetto JA, Low-Constraint Toughness Testing: Results of a Round Robin on a Draft SE(T) Test Procedure," Proceedings of the ASME Pressure Vessels & Piping Division Conference (PVP2013), Paris, France, Paper PVP2013-97299.
[252] Kyriakopoulou HP, Karmiris-Obrata´nski P, Tazedakis AS, Daniolos NM, Dourdounis EC, Manolakos DE, Pantelis D. Investigation of Hydrogen Embrittlement Susceptibility and Fracture Toughness Drop after in situ Hydrogen Cathodic Charging for an X65 Pipeline Steel. Micromachines 2020; 11: 430; doi:10.3390/mi11040430
[253] San Marchi C, Somerday B. SANDIA REPORT technical reference for hydrogen compatibility of materials technical reference for hydrogen compatibility of materials. 2023
[254] Du Y, Lv L, Chen K, Dang G, Xu H, Zheng S. Investigating variations in hydrogen-assisted crack propagation of X52 pipeline steel with different microstructural characteristics. Corrosion Science 2024; 239: 112417.
[255] Nguyen TT, Heo HM, Park J, Nahm SH, Beak UB. Fracture properties and fatigue life assessment of API X70 pipeline steel under the effect of an environment containing hydrogen. J Mech Sci Technol 2021;35(4):1445–55.
[256] Gutierrez-Solana G, Elices M. HIGH-PRESSURE hydrogen behavior of a pipeline steel. 1982.
[257] Catalano F, Palombo M, De Marco M, Mortello M, Recanzone FA, Baricco M, Milano I, Piccardo P, Spotorno R. Development of an experimental setup for testing X52 steel SENT specimens in electrolytic hydrogen to explore repurposing potential of pipelines. International Journal of Pressure Vessels and Piping, 216, 2025, 105527.
[258] Yao C, Ming H, Chen J, Wang J, Han E. Effect of Cold Deformation on the Hydrogen Permeation Behavior of X65 Pipeline Steel. Coatings 2023, 13, 280. https://doi.org/10.3390/coatings13020280
[259] Lee HL, Chan SLI, ydrogen embrittlement of AISI 4130 steel with an alternate ferrite/pearlite banded structure. Materials Science and Engineering A 1991; 142:193-201
[260] Tau L, Chan SLI. Effects of ferrite/pearlite alignment on the hydrogen permeation in a AISI 4130 steel. Materials Letters1996; 29:143-7.
[261] Sun Y, Cheng YF, Hydrogen permeation and distribution at a highstrength X80 steel weld under stressing conditions and the implication on pipeline failureand the implication on pipeline failure. International Journal of Hydrogen Energy 46 (2021), 23100-23112. https://doi.org/10.1016/j.ijhydene.2021.04.115
[262] Wang H, Ming H, Wang J, Ke W, Han E. Hydrogen permeation behavior at different positions in the normal direction of X42 and X52 pipeline steels. International Journal of Hydrogen Energy 72 (2024) 1105-1115. https://doi.org/10.1016/j.ijhydene.2024.05.479
[263] Haq AJ, Muzaka K, Dunne DP, Calka A, Pereloma EV. Effect of microstructure and composition on hydrogen permeation in X70 pipeline steels. International Journal of Hydrogen Energy 38 (2013) 2544-2556. http://dx.doi.org/10.1016/j.ijhydene.2012.11.127
[264] Zhao W, Du T, Li X, Sun H, Li B, Yuan S. Effects of multiple welding thermal cycles on hydrogen permeation parameters of X80 steel. Corrosion Science 192 (2021), 109797. https://doi.org/10.1016/j.corsci.2021.109797.
[265] https://e360.yale.edu/features/climate-lawsuits-oil-industry-research [accessed february 2026]
[266] Supran G, Rahmstorf S, Oreskes N. Assessing ExxonMobil's global warming projections. Science 379, 153 (2023). DOI: 10.1126/science.abk0063